OPTIMIZED DESIGN AND SYNTHESIS OF PHOTOCATALYTIC MODIFIED BLACK TITANIA FOR WATER TREATMENT

A Thesis

by

AHMED SHERIF BADRELDIN

Submitted to the Office of Graduate and Professional Studies of
Texas A&M University
in partial fulfillment of the requirements for the degree of

MASTER OF SCIENCE

Chair of Committee,	Ahmed Abdel-Wahab
Committee Members,	Mohamed Nounou
	Bilal Mansoor
Head of Department,	Nazmul Karim

August 2019

Major Subject: Chemical Engineering

ABSTRACT

Organic contaminants in water sources are perhaps amongst the most damaging presences in untreated waters due to their effects in fouling membranes and significantly increasing operational costs of water treatment facilities. Conventional treatment processes such as adsorption do not eliminate the contaminants from the environment, but simply transform them from the water phase to another phase. Heterogenous photocatalysis is a rather an attractive method for effectively mineralizing/degrading those organic contaminants via the illumination of solar light. Titania (TiO_2) is amongst the largest used and sought after photocatalysts due to its relatively high photoactivity. However, crippled by a fast electron-hole recombination rate and their activation is limited to the UV light which represents only about 5% of solar energy available, titania based photocatalysts have found a towering hinderance in entering commercial employment.

The design, development and performance evaluation of photoactive titania nanostructures that employ both UV and visible segments of the solar energy spectrum have been successfully carried out in this research work. The incorporation of multiwalled carbon nanotubes (MWCNTs) whilst maintaining a highly heterojunctioned and low aggregated structure was achieved via the investigation of factors that affect this nanocomposite. Furthermore, in order to increase the commercial appeal of the developed photocatalyst, a silica-coated paramagnetic iron oxide core was used to mount the photoactive black titania nanowires with incorporated MWCNTs

(bTNW/MWCNT@SiO_2@Fe_3O_4). In this way, a small magnetic field can easily collect all the solid photocatalysts in solution upon complete treatment of the water and recycle them to treat additional water volumes.

Photodegradation experiments were conducted in batch, using methylene orange (MO) as a mimicking agent organic contaminant. For each photodegradation experiment, 50 mL of 10 ppm MO contaminated synthetic waters were used, with a catalyst load of 1 g/L, an artificial solar intensity of 700 W/m^2, and a maintained pH value of 7 were used. Aliquots were collected with respect to time and the concentration of contaminant remaining was determined using a liquid UV-Vis-NIR technique. The final developed stand-alone black titania nanowires with incorporated MWCNTs (bTNW/MWCNTs) were found to yield a photodegradation efficiency of 97.4% in 20 minutes of solar irradiation, whilst the composite bTNW/MWCNT@SiO_2@Fe_3O_4 yielded a photodegradation efficiency of 90.68%.

The developed materials were thoroughly characterized via XRD, XPS, SEM, TEM, solid-state UV-Vis-NIR, elemental mapping, and FTIR. This allowed for the progressive monitoring of the different changes in design parameters that were undergoing from each successive synthesis step in order to better depict a clearer understanding of the importance and physical contributions these design parameters have on apparent photodegradation efficiency.

DEDICATION

To my father, and role model, Sherif El-Sayed Badreldin, who taught me the essence of love, family, hard work, discipline and morality. To my mother whose unwavering love and support continues to build me up. To my brother, Marwan Sherif Badreldin, who supported me through the most difficult times in my life and perseveres to be an example of commitment and joy to everyone around him. To my family in Alexandria, Egypt whose prayers and support constantly serve to remind me of my purpose. And to my partner, Honey-Grace Santos, for her brief but momentous impact on my life and dreams.

ACKNOWLEDGEMENTS

I would like to express my deep appreciation to Dr. Ahmed Abdel-Wahab, my advisor, for his time, insight, guidance and patience throughout my graduate studies journey. His support and teachings have made the next step of my journey – continuation into the PhD program for Chemical Engineering at TAMU – possible.

I would also like to express my gratitude to Dr. Kumar Vignesh and Dr. Dong Suk Han for their guidance around the lab and their thoughtful insights when it came to experimental setups. I would also like to thank Dr. Yiming Wubulikasimu for his assistant in material characterizations. I deeply appreciate the support I have received from different groups at Qatar Environment and Energy Research Institute (QEERI) and Qatar University Center for Advanced Materials (QU – CAM) with respect to material characterization.

CONTRIBUTORS AND FUNDING SOURCES

This work was made possible by the financial support provided by Texas A&M University at Qatar. I would also like to thank the insightful contributions by Dr. Mohamed Nounou and Dr. Bilal Mansoor who acted as committee members for this work.

TABLE OF CONTENTS

LIST OF FIGURES

Page

LIST OF TABLES

Page

CHAPTER I

INTRODUCTION

Climate and social changes including, but not limited to, population and economic growth, an increase in social disparities, globalization, urbanization and a myriad of social discontent have continuously been putting more pressure on water, energy and food resources. This subsequently increases the risk of conflict between these resources which have rather complex interactions. Statistically, global population has seen an exponential increase over the past few decades and is expected to grow to 8 billion by 2025, 10 billion by 2050, and all billion by 2100 (DESA, 2017). With respect to globalization, the amalgamation of traded percentage of food produced has globally grown from 10% in 1970 to 15% in 2000. Stochastically, the demand for water, energy and food are estimated to increase by 40%, 50% and 35%, respectively, by 2030. Addressing the aforementioned predicaments have therefore become one of the most pressing global environmental challenges of our time.

The familiar interconnectedness of food and water is perhaps most conspicuous in the agricultural predisposition of consuming a major bulk of the available water supply. Generally, about 70-80% of global water supply is allocated to agricultural demand. Touching on an earlier point, with the inevitability of continued population increase, a cascading increase in demand for potable water and food – most of which is agriculturally based – it is expected to follow. It has become clear that innovative

approaches are needed to bridge the disparity between multiple, and perhaps antagonistic, human needs and demands to achieve sustainable development goals (SDGs) set by the United Nations (UN) for 2030 (UN, 2016). **Figure 1** below depicts the intertwinement of food, water, and energy. It has been argued that a nexus approach is most appropriate in tackling the aforementioned dilemma, however this work will primarily scope water as the challenge of interest. The word 'nexus' comes from the Latin *nectare*, to connect. However, it is this work's belief that through the initial probing, understanding and effective demonstration of efficient solutions for each challenge singly, one may postulate an amalgamation of effective solutions that address the food-water-energy nexus.

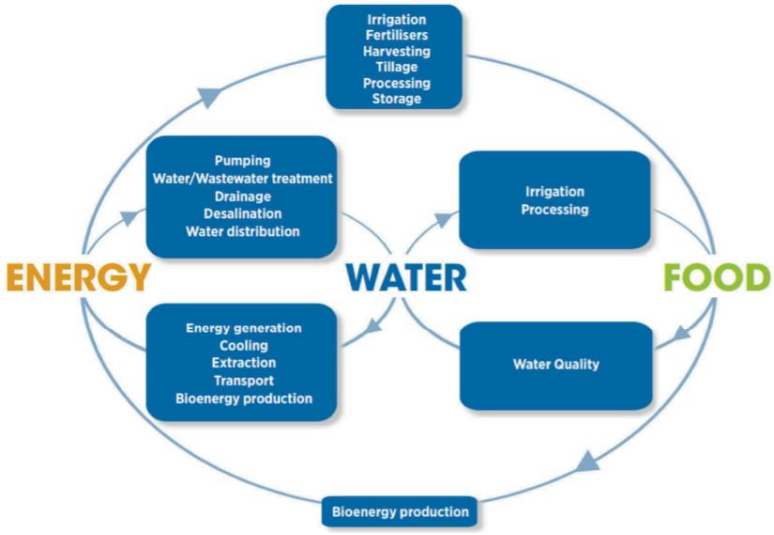

Figure 1 – Interconnectedness of Food-Water-Energy on Governmental Uses (UN, 2016)

Amongst the myriad of both conventional and emerging water treatment technologies, special interest has been dedicated to heterogenous photocatalytic treatment processes, especially over the past two decades. Briefly, heterogenous

photocatalysis involves a two-phase interaction between a solid photocatalyst and the liquid/aqueous medium. This will be elaborated on in later sections.

The increased appeal towards photocatalysis as a treatment methodology of persistent organic contaminants in waters was a result of several factors. Due to the increased commercial utilization of tertiary treatment membrane-based technologies (i.e. Reverse Osmosis (RO), Nanofiltration (NF)) for desalination and other treatment operations, membrane fouling due to organic and biological contaminants persisting from pretreatment systems causes a significant energy and fiscal hindrance to the potential full utilized efficiency of membrane-based systems. As such, a natural and focus-driven progression to effective pretreatment processes that effectively remove or degrade natural organic matters (NOMs) led to increased attention to photocatalytic processes. Moreover, owing to the constant improvement and development of nanosized photocatalytic materials, a prevalent increase in degradation efficiencies have been observed. Photocatalytic processes have an added advantage, which is forsaken in other pretreatment processes. Ordinarily, in conventional pretreatment processes (i.e. coagulation-based technologies), the organic contaminant is simply transported from one phase – namely the liquid water – to the solid phase of the coagulant material utilized. This methodology of removing organics from downstream processes, is derogatory in the sense that the coagulant material will have a low finite lifetime before costly regeneration processes are used. Adopting an effective photocatalytic material, however, would indicate that the complex organic contaminant is effectively degraded to its base

carbon form (i.e. CO_2); in turn eliminating any costly regeneration costs and ensuring that the contaminant is degraded in-situ.

Moreover, photocatalysis has several direct advantages including mild operation conditions, low energy consumption, and economic operation costs (S. Y. Lee, & Park, S. J. , 2013). Heterogenous photocatalysis employs semiconductor materials such as TiO_2, ZnO, Bi_2S_3, Bi_2WO_6, ZnS, Fe_2O_3, Ag_2CO_3, etc. as photocatalytic reagents (Dai, Yu, & Liu, 2012; Devi, 2013; Lu, 2012; J. Yu, & Yu, X., 2008; J. Yu, Xiong, J., Cheng, B., Yu, Y., & Wang, J., 2005; Jiaguo Yu, Zhang, & Liu, 2010; Q. Zhang et al., 2015). Upon photo-illumination, whereby a photon with greater energy than the semiconductor band gap, will result in a photoexcitation. During which, an electron will 'jump' from its valence band to a higher energy conduction band, migrating to the surface of the photocatalyst to initiate a photocatalytic decomposition of organics and deactivation of pathogens (Fox & Dulay, 1993).

In the past few decades, TiO_2 has received swelling attention in photocatalysis fields due to its ability to remove fouling organics. Furthermore, TiO_2 as a photocatalyst material has been widely promoted for its high chemical stability, nontoxicity, relative high availability, and cost-benefit properties (Cargnello, Gordon, & Murray, 2014; X. Chen & Mao, 2007; Fujihira, Satoh, & Osa, 1981; Y. Zhang, Tang, Z. R., Fu, X., & Xu, Y. J. , 2010). However, no material comes with a fully attainable set of advantageous properties for a given purpose. For instance, with respect to TiO_2-based photocatalytic systems, they suffer from a low adsorption capacity, small surface area, a relatively rapid electron-hole recombination rate, and a low utilization of solar energy. The last of these

drawbacks, focuses on the fact that TiO_2-based materials are photoexcited only by a small band of the spectrum reaching us from the Sun. Basic TiO_2-based materials can only utilize around 5% of the solar spectrum (namely UV) that reaches the surface. This inadequacy in a large spectrum coverage in terms of active utilization is owed to TiO_2's wide band-gaps – 3.2 eV for anatase and 3.0 eV for rutile (Hossain, 2010).

Clear defalcations in utilized methods used for water treatment coupled with a continuously growing water thirsty global population has subsequently placed an extensive amount of stress on pre-existing natural water resources. Due to a prevalent augmentation of policies to conserve freshwater sources, countries have turned to other water sources for treatment and purification for use amongst several major sectorial uses, namely irrigation, municipal, livestock, steam-electric, manufacturing, mining, and produced water from the oil-and-gas industry. Different water user sectors realize their water supply from different sources – predominantly groundwater, surface or treated wastewater sources.

With respect to organic contaminant degradation utilizing photoactive nanomaterials, several mimicking agents are typically used to test the photoactivity and quantum efficiency of a photocatalyst. It has been reported that textile dyes represent a predominant fraction of organic contaminants in industrial wastewater sources (Konstantinou, 2004). This is commodiously due to a high percentage of textile dyes – up to 20% - being lost during the dying process. This percentage varies between the different dying techniques employed worldwide (Zollinger, 1991). Over 10,000 azo dyes are in commercial use for a myriad of processes and applications. Textile dyes include

methylene orange (MO) and methylene blue (MB) which are reported to account for severe health concerns and eutrophication in ecological systems – which can consequently have devastating effects on the food web downstream (Schneider, 2014). Due to the general complex structural nature of most of these azo dyes, they can serve as reasonable mimicking agents for complex and persistent NOMs and synthetic organic contaminants that find their way to different water sources (i.e. groundwater, surface water, municipal and industrial wastewater, etc.). **Figure 2** shows a depiction of the methylene orange, the mimicking agent of choice that will be employed to probe the photocatalytic efficiency of the synthesized titania-based nanocomposite in this research at degrading organic contaminants in water systems. The polar ionic nature of those dyes differs (i.e. cationic and anionic) and as such, different parametric variables can significantly affect the degree of adsorption – an essential step in heterogenous photocatalysis – and subsequently the observed photodegradation efficiency of the photocatalytic system. Parametric factors such as temperature, catalyst loading, initial contaminant concentration, irradiated light intensity, pH, dissolved oxygen (DO), etc. all may have varying effects depending on the contaminant and photocatalyst employed. However, some general trends between those parameters have been identified and will be discussed in later sections of this thesis.

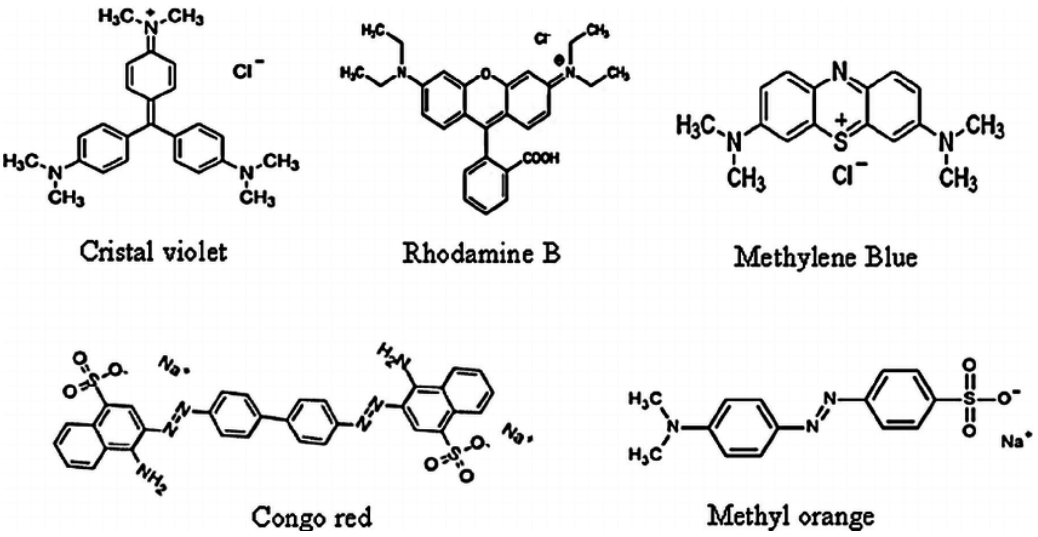

Figure 2 – Representative Chemical Structures of Typical Organic Dyes

Understanding the different factors that affect a photocatalyst's efficiency is not a simple task. Depending on the semiconductor material utilized, the photocatalyst's morphology, crystallinity, preparation technique and semiconductor precursor used are all typical factors that can have substantial effects on the final photoactive nanomaterial. As will be further elaborated on in later sections, prior to formalizing an effective nanocomposite photocatalyst for this work, a careful hypothesis based on reported characterizations and performances of TiO_2-based photocatalytic materials were investigated.

A major drawback of heterogenous photocatalysis has always been the predicament of recycling and recollecting the photocatalyst in a large-scale photoreactor. Consequently, it is of paramount importance to effectively incorporate and employ a retainment mechanism for the photocatalyst of interest, whilst maintaining a high recyclability and photoactivity in degrading the target organic contaminants.

Subsequently, and whilst keeping all the previously noted challenges in mind, a highly photoactive titania-based nanocomposite with a modified nanowire morphology will be synthesized, optimized and utilized in this work. Furthermore, this material will undergo surface defect alterations in order to induce oxygen vacancies in the structure – found to reduce the semi-conductor's band-gap energy and therefore enhance visible light absorption. The nanomaterial will be incorporated with multi-walled carbon nanotubes (MWCNTs), induce a beneficial reduction in the so called 'electron-hole recombination rate'. Lastly, in an effort to obtain a highly retainable photocatalyst that can be effectively utilized for large-scale organic contaminant degradation processes, the aforementioned nanocomposite photocatalyst will be chemically bound to the surface of a paramagnetic silica-coated iron oxide microsphere core.

In order to achieve the highest photoactivity possible from the proposed nanocomposite photocatalyst, every step of the synthesis was optimized and characterized prior to proceeding to the following sequential step, in order to investigate the effects each may have on the material's morphology, crystallinity, band-gap energy, and ultimately its photoactivity. Moreover, the nanocomposite's degradation efficiency was tested by varying different parametric variables including the initial concentrations of MO, catalyst loading, pH, irradiated light intensity, etc. This has led to a greater understanding and effective photoactivity optimization of the ultimate photocatalyst synthesized and the mechanisms at work during the visible light based photodegradation process employed.

Scope of Work

The underlying target of this project is to develop an integrated solar-driven photochemical and membrane separation treatment process with a novel photocatalyst design and specific components tailored to impaired water pretreatment and reuse. The photocatalyst material of interest will be based on a reduced (black) TiO_2 nanowire photoactive catalyst, with a MWCNT mesh for enhanced photocatalytic efficiency and a paramagnetic core for ease of retainment during flow operations. The aforementioned novel catalyst will be developed and utilized for the removal of organic contaminants prior to membrane desalination processes.

Four specific objectives will be pursued throughout the course of this project:

- Design, fabricate and optimize black TiO_2 nanowires with MWCNTs incorporated in the main catalyst mesh ($bTiO_2$ NW/MWCNT)
- Incorporate the optimized core titania-based photocatalyst with different carbon-based amalgamations – namely Activated Carbon (AC) – and under different surface activation fabrication processes
- Evaluate the performance of photocatalyst nanocomposites for solar-driven photocatalytic organic degradation using synthetic impaired waters

Investigate and optimize a method for applying $bTiO_2$ NW/MWCNT nanocomposite in continuous flow treatment systems.

CHAPTER II

LITERATURE REVIEW

Background

Water – a presently cheap commodity that has been having an ever-increasing demand to endow a multitude of industrial, municipal, agricultural and energy-based processes. Due to the serendipitous properties of water as an excellent solvent, a high energy-capacity fluid, and one of humanity's fundamental needs, a particular attention has been devoted to conserving existing water resources and replenishing wastewater through treatment processes. As is the case with most developing technologies, the array of commercially available water treatment processes – whether primary, secondary or tertiary treatment methodologies – are respectively designed to target and treat a relatively small group of components present in the water source to be treated.

Prior to properly and effectively identifying which water treatment processes will be utilized in junction for efficient treatment, the nature of the contaminated water source needs to first be identified. Discrepancies in source-water utilizations by sectorial use may change significantly between countries depending on attainable resources. Generally, as was mentioned previously, irrigation uses up most of a country's available water resource. **Figure 3** below shows the allocation of surface and groundwater use by each aforementioned sectorial use (EPA, 2018).

Surface water generally captains water obtained from streams, rivers, lakes, and underground reservoirs. In the United States, approximately 80% of the total national water use comes from surface water sources (EPA, 2018). Upon utilization of surface water for any of the above sectorial uses, the water is ordinarily returned to the source following proper treatment that abides by discharge standards set by NPDES (National Pollutant Discharge Elimination System) conferred by the US EPA (Environmental Protection Agency) (EPA, 2018).

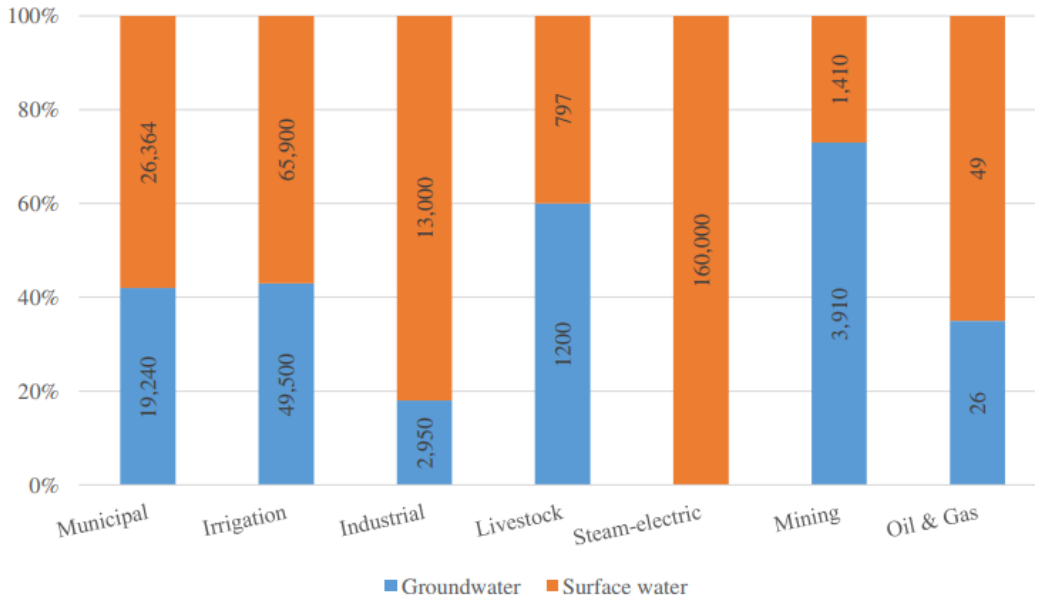

Figure 3 – Total Water Use Across Different Sectors (EPA, 2018)

Groundwater is namely obtained from underground aquifers which in turn result from any water source (i.e. precipitated) that seems into the soil and gets stored above nonporous rock formations underground. In the United States, about 20% of the total national water use comes from groundwater sources (EPA, 2018). However, in some

countries with very porous surface soil layers and relatively high precipitation (i.e. North African countries), groundwater use accounts for a much higher percentage of their respective total national water use. As can be seen from **Figure 3** groundwater sources account for about 60% of the national agricultural water supply.

The existence of a myriad of wastewater supplies from different industries calls for the initial prescreening or water content characterization to ensure the proper water treatment technology is exploited for the treatment process. pH, total suspended solids (TSS), total dissolved solids (TDS), alkalinity, natural organic matters (NOM), biochemical oxygen demand (BOD), oil and grease content, temperature, toxic ions, etc. are the most common characterization parameters used in determining which treatment process is optimum for the incoming untreated water supply. Of interest to this research work, the pharmaceutical, textile, and pulp and paper industries release wastewaters with relatively high levels of TSS and BOD causing undesirable consequences on the receiving environment if improper treatment is carried out. For instance, the release of wastewater high in dissolved organic compounds can cause eutrophication – in turn extensively harming marine life (Richard Helmer, 1997).

Organics present in untreated water supplies can include, but are not limited to, wastes from the pharmaceutical, textile, pulp and paper industries, and NOMs present in the case of surface and groundwater. An adequate technique is needed to properly remove such organics from their water source. As can be seen in the following subsection, conventional methods ineffectively focus on simply transferring the organics

from the liquid phase to another phase – which is not deemed a permanent and sustainable solution.

Water's advantageous properties that led to endless chemical processes utilizing it as a solvent, has also been water's bane when it comes to removing soluble organic contaminants from it. One of the most prominent organic contaminants found in industrial wastewater sources has been dyes, and in particular azo dyes – namely identified by comprising of an azo bond (-N≡N-) in their chemical structure. Upon the serendipitous discovery of 'Mauevin' in 1856, current production and utilization of over 10,000 different dyes finds its way in wastewater effluents from textile, pulp and paper, pharmaceutical and a myriad of other industries. It is estimated that about 15-20% of the initial dye concentration persists in wastewaters and as such make the wastewaters very difficult to use in agricultural, municipal or other industrial purposes without proper treatment. Due to the organic fouling properties of azo dyes, they severely decrease the flux efficiency and degrade membranes used downstream as tertiary water treatment processes. As will be illuminated on briefly, organic azo dyes are extremely problematic in removing using existing pretreatment processes, namely adsorption methods (i.e. activated carbon adsorption). Moreover, such pretreatment processes are non-destructive – whereby the contaminant is simply transferred between two different phases and not mineralized. Advanced Oxidation Processes (AOP) utilizes the very cogent oxidizing hydroxyl radical to completely mineralize the contaminant, rendering AOPs as a growing field of interest for the ever-increasingly present azo dyes in industrial wastewaters.

It is worth elaborating that organic treatment can be undertaken at different stages of a water treatment processes depending on the incoming water supply and intended final allocation of the treated produced water. For instance, it is generally used as a pretreatment step prior to tertiary processes (i.e. nanofiltration (NF), Reverse Osmosis (RO)) in the case of treating industrial wastewater, brackish or seawater for municipal use. It can also be used as a 'polishing' or tertiary process in the case of treating municipal wastewater upon the actual screening, filtering, and elimination of microorganisms steps – in the case of potability being the intended end-goal of treatment. Regardless of the processes train, incoming source, and intended use, the effective and sustainable removal of organic contaminants from water continues to be a persisting predicament. The aim of this research is to develop a full spectrum organic removal from water methodology that is both environmentally benign, highly cyclable, efficiency and sustainable. Azo dyes (i.e. MO) will be used as organic mimicking agents in artificially contaminated waters.

Conventional Water Treatment Processes

There are two predominant desalination water treatment routes that are commercially utilized for removal of dissolved solids from water, namely thermal processes and membrane-based processes. Common thermal processes include, but are not limited to, Multistage Flash (MSF), Mechanical Vapor Compression (MVC), and Multi-Effect Distillation (MED). Briefly, thermal processes work on the fundamental principle that a non-volatile dissolved salt will remain in solution as the water is evaporated. On the

contrary, the most common membrane-based process includes Seawater Reverse Osmosis (SWRO), Brackish Water Reverse Osmosis (BWRO), Nano-Filtration (NF), and Electrodialysis (ED). Reverse Osmosis process count on dynamic pressure to essentially reject salts, where electrodialysis depends on inducing ion-selective permeation via the utilization of electric power – leaving a diluted water solution. Micro-Filtration is predominantly used to separate out suspended particles and viruses, Ultra-Filtration separates out bacteria and virus, and finally Nano-Filtration is utilized in separation of heavy salts (Semiat, 2000).

Upon on the initial effective characterization of the incoming water source to be treated, bar screening and simple granular bed filtration is used to eliminate large particles that may block downstream process. Chemical additives (i.e. anti-scaling, anti-foaming agents) are utilized to control preliminary physical and chemical effects the incoming contaminated water may have on equipment (i.e. heat exchangers and membranes) downstream. Pretreatment is of paramount importance for thermal processes in order to mitigate against corrosion and scaling predicaments that arise on process equipment. Membrane-based treatment methods not only face the same challenges as thermal processes, with the added complexity of complications resulting from membrane fouling due to organic or biological fouling.

In the case of treating waters containing high TDS (i.e. dissolved salts) and TSS (i.e. organics), a primary treatment step namely includes coagulation clarifiers which amalgamate and flocculate organic matter for ease of separation. The process can then pass through biological reactors and thermal, or membrane-based, tertiary separation

processes. However, in the case of treating municipal wastewaters, where TDS is low, organic removal is usually performed as a final step, again using coagulation clarifiers.

There has been an array of research-based advances that account for coagulation technologies. A more efficient coagulant material will relieve stress downstream on tertiary treatment processes, which account for the bulk of a treatment plant's operational and capital costs. The below section briefly investigates some of the advances achieved in coagulant materials.

Coagulant-Based Technologies

Coagulation based technologies used in clarifier/residence tanks are specifically aimed at captaining suspended organic molecules in untreated waters. It is worth noting that the character, content and interference properties of the contaminating organics depends greatly on the biogeochemical cycles of the emitting environment(Fabris, Chow, Drikas, & Eikebrokk, 2008). For instance, the interference properties of NOMs is due to their tendency to impede the elimination of other contaminants. Moreover, water-borne organics in their various forms, severely contribute to formations of disinfection by-products (DBPs) – i.e. haloacetic acids (HAAs) and trihalomethanes (THMs) – which adds an extra level of complexity for effective treatment and removal of all organic contaminants. Organic contaminants contain both hydrophilic and hydrophobic fractions, whereby the hydrophobic fraction is usually predominant. Carbohydrates, proteins and carboxylic acids containing nitrogen and aliphatic carbons comprise of the majority of the hydrophilic fraction in NOMs, whereas humic substances (i.e. humic and

fulvic acids) comprising of phenolic structures with aromatic carbons and conjugated double bonds makeup the hydrophobic fraction of NOMs (Swietlik, Dabrowska, Raczyk-Stanislawiak, & Nawrocki, 2004). Similarly with azo dyes, both cationic and anionic dyes contaminate industrial wastewaters. As a pretreatment sequence, coagulation coupled with flocculation followed by sedimentation and filtration are considered the most economically and practically feasible process for removal of organics (Jacangelo JG, 1995).

During coagulation, the electric double layer's potential (repulsive due to same charged species) of organic colloids decreases enough to the point where micro-amalgamations can form and coalesce. Flocculation occurs when these micro-amalgamations collide and form larger bulkier counterparts (i.e. flocs). Generally, coagulation processes have been utilized for decreasing the turbidity, color, odor, and pathogenic content of water. This requires a very fine-tuned dependability on parametric conditions, namely pH (Bond, Goslan, Parsons, & Jefferson, 2010), which are not always in agreement with optimum conditions needed for organic removal (Jianfeng Yu et al., 2007). Effective removal of organic contaminants depends on an array of parameters including coagulant identity, mixing, concentration, pH, temperature, molecular properties of the predominant organics of interest. During aggregation/coagulation, the prevalent mechanism of coagulation consists of a sequence of steps including charge neutralization, adsorption, entrapment and complexation with coagulant's metallic cations (i.e. Al^{3+} and Fe^{3+} upon hydrolysis of the metallic salts) that result in a precipitative aggregate (Jarvis, Jefferson, & Parsons, 2004).

Alum ($Al_2(SO_4)_3$) along with aluminum chloride ($AlCl_3$) as a co-coagulant have been extensively employed as effective aluminum-based coagulants, however depending on external factors (i.e. low temperatures and pH) can leave residual aluminum compounds in the released water product. These residuals have been found to have severe health effects and disadvantageous effects downstream (i.e. spontaneous flocculation). Such predicaments can be controlled by running the system at higher temperatures and pH values, however this consequently affects the effectiveness of organic and turbidity removal – presenting an undesirable bottleneck situation (Chow, van Leeuwen, Fabris, & Drikas, 2009; Matsukawa, 2006). Other coagulants that have been extensively developed and used include ferric-based coagulants (i.e. ferric chloride ($FeCl_3$) and ferric sulfate ($Fe_2(SO_4)_3$)), however other predicaments and unwanted compromises are present when using ferric-based coagulants as well (Siéliéchi et al., 2008; V. Uyak, Yavuz, S., Toroz, I., Ozaydin, S., & Genceli, E. A., 2007). Cationic polyelectrolytes (a polymer with cationic groups) have been broadly employed for removal of organic contaminants, since in aqueous contaminated solutions tend to be anionic which allows for removal via charge neutralization (H.T. Gao, 2011). It was found that cationic polyelectrolytes are rather toxic to marine organisms and as such they have been disallowed for use in several countries.

Electrocoagulation (EC) as a pretreatment coagulation process has also been studied extensively, however it is yet to be determined as a feasible substitute for conventional coagulation methods (Bagga, Chellam, & Clifford, 2008). Water soluble anodes fabricated from aluminum or ferric-based coagulants are used in EC, whereby the release

of respective metal cations in the electrolyte complex with anionic organics and are carried to the anode through electrophoretic motion (Mollah, 2004). Coagulation along with other treatment processes used symbiotically have also been studied. Predominantly, Magnetic Ion Exchange Resins (MIERs), oxidation (i.e. Advanced Oxidation Processes, Chlorination, etc.) and Activated Carbon Filtration (ACF) have all been tested and results show undesirable tradeoffs (Morran, 2004; Rämö, 2001; V. Uyak, Yavuz, Toroz, Ozaydin, & Genceli, 2007). For instance, it was found that chlorination induced DBP formation, and although ACF as a process can effectively remove DBPs, it has the downfall of ineffectively removing lower molecular mass (LMM) organics. It is worth noting that a major argument against coagulation as a pretreatment technology lies in the fact that organic contaminants are not in any respect degraded or destroyed but are simply transferred from the aqueous medium to a solid medium for easier handling. This in turn means that coagulants added are not very recyclable and any effort in recycling them will be an added cost to the pretreatment process.

TiO_2 Based Photocatalysis

One of the recent emerging areas of contaminant degradation is heterogenous photocatalysis. Heterogenous photocatalysis has seen a markedly swelling of interest for several reasons including abundance and relative cost effectiveness of semi-conductor materials employed, complete mineralization or degradation of the organic contaminant in-situ, and a remarkably increased performance of photoactive materials utilized over

the years. Briefly, a photocatalytic process involves a reaction that is preliminarily activated by the absorption of a photon with ample energy to overcome the band-gap energy of the photoactive material used. The band-gap energy is in essence the difference in energy between the valence band (VB) – where the semi-conductor's valence electron is in its ground state – and the conduction band (CB) which is the higher energy level the electron temporarily resides about during photoexcitation. Upon photoexcitation, the electron leaves a 'hole' at the VB whereby allowing the generation of oxidizing radicals. Thus, it is during the intermittent time that the electron is at the CB that photodegradation of a contaminant is feasible due to the near-simultaneous generation of oxidizing radicals. However, depending on the photocatalytic material employed, the electron/hole recombination rate varies – presenting a prominent challenge in the case where the recombination rate is high. Simply, in the scenario that the recombination rate exceeds the time it takes to generate an oxidizing radical, the photoexcitation process is essentially wasted, subsequently decreasing the apparent photoactivity and quantum efficiency of the photocatalyst.

It has been noted that conventional pretreatment techniques have severe innate deficiencies in the effective removal of organic dyes from wastewater. Synthetic azo dyes typically have a rather high affinity to be chemically stable and photolysis of contaminated wastewaters have seemingly no effect. This claim has been assuredly verified by Forgacs whereby 11 out of 18 azo dyes selected for the study passed through the pretreatment processes (activated sludge) essentially untreated (P. Zhou, Wang, Y., Xie, C., Chen, C., Liu, H., Chen, R., ... & Wang, S. , 2017).

The field of photocatalysis found a growing interest to tackle the aforementioned predicament. A slew of different photocatalytic materials have been developed, each with a varying degree of photoactivity, chemical and thermal stability, recyclability, adsorptive capacity, and predominant application field of interest and further development. Titanium dioxide has perhaps been the single-most investigated and developed photocatalyst owing to several unique characteristics. Its exceptional photo and chemical stability, relative abundance, nontoxicity, and cost-benefit properties have promoted its use in a myriad of different applications over the years (Ge, 2016; Lacombe, 2014). As is the case with material science generally, once a material with advantageous properties to a seemingly niche field of interest is fabricated, further developments and modifications are soon to follow. This was in fact the case with TiO_2, but with an exponential growth of interest over the past few years, as is deduced from **Figure 4** (Lacombe, 2014).

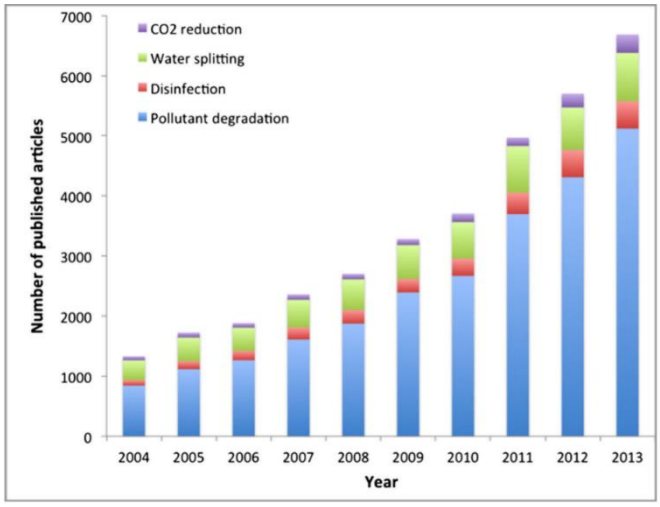

Figure 4 – Number of Research Articles Published between 2004-2013 in the Field of Heterogenous Photocatalysis (Lacombe, 2014)

Certain intrinsic properties of TiO_2 renders a limit to its photocatalytic efficiency (PCE) with organic contaminant degradation. Namely, a relatively low adsorptive capacity and surface area limit the amount of active adsorption sites available for a photodegradation phenomenon. Moreover, TiO_2 has a band-gap energy of approximately 3.2 eV for anatase and 3.0 eV for rutile (Hossain, 2010). This is a comparably high band-gap energy which amounts to only 3-5% of solar photons having enough energy to initiate a photoexcitation event. The high degree of essentially redundant photons that continue to bombard the semi-conductor during solar irradiation are simply wasted. Innately, TiO_2 has a disadvantageously high electron-hole recombination rate which, as previously mentioned, significantly reduces its PCE and quantum efficiency. Although the aforementioned drawbacks are significant, researchers have found creative ways to tackle each one of them. Unfortunately, due to the complex effects that may be introduced when a material is modified, it is not uncommon for an advantageous change in one of those drawbacks to unwittingly negatively affect another property detrimental to the photocatalytic process.

In order to achieve a highly photoactive material, the brevity and complexity of a multitude of parameters need to be fine-tuned simultaneously and effectively in order to achieve expedient results. Over the years, several techniques have been developed to undertake these impediments such as coupling with other semiconductors, combining with carbon-based materials, modification with metals and/or metal oxides, and cation and anion doping (Asahi, 2001; Burri, 2007; Pozan, 2014; Vijayan, 2010). Unrevealingly, these modifications have had hampered effects in extending the spectral

response of TiO_2 materials to visible light, therefore most visible light and infrared (IR) energy is still wasted as previously noted.

As was previously touched upon, in order for the fundamental redox reaction to be favorably facilitated atop the photocatalyst's surface, certain steps need to occur almost instantaneously. A photon with ample energy to overcome the photoactive material's bandgap needs to photoexcite an electron from its ground state VB to an excited state – the CB. During the very brief transition period the electron is at the CB, it is necessary to react with an oxidant to generate a reduced species. Simultaneously, the generated hole is to react with a reductant to effectively generate an oxidized product. Generally in water systems, the photoexcited electron reacts with diatomic oxygen – either part of the DO or from surface oxygens – to produce superoxide radicals (O_2^-•), and the generated hole either oxidizes an organic contaminant or reacts with available water molecules, resulting in hydroxide radical (•OH) which can easily oxidize organic contaminants. Pertaining to the aforementioned generally accepted photodegradation mechanism, a pertinent reaction scheme that inevitable results in an organic compound's degradation at the photocatalyst's surface is briefly shown below (Zollinger, 1991):

$TiO_2 + h\nu\ (UV) \rightarrow TiO_2\ (e_{CB}^- + h_{VB}^+)$

$TiO_2\ (h_{VB}^+) + OH^- \rightarrow TiO_2 + \bullet OH$

$TiO_2\ (h_{VB}^+) + H_2O \rightarrow TiO_2 + H^+ + \bullet OH$

$TiO_2\ (e_{CB}^-) + O_2 \rightarrow TiO_2 + O_2^-\bullet$

$O_2^-\bullet + H^+ \rightarrow HO_2\bullet$

Azo Dye (i.e. MO, MB, etc.) + •OH (or e_{CB}^- or h_{VB}^+) → Degradation Products

where $h\nu$ is the required photon energy in eV, and 'Degradation Products' can namely be smaller organic intermediates that are further degraded into CO_2 in the case of complete

mineralization. The degree of complete mineralization can be confirmed using Total Organic Carbon (TOC) analysis.

Retainment of Photocatalyst

A quite significant factor that becomes detrimental in the practical utilization of nanocomposite systems, is the prerequisite of allowing for a retainment mechanism of the NP composite. Therefore, separating the active photocatalyst composite from the treated water and then retaining them in the photoreactor for further use is of paramount importance to the feasibility of the process, and to ensure the cyclability of the TiO_2-based photocatalyst is being utilized appropriately and sustainably. Some work has been done with photocatalysts being coated upon a paramagnetic iron core which can be collected when passed through a magnetic field (Chalasani, Cyclodextrin-functionalized Fe3O4@ TiO2: reusable, magnetic nanoparticles for photocatalytic degradation of endocrine-disrupting chemicals in water supplies; H. Liu, Jia, Z., Ji, S., Zheng, Y., Li, M., & Yang, H. , 2011; Xin, 2014).

Enhancement Techniques to Photoactive TiO_2 Nanostructures

Owing to the relatively recent discovery of black TiO_2 nanoparticles (NPs), a new untrodden pathway has been cleared for the long wavelength optical absorption TiO_2-based materials, which serendipitously allowed for growing interest in TiO_2 application in a myriad of solar energy systems (Naldoni, 2012; H. Pan, Zhang, Y. W., Shenoy, V. B., & Gao, H., 2011; Syzgantseva, 2011; G. Wang, Wang, H., Ling, Y.,

Tang, Y., Yang, X., Fitzmorris, R. C., ... & Li, Y. , 2011). The presenting physics of black, or reduced, TiO_2 absorbs in the visible and IR wavelength region (X. Chen, Liu, L., Liu, Z., Marcus, M. A., Wang, W. C., Oyler, N. A., ... & Guo, J. , 2013). The intra-band states of black TiO_2 are located between 0.92 to 1.37 eV below the conduction band edge (Z. Wang, Yang, C., Lin, T., Yin, H., Chen, P., Wan, D., ... & Jiang, M. , 2013), which in turn allows for a visible light photon to initiate photoexcitation and generate an electron-hole pair. This increase of utilized photons in the visible light and IR bands of the solar spectra can be seen in **Figure 5** below.

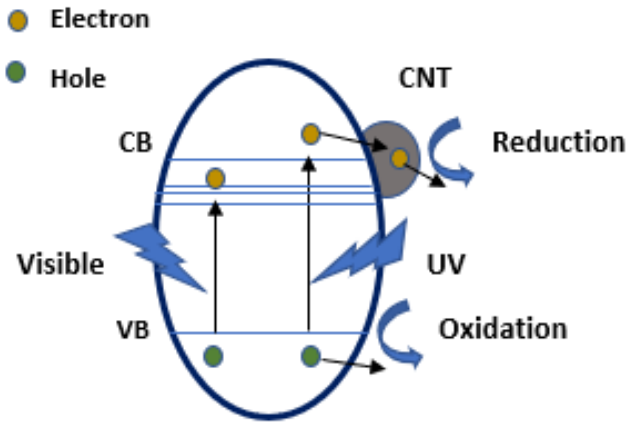

Figure 5 - Schematics of visible light responsive photocatalytic activity of TiO_2/CNT

Briefly, since the initial discovery of black TiO_2 photoactive nanomaterial several techniques have been employed to yield colored – namely black – titania. Following the same general method of reducing pristine titania in its ground oxidation state of Ti^{4+} to its Ti^{3+} reduced state, high-pressure hydrogenation was successfully utilized. 20 bar H_2 atmosphere was reportedly used with a constant temperature of 200 ºC for 5 days (X. Chen, Liu, L., Peter, Y. Y., & Mao, S. S. , 2011). The exposure time

led to varying degrees of reduced TiO_2 – which is easily observed by the depth of their dark color change. A similar hydrogenation reaction was also performed whereby a higher pressure hydrogen atmosphere (35 bar) was utilized at room temperature, and the varying parameter was also the allowed reaction time – namely 0-20 days (C. Zhang, Yu, H., Li, Y., Gao, Y., Zhao, Y., Song, W., ... & Yi, B. , 2013). On this note, anatase TiO_2 was fabricated under atmospheric pressure for 1 hour, however annealing temperatures ranging from 200-600 ºC were used (C. Zhang, Yu, H., Li, Y., Gao, Y., Zhao, Y., Song, W., ... & Yi, B. , 2013). Hydrogenation of anatase TiO_2 was later achieved through a mixed atmosphere of hydrogen/argon for 5 hours at 400-600 ºC (Zhu, 2012). Interestingly, there was an expected shift from direct hydrogenation due to the relatively high temperatures and/or pressures needed, which posed a high safety issue. As such, black TiO_2 nanomaterials were successfully fabricated under argon atmosphere using 400-600 ºC for 5 hours. The annealed sample was a TiO_2 gel which was formulated using $TiCl_4$ as the titania precursor along with a mixture of HF and urea. Depending on the amounts of urea and HF in the un-annealed sample, the degree of reduction can be controlled (Jianfeng Yu et al., 2007). Amongst the different reduction techniques investigated, chemical reduction using aluminum (Jianfeng Yu et al., 2007), imidazole (Zou, 2013) and calcium hydride (Tominaka, 2011) have shown increased utilization, and in particular sodium borohydride facilitated reduction (Kang, 2013). Chemical oxidation (X. Liu, Gao, S., Xu, H., Lou, Z., Wang, W., Huang, B., & Dai, Y. , 2013) and electrochemical reduction (C. Xu, Song, Y., Lu, L., Cheng, C., Liu, D., Fang,

X., ... & Li, D., 2013) methods have also been investigated and black TiO_2 nanomaterials have successfully been fabricated from both.

As is the nature of TiO_2-based semiconductors, there's an impediment from the unfavorably fast electron-hole recombination rate, which means that a photoexcited electron in the cathode band will recombine back into its valence band before reaching the surface of the catalyst to initiate a favorable photocatalytic degradation. It has therefore been postulated that the addition of a high electron acceptor, such as carbon nanotubes (CNTs), should promote electron-hole separation, effectively decreasing the electron-hole recombination rate. This in turn will allow for a more relaxed time for the photoexcited electron to be accepted by the skeletal CNTs and travel to the surface, thereby allowing for a higher probability of photocatalytic degradation of an organic. This in turn leads to an effective higher photocatalytic efficiency (X. Chen, Liu, L., Peter, Y. Y., & Mao, S. S. , 2011; Li, 2011). In an initial effort to visualize the improved light absorption ability of black TiO_2 NPs, as opposed to pristine TiO_2 NPs, **Figure 6** shows the UV-Vis absorption spectra (Wu, 2017). The absorption spectrum of CNTs, in accordance with literature, shows that CNTs absorb approximately 100% of solar light reaching Earth's surface (L. C. Chen, Ho, Y. C., Guo, W. S., Huang, C. M., & Pan, T. C, 2009). Quite simply, the darker a material is, the more visible light it will absorb. Therefore, a higher degree of reduction of pristine TiO_2 NPs will lead to a higher absorption spectrum of the resultant reduced black TiO_2 NPs.

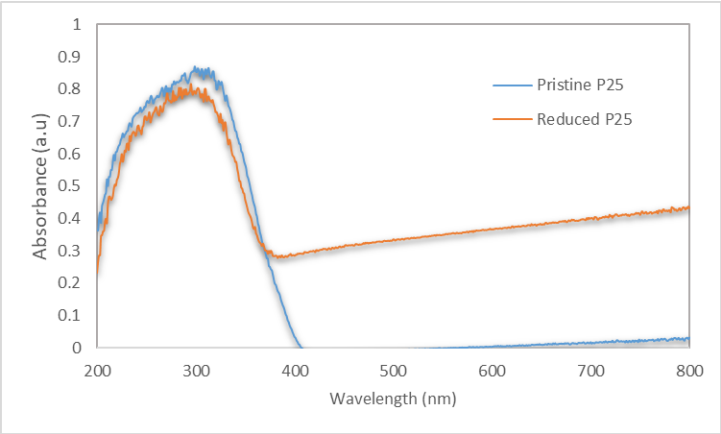

Figure 6 – UV-Vis adsorption spectra of pristine TiO_2 and reduced TiO_2

Effect of Nano-morphology and TiO_2 Crystalline Phase on Photoactivity

In an effort to further curb the fundamentally disadvantageous effect of a fast electron-hole recombination rate in TiO_2-based photocatalysts, a morphological change can be utilized to reduce this phenomenon. Allowing for nanowire/nanorod (NW/NR) growth from the spherical nanoparticle precursor is expected to reduce the electron-hole recombination rate, since it would allow for an axial path for the electrons to conduct through. Photoactive titania nanowires were also reported to have high chemical stability and facilitate ample space for nucleation (G. Chen, Ji, S., Li, H., Kang, X., Chang, S., Wang, Y.,Liu, H, 2015; Tian, 2015). However, employing a predominantly axial morphology comes with some consequences. This is due to the photocatalytic charge density being higher in the initial spherical morphology. Nonetheless, utilizing a nanowire framework along with the dendritic structure of CNTs (or MWCNTs) would allow for better intertwinement with the active reduced TiO_2-based nanowire

photocatalyst. This in turn can be advantageous in increasing the cyclability of the amalgamate nanocomposite being used.

Moreover, due to the inherent high surface area, a NW morphology allows for the presence of more adsorptive sites essential in enhancing the apparent PCE of the system (X. Wang, Li, Z., Shi, J., & Yu, Y., 2014). However, the overarching cost-benefit of changing the TiO_2 morphology from NPs to NWs has been challenged and no concrete consensus has been reached on which morphology facilitates higher photoactivity. For instance, Zhao et al. concluded that titania NPs showed higher photoactivity at degrading Rhodamine B (RhB) (Fu, 2018). In their work, titania NPs were initially fabricated and then hydrothermally grown to NWs. The titania NWs were later decorated by NPs and a nano-heterostructure was successfully fabricated – resulting in a higher photoactivity than either stand-alone morphologies. The higher photoactivity of NPs than NWs was attributed to their smaller particle size and more crystalline structure. It is worth noting that due to the nature of nanowires to not have unidirectionality in growth and depending on the addition of certain templating and facilitating agents during NWs growth, crystallinity is usually significantly effected and an unfavorably predominant amorphous product can be generated. However, the degree of crystallinity can be controlled by sound chemical procedures and calcination steps.

Phase crystallinity of the final titania-based nanomaterial has been found to be a parameter of paramount importance to photoactivity and PCE of organic degradation. Succinctly, TiO_2 has four mineral or crystalline forms: anatase, rutile, brookite, and titanium dioxide (B). In photocatalysis, it was found that in a predominantly anatase

phase crystalline TiO_2-based material, high photoactivity can be obtained (Luttrell, 2014; Ohtani, 2010). Generally, anatase comprises of a tetragonal system with a bipyramidal pattern. The crystalline structure is an important factor in determining the effective band-gap energy of the final photocatalyst – although morphology, surface defects, and oxygen vacancies are also major factors in manipulating a semi-conductor's band-gap energy. Rutile is reported to have a tetragonal structure with a prismatic pattern and brookite, has an orthorhombic crystalline structure. There have been several explanations as to why anatase seems to be the photoactive phase in TiO_2.

Anatase TiO_2 is characterized by having an indirect band-gap, and such indirect band-gap semiconductors have been reported to exhibit a longer charge carrier life than direct band-gap semiconductors (M. Xu, Gao, Y., Moreno, E. M., Kunst, M., Muhler, M., Wang, Y., ... & Wöll, C., 2011). Fundamentally, anatase has a slightly higher band-gap energy than rutile TiO_2 – approximately 0.25 eV higher – and an increase in band-gap energy subsequently increases the oxidative power of the photogenerated electron, whereby allowing for a more spontaneous transference of the electron from the photoexcited TiO_2 to the adsorbed target contaminant (Batzill, 2011; J. Pan, Liu, G., Lu, G. Q., & Cheng, H. M., 2011). Comparatively, rutile TiO_2 is generally formed above calcination temperatures exceeding 500-600 ºC. It has been reported that calcination at higher temperatures promotes nanoparticle agglomeration which disadvantageously reduces the exposed surface area of the photocatalytic nanomaterial – also leaving 'inner core' titania NPs uselessly shielded from incoming irradiation flux. Although both rutile and anatase TiO_2 phases have a rather high electron-hole recombination rate, the latter

has a comparatively higher rate, which again reduces the apparent photoactivity of the material. Surface defects are also more concentrated in the anatase phase, compared with the other TiO_2 crystalline phases. This in turn can be advantageous in the generation of more oxygen vacancies – which can act as electron sinks in effect reducing the electron-hole recombination rate. Although anatase has several facets, namely {101}, {001}, {110}, {100}, etc. it has been found that the {101} facet has the lowest surface energy (0.44 J/cm^2) which substantiates its strong reduction capabilities. Therefore, an anatase material with a predominant {101} facet – which can be determined from XRD analysis – should theoretically serve as an exception photocatalyst for water-splitting applications. The 2-theta diffraction peak located at 25.3º corresponds to anatase phase {101} facet – as can be seen from **Figure 7** below (Sussman, 2013). An X-Ray Diffraction (XRD) plot of a TiO_2-based nanocomposite with a strong peak at 25.3º would thus preliminarily indicate a good photoactive predominant anatase phase material.

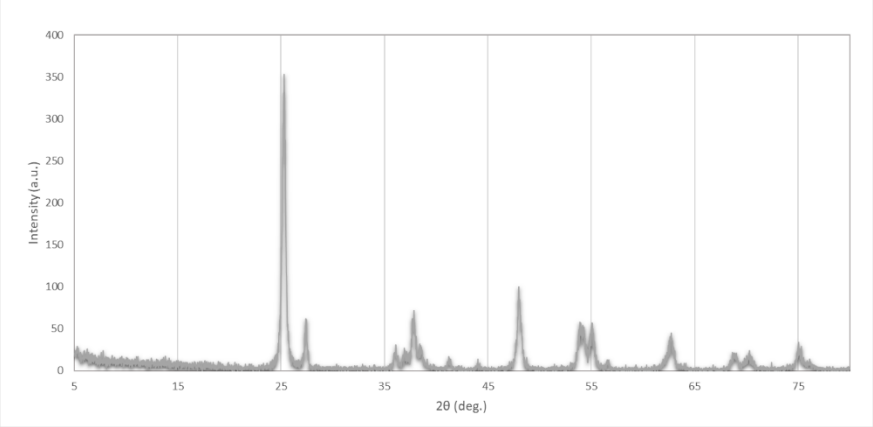

Figure 7 – XRD of Commercial TiO_2 NP (P25) comprising of 78% anatase, 14% rutile and 8% amorphous phase (Sussman, 2013)

Incorporation of Carbon Nanotubes with TiO_2 Nanocomposites

As was mentioned previously, several morphologies of titania have been fabricated over the years with varying degrees of photoactivities. Through a precipitation method followed by mild calcination at 400 ºC in air, Manorama et al. fabricated titania nanoparticles whilst controlling the percentage and crystallinity of the photoactive anatase phase (Reddy, 2003). One-dimensional morphologies such as nanotubes, nanowires, nanoribbons, and nanorods have all been effectively synthesized by a 'one-pot' alkaline – namely concentrated sodium hydroxide solution (NaOH) - hydrothermal method using a range of temperatures (130-200 ºC), templating agents (ethanol), aqueous NaOH concentrations, reaction times, and titania precursors (i.e. P25, titanium Isopropoxide (TTIP), titanium (IV) butoxide (TBOT), etc.) (Anas, 2016; G. Rao, Brastad, K. S., Zhang, Q., Robinson, R., He, Z., & Li, Y. , 2016; G. Rao, Zhang, Q., Zhao, H., Chen, J., & Li, Y. , 2016; Rao, 2017; Yoon, 2017; Q. Zhang et al., 2015; Zhao, 2017). Fine tuning those parameters have yielded several one-dimensional morphologies for TiO_2. In an effort to reduce electron-hole recombination of titania, one study reports the incorporation of titania NPs with one-dimensional CNTs to formulate a 3-dimensional urchin like structure with high PCE for degrading methylene orange (MO) (Y. Zhang, Xing, Z., Yang, S., Zhou, W. , 2017). Due to the advantageous properties of CNTs, several reported works have shown its incorporation with different morphological TiO_2 structures and under different synthesis procedures such as mechanical mixing of TiO_2 and CNTs (Kuo, 2009), sol– gel synthesis of TiO_2 in the presence of CNTs (Hu,

2011), electro-spinning methods (Aryal, 2008), hydrothermal (Muduli, 2009) and chemical vapor deposition (H. Yu, Quan, X., Chen, S., Zhao, H., & Zhang, Y., 2008).

Effect of Doping on Photoactivity

As was previously mentioned, amongst the different methods utilized to enhance the photoactivity of TiO_2-based nanomaterials and nanocomposites, doping has been a major area of focus especially prior to the discovery of black titania. Briefly, doping can be subdivided into different groups – namely metal, non-metal, and co-doping. Doping has been used to reduce the electron-hole recombination rate and to simultaneously increase the visible light absorbance of the photocatalyst.

Metal doping involves the surface incorporation of transitional group metals, which serve two main goals. Firstly, it has been found that metal doping enhances the adsorption of pollutants whilst also favorably reducing the electron-hole recombination rate (H. XingGang, 2009; Tieng, 2011). The effective charge-transfer amongst d-electrons in transitional metals and the CB/VB of titania allows for a shifting in the light absorption of the final amalgam. Notwithstanding, metal doping has several drawbacks that directly affect the advantageous properties of TiO_2. Due to their relatively expensive preparation methods and low thermal stabilities, they are unfavorably reducing the innately high stability of the focal TiO_2 (H. XingGang, 2009). Metal leaching out from poorly recyclable materials posed a major environmental issue for the utilization of metal-doping in water treatment applications. Moreover, there's an inherent increased risk with metal doping due to an increasingly high carrier charge recombination probability.

In the progression of TiO_2 modification, non-metal doping was the next logical step to theoretically and cost efficiently increase the absorption spectra of the final photocatalyst without suffering from the poor thermal stability and other predicaments of metal doping. Increased attention has been dedicated to specific non-metal doping for TiO_2, especially nitrogen (A.E. Giannakas, 2012), sulfur (H. U. Lee, Lee, S. C., Choi, S. H., Son, B., Lee, S. J., Kim, H. J., & Lee, J. , 2013), and carbon (Górska, 2008). Although visible light activation has been achieved, low quantum efficiency has been the main drawback of non-metallic doping. It is important to recognize the reasoning behind the varying degree of contribution doping generally has. Amongst several factors, the synthesis method and the nature of the dopant are two of the most important factors effecting the final efficiency. Once the dopant is in the host lattice, the coordination setting is determined by both the nature of the dopant and the host lattice – which allows for perpetual variations of different allowable doped photocatalysts with varying effects (Yuan, 2011). To further manipulate a favorable doping effect, recent progress has been made with TiO_2 co-doped photocatalysts (P. Zhou, Yu, J., & Wang, Y. , 2013). **Table 1** below summarizes some of the compiled findings pertaining to different dopants used with TiO_2. These results were obtained using different photocatalytic reactors, preparation methods of photocatalysts, and different parametric variations in reaction conditions, which as will be discussed can have significant consequences on the obtained photocatalytic efficiencies. All below results have been compiled from sources using

UV-light as the irradiation source.

Dopant Type	Synthesis Methodology	Dopant Identity	Initial Concentration of MO (ppm)	Photocatalyst Loading (g/L)	Reaction Time (min)	Removal Efficiency (%)	Reference
Metal	Sol-gel	Ho	20	1	15	99	(Heshan, 2008)
		Fe	40	2	9	80	(Shi, 2007)
		Ce	10	2.5	120	58	(Q. Wang, Xu, S., & Shen, F., 2011)
	Precipitation	Gd	20	2	150	98	(Lv, 2011)
Non-metal	Sol-gel	S	20	1	50	95	(H.T. Gao, 2011)
		N	20	1	50	100	(H.T. Gao, 2011)
	Hydrothermal	N	20	0.1	45	99	(Peng, 2008)
	Impregnation	F	20	0.5	120	100	Y. Yu, Wu, H. H., Zhu, B. L., Wang, S. R., Huang, W. P., Wu, S. H., & Zhang, S. M. (2008)
Co-doped	Sol-gel	Fe-Ho	40	2	9	97	(Shi, 2007)
		N-S	20	0.4	100	98	(H.T. Gao, 2011)
		Ce-N	10	0.4	120	95	C. Liu, Tang, X., Mo, C., & Qiang, Z. (2008)
	Solvothermal	N-La	30	3	120	100	(X. Zhang, Zhou, G., Zhang, H., Wu, C., & Song, H., 2011)

Table 1 – Summary of Reported Doped TiO_2 Photodegradation of MO

CHAPTER III

RESEARCH METHODOLOGY

Experimental Setup

A quartz petri dish was used as an effective batch reactor, whereby 50 mL of the reactor was filled with the contaminated synthetic water – containing a predetermined amount of photocatalyst dose - at the beginning of each photodegradation experiment. The light source utilized was from an artificial solar simulator working at, base case, 700 W/m^2 light intensity. The solar simulator was rigorously calibrated using a standard pyranometer (CMP6 Kipp & Zonen with a spectral range of 285-2800 nm) preceding any change to illumination intensity change throughout the course of the work.

Prior to the addition of the 50 mL volume to the model reactor, 50 mL of synthetic contaminated water (MO, 10ppm) was collected from a 0.5 L stock solution (MO, 10ppm). The appropriate amount of powder photocatalyst was carefully weighed on a calibrated balance and added to the 50 mL synthetic water. Subsequently, a tip-sonicator (Q-Sonica Q700 used at low amplitude for 30 seconds) was used to obtain a homogenous mixture of the photocatalyst in the synthetic water volume. SEM analysis was performed on the photocatalyst materials before and after sonication to ensure that no morphological change to the nanostructure inadvertently occurred.

Adsorption effects were factored for each photodegradation experimental run. Namely, upon the addition of the synthetic water volume (containing the photocatalysts) to the petri dish, the reactor was covered with aluminum foil (dark conditions) and stirred (200 RPM) for 1 hour. This allowed for adsorption/desorption effects to be investigated and for an equilibrium to be reached prior to any photocatalytic activity to be initiated under light irradiation.

For the screening experiments to evaluate the photoactivity of the different synthesized photocatalysts, the only variable that was investigated was the photocatalyst material added to the water that contains MO. Parameters such as pH (6.5), photocatalyst load (1 g/L), standard room temperature, initial MO concentration (10 ppm), and light intensity (700 W/m^2) were constantly maintained in these experiments. Other sets of experiments were performed to evaluate the effects of experimental conditions for the promising photocatalysts that were identified by the screening experiments.

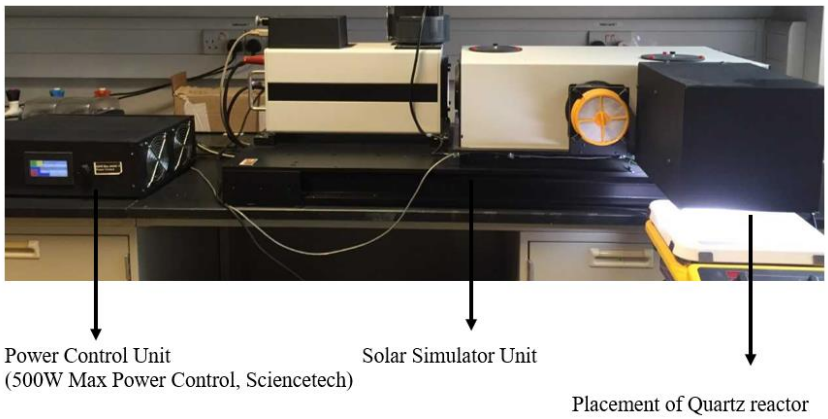

Figure 8 – Depiction of photodegradation experimental setup

Samples were taken at the desired reactions times using a 10 mL disposable syringe and immediately filtered using a 0.45 μm mixed cellulose-ester filter paper obtained from Advantec. The filtered aliquots were stored in 10 mL scintillated glass vials until analysis for MO using UV-Vis-NIR spectrometer.

Synthesis of Photoactive Samples

In order to effectively investigate each progressive synthesis step – namely morphology change, surface treatment, calcination, MWCNT incorporation, and reduction – an array of samples have been synthesized.

Upon successful fabrication of each set of sample groups, their photoactivity in degrading MO was undertaken using the photodegradation experimental setup explained above. A comparative study and investigation based on several material characterization techniques (discussed later) aided in a well-rounded understanding of the material aspects that predominates photoactivity. It is to note that lab glassware was cleaned prior to use in any synthesis by first soaking in DI water and soap, then rinsed with DI water, then soaked in 0.1M HCl solution, then rinsed again with DI water, and finally left to air dry.

Pristine TiO_2 nanoparticles (pTNP) were synthesized via a modified solvothermal methodology reported previously (J. S. Chen, Tan, Y. L., Li, C. M., Cheah, Y. L., Luan, D., Madhavi, S., ... & Lou, X. W, 2010). Essentially, 3.64 mL of as-purchased Titanium Isopropoxide (TTIP) were added to a well-mixed solution of 70 mL isopropyl alcohol (IPA) and 0.8 g ethylenediaminetetraacetic acid (EDTA). The solution

was left under vigorous stirring for 20 minutes and then transferred to a Teflon-lined stainless-steel autoclave and placed in the oven for 24 hours at 150 ºC. The resultant white pulp was then washed and centrifuged at 6000 RPM three times with DI water and once with ethanol, then calcinated at 500 ºC in a muffle furnace for 2 hours.

Pristine TiO_2 nanowires with incorporated MWCNTs (pTNW/MWCNT) were synthesized using a modified procedure performed previously (G. Rao, Brastad, K. S., Zhang, Q., Robinson, R., He, Z., & Li, Y. , 2016). Briefly, 1.0 g of P25 powder and 5 w% MWCNT were added to aqueous NaOH (35mL, 10M) solution under vigorous stirring in a 100 mL Pyrex beaker for 15 minutes. 35 mL of DI water was then added and stirring was continued for an additional 15 minutes to obtain a homogenous suspension of TiO_2 nanoparticles (NPs) with the MWCNTs. It was found that the addition of ethanol was disadvantageous, and therefore ethanol was eliminated in later syntheses, and a 70 mL NaOH (10M) aqueous solution was used. The mixture was quickly added to a Teflon-lined container (30% headspace by volume) and enclosed in a stainless-steel autoclave. A solvothermal reaction was then facilitated by keeping the autoclave in a thermostatic oven at 180 ºC for different times – namely 20 and 42 hours – to test the effect of NW growth on solvothermal reaction time. The resultant grayish pulp was washed and centrifuged at 6000 RMP with 0.1M HCl, DI water and ethanol several times. The pulp was then vacuum dried prior to surface treatment (discussed below), or directly calcinated at 450 ºC for 4 hours. Using a higher calcination temperature can result in an unfavorable phase shift and more importantly can cause combustion of MWCNTs.

pTNW/MWCNT samples were also fabricated by replacing P25 as the titania precursor and using pristine TNP fabricated using Titanium Isopropoxide (TTIP) as the precursor. Pristine TiO_2 nanowires with incorporated Activated Carbon (AC) were also synthesized using the same procedure described above, by simply replacing the MWCNTs with AC which was obtained by grinding granular AC.

A two-step surface treatment procedure was performed for some samples in order to test the surface treatment effect on the as-prepared materials. This step was performed after the final morphological change – NP to NW – and prior to the final calcination step that was adapted from Tian et al. with some modification (J. Tian, 2016). After complete washing of samples – method previously discussed – they were stirred in 0.5M HCl for 24 hours. This was followed by a thorough washing with DI water. The samples were then isolated by centrifugation at 6000 RPM and vigorously stirred in 70 mL of diluted sulfuric acid (0.02M) for 30 minutes. Upon reaching a homogenous mixture, the solution was transferred to a Teflon-lined stainless-steel autoclave and heated to 120 ºC for 5 hours. Samples that underwent this surface treatment step were then calcinated at 450 ºC for 4 hours.

To further test the effect of having effective heterojunctions between titania NWs and NPs, a TiO_2 nano-heterostructure was effectively fabricated using a modified method proposed by Fu et al. (Fu, 2018). to synthesize pTNW/pTNP/MWCNT, pTNW/MWCNT was first synthesized using the aforementioned procedure, ostracizing the surface treatment step. Fu found that an equimolar deposition of TNP on TNW yielded the highest photoactivity, and as such an equimolar nano-amalgam was

fabricated as follows: a 1.05 g of calcinated pTNW/MWCNT was added under stirring to 70 mL of IPA solution – containing 0.25 g of dissolved EDTA. The sample was sonicated using a tip-sonicator (15 amplitude) for 2 minutes in order to achieve homogeneity. Subsequently, a volume of 3.64 mL TTIP was added such that upon hydrolysis an equimolar amount of TNP to TNW are formed. The solution was stirred for another 15 min then swiftly transferred to a Teflon-lined stainless-steel autoclave, whereby solvothermal hydrolysis of the TNP was facilitated at 150 ºC for 24 hours. The resultant pulp was then washed and centrifuged several times with DI water. Lastly, the same surface treatment and calcination steps as described above were carried out.

All titania-based nano-composites were effectively fabricated through a simple mechanochemical reduction step using sodium borohydride ($NaBH_4$). An optimized molar amount of $NaBH_4$: Titania – namely 1.25:1 – was collected and thoroughly mixed for 10 minutes using a Agate pestle and mortar. The powder mixture was transferred to a ceramic crucible and placed in a tubular furnace. Prior to heating, the system was vacuumed to remove any oxygen in the reactor's volume and then purged with Argon until atmospheric pressure was restored. Reduction was carried out at 380 ºC for 2 hours following 1 hour heating time. The reaction was facilitated under 150 sccm of Argon flow. The sample was cooled to room temperature prior to opening the reactor and extracting the crucible. This procedure allowed all unreacted $NaBH_4$ to cool to room temperature in order to allow safe handling during the following washing step (Ariyanti, 2017). The as-prepared samples were then washed and centrifuged several times using

DI water and ethanol. Finally, the collected samples were vacuum dried overnight at 80 ºC.

Pertaining to the syntheses of the final recoverable photoactive samples, an unsuccessful attempt at direct surface attachment of the photoactive titania-based nanocomposites to the silica-coated iron microsphere cores led to a different strategy of formulating the final paramagnetic and photoactive samples. Essentially, the photoactive titania-based catalyst was grown atop the silica-coated paramagnetic iron microsphere cores. A refined synthesis scheme to that of Yu et al. was employed (X. Yu, Liu, S., & Yu, J. , 2011). Firstly, fabricating paramagnetic Fe_3O_4 microspheres was performed using a hydrothermal procedure. Iron chloride hexahydrate ($FeCl_3 \cdot 6H_20$, 2 g) was dissolved in 70 mL ethylene glycol, followed by the addition of sodium acetate (NaAc, 5 g) and polyethylene glycol (1 mL) under continuous stirring for 30 minutes. The solution was then transferred to a 100 mL Teflon-lined stainless-steel autoclave, whereby the autoclave was heated at 170 ºC for 10 hours in a thermostatic electric oven, then allowed to cool to room temperature prior to further processing. The resultant brown-black pulp was washed and centrifuged several times with DI water and ethanol, then vacuum dried at 70 ºC overnight.

It was previously reported that an unfavorable heterojunction occurs during the surface attachment of Fe_3O_4 and titania (Song, 2007). Therefore, a barrier silica layer was found to effectively shield the active titania from direct contact with the paramagnetic iron oxide. Briefly, using a modified Stöber methodology, an amorphous, inert and thermally stable silica coating can be introduced atop the iron core at ambient

conditions (Song, 2007). 100 mg of Fe_3O_4 microspheres were dissipated in 100 mL solution of IPA and water 2:1 volume ratio respectively. An amount of ammonium hydroxide (NH_4OH) was added to adjust pH to pH11. The solution was preliminarily stirred and shortly tetraethyl orthosilicate (TEOS, 400 μL) was added dropwise under stirring. The synthesis beaker was covered, and reaction conditions were maintained for 1.5 hours until a clear gray solution was formed. The silica-coated iron microspheres were collected using a magnet and washed several times with formaldehyde solution, then vacuum dried at 70 ºC overnight.

Growing pTNW atop the $Fe_3O_4@SiO_2$ paramagnetic was achieved through a two-step process. Firstly, depositing pTNP with high surface coverage was achieved by dispersing $Fe_3O_4@SiO_2$ (1 g) in well-stirred solution of IPA (70 mL), dissolved EDTA (0.25 g), and 250 μL of TIIP. Stirring was continued for 30 minutes at room temperature, then the solution was transferred to a 100 mL Teflon-lined stainless-steel autoclave and maintained at 150 ºC for 24 hours. The autoclave was naturally cooled to room temperature. The brown-black pulp was collected via a small magnet, washed and centrifuged several times with DI water and ethanol, then air dried overnight yielding $pTNP@Fe_3O_4@SiO_2$. In order to facilitate titania nanowire growth, 2 grams of the as-prepared sample was mixed in NaOH (70mL, 10M) solution and 5 w% MWCNT were added. The nanowire growth procedure previously discussed was undertaken. In order to maintain a high surface coverage in the final TNW growth upon the silica surface, 1 gram of commercial grade P25 was added to the NaOH solution prior to transference to the autoclave. Obtaining the reduced black $TNW/MWCNT@Fe_3O_4@SiO_2$ followed the

same mechanochemical process discussed previously. No surface treatment was performed on these set of samples. **Figure 9** below briefly demonstrates the synthesis procedure for the retrievable and photoactive nanocomposite.

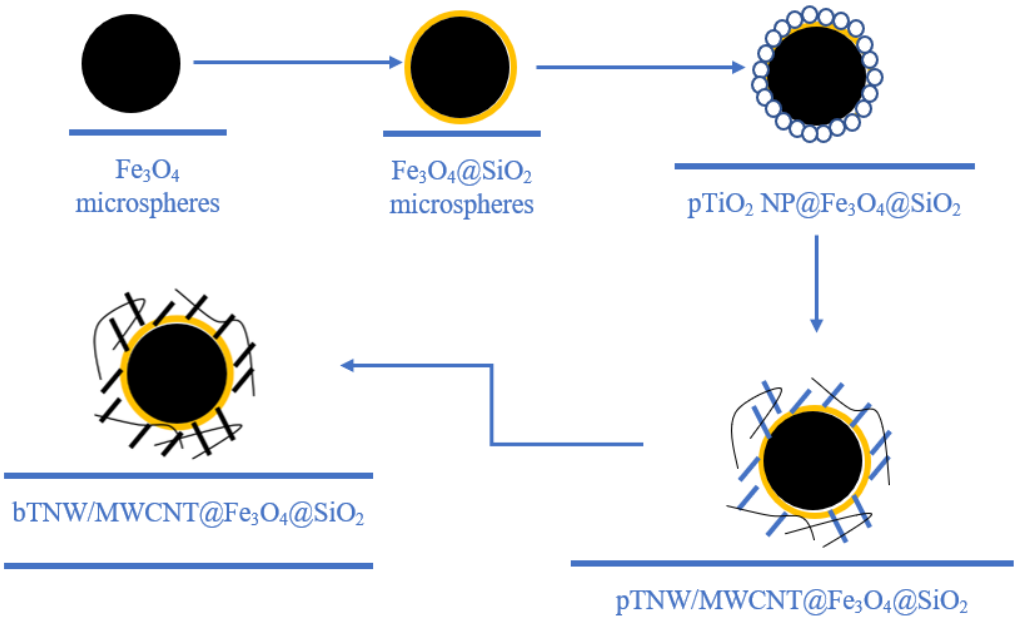

Figure 9 – Schematic depiction of bTNW/MWCNT@Fe_3O_4@SiO_2 fabrication sequence

Table 2 – Chemicals used and their specifications

Chemical	Vendor	Specifications
Methylene Orange	Sigma-Aldrich	ACS reagent, Dye content 85%
Hydrochloric Acid	Sigma-Aldrich	ACS reagent, 37%
Sulfuric Acid	Sigma-Aldrich	ACS reagent, 95-98%
Titanium Isopropoxide	Sigma-Aldrich	99.999% trace metal basis
Isopropyl Alcohol	Sigma-Aldrich	ACS reagent, ≥99.5%
Ethylenediaminetetraacetic acid	Sigma-Aldrich	ACS reagent, 99.4-100.6%, powder
Titanium (IV) Oxide, Aeroxide P25	Fisher Scientific	≥99.5% (based on ignited material) typically
Multi-walled Carbon Nanotubes	Sigma-Aldrich	98% carbon basis, O.D. × L 6-13 nm × 2.5-20 μm
Sodium Hydroxide	Sigma-Aldrich	ACS reagent, ≥97.0%, pellets
Ethanol	Sigma-Aldrich	Laboratory Reagent, 96%

Table 2 Continued

Chemical	Vendor	Specifications
Activated Carbon	Sigma-Aldrich	untreated, granular, ≤5 mm
Sodium Borohydride	Alfa Aeser	0.98%
Iron (III) Chloride Hexahydrate	Sigma-Aldrich	0.98%
Ethylene Glycol	ParChem	99.5 % Min.
Polytheylene glycol	Sigma-Aldrich	average mol wt 200
Anhydrous Sodium Acetate	Kexin Chemicals	≥98.5
Ammonium Hydroxide solution	Sigma-Aldrich	28% NH3 in H2O, ≥99.99% trace metals basis
Tetraethyl Orthosilicate	Sigma-Aldrich	99.999% trace metals basis

Preparation of MO Solutions

Fresh stock solutions of MO were prepared daily prior to utilization in photodegradation experiments. Deionized water (DI water) was used for the preparation of each stock solution, and for the preparation of all solutions used in photocatalytic material fabrications. To prepare the MO stock solutions, 0.005 g of MO powder was added to 500 mL DI water to obtain 10 mg/L of MO concentration and stirred for 45min at 400 RPM using magnetic stirrer.

A calibration curve was obtained by measuring light absorption at 464 nm using the UV-Vis-NIR liquid analysis. Four MO concentrations, 30, 20, 10, and 5ppm, were prepared. First, a 30 ppm MO stock solution was prepared by dissolving 0.015 g MO powder into 500 mL of DI water. Dilution was then performed in order to obtain the lower concentrations of the standard solutions. All 4 samples were run through a

calibrated UV-Vis-NIR solution – using DI water in the reference cuvette – and the below MO calibration curve was obtained.

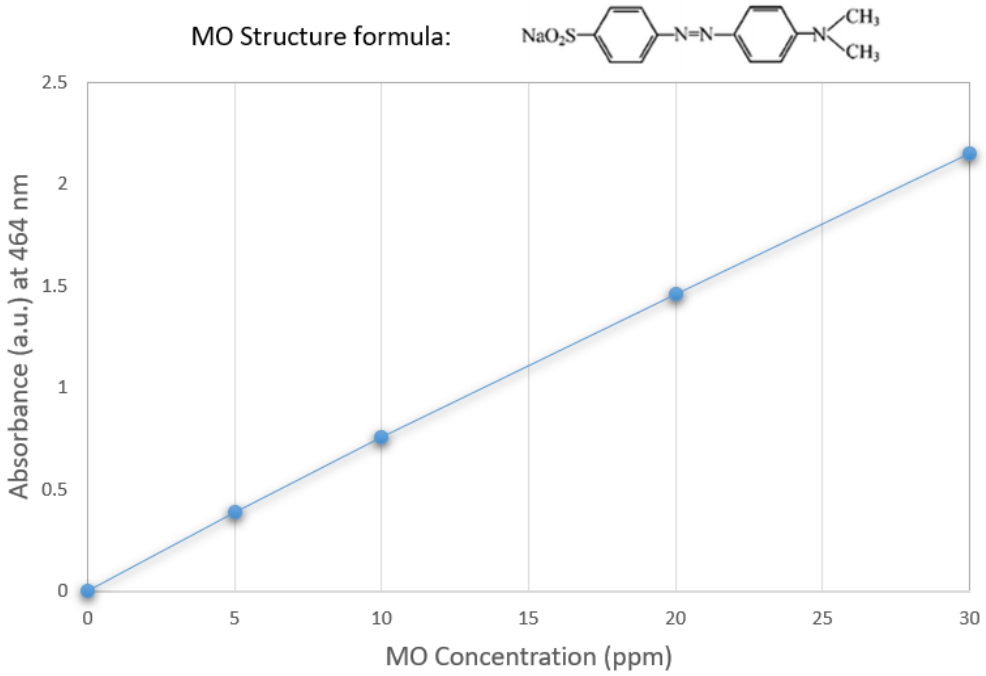

Figure 10 – Methylene Orange UV-Vis-NIR Calibration Curve

Materials Characterization

In order to effectively characterize the morphology and structure of the different samples through the different experimental syntheses, both a Scanning Electron Microscope (SEM, FEI Quanta 400 FEG ESEM) and Transmission Electron Microscopy (TEM, JEOL JEM-2100 FEG TEM) were employed. In order to enhance sample stability during high intensity electron beam exposures of SEM/TEM, the as prepared samples were gold-coated under Argon, as the process gas, in order to enable higher resolution imaging. This was performed using a sputtering device (LEICA, EM

SCD050). EDX and elemental mapping were performed via both integrated SEM and TEM EDX devices. Crystallinity was measured via XRD analysis (Rigaku, Ultima IV) at a 2θ angle scanning rate of 1 º/min. The surface chemical composition and band-gap edges were analyzed using X-ray Photoelectron Spectroscopy (XPS, PHI Quantera XPS) on a PHI-5000C ESCA system equipped with Al Ka as the X-ray excitation source. The microstructure of the samples were analyzed using Raman spectroscopy (Labram-010 equipped with a 632.8nm laser). UV-Vis-NIR diffusion reflectance spectra were realized using a solid-sample unit on a PerkinElmer Lambda 950 Spectrophotometer, which allowed for band-gap energy estimation of the photocatalysts prepared. FT-IR Spectrophotometry analysis was used for functional group identification (Varian 640-IR).

Analytical Procedure for Photodegradation Quantification

In order to effectively determine the degree at which different photocatalyst samples can degrade the contaminant, namely MO, two techniques have been used in this study. Liquid UV-Vis-NIR (PerkinElmer 950 Spectrophotometer) has been used to measure the concentration of MO in the solution. Briefly, the absorption spectra for each liquid sample was obtained between 400-550nm and the maximum absorption of MO was recorded at 464nm. Effectively, this allows quantification of the remaining MO residue present at different sampling times, in turn allowing to calculate the percentage MO degraded at different irradiation times, with different photocatalysts. The percentage degradation can thus simply be calculated using **Eq. 1** below.

$$\text{Degradation (\%)} = \frac{100*(C_o - C_t)}{C_0} \qquad \textbf{(Eq. 1)}$$

where, C_0 is the initial MO concentration and C_t is the concentration of MO after time (t).

Furthermore, in order to study the degradation behavior of MO, first and second order reaction kinetic models were employed. The apparent first (k_1) and second (k_2) rate constant were obtained and tabulated simply by investigating the linear relation in both kinetic models respectively. By comparing the correlation coefficient (R^2) for each photodegradation experiment's respective linear kinetic model plot, it can be deduced which model best describes the degradation behavior observed. The linear form of the kinetic models for first and second order kinetic models can be seen in **Eq. 2** and **Eq. 3**, respectively. Therefore, the linear relation between $-Ln(C_t/C_0)$ vs. time and $1/C_t$ vs. time were used to obtain k_1 and k_2, respectively.

$$C_t = C_0 e^{-k_1 t} \qquad \textbf{(Eq. 2)}$$

$$\frac{1}{C_t} = \frac{1}{C_0} + k_2 t \qquad \textbf{(Eq. 3)}$$

Depending on which kinetic model best fits the degradation behavior, the reaction rate constant obtained for each individual photodegradation system can effectively allow for the quantification of photocatalyst performance on the contaminated water system.

Moreover, to evaluate the extent of MO degradation and formation of other organic byproducts from MO degradation, total organic carbon (TOC-L, Shimadzu) analyzer was used to measure the concentration of organic carbon remaining in the

solution. This also allowed for a better understanding of the reaction mechanisms and MO degradation pathways.

Cyclability experiments were performed to investigate the effect of reusing the photocatalysts on their photoactivity as well as their stability in a continuous flow reactor system. Briefly, upon the completion of a photodegradation experiment, both the remaining photocatalyst in the reactor volume and deposited on microfilters were collected and dried at 60 ºC, weighed and subsequently used with the appropriate volume of contaminated MO synthetic water.

CHAPTER IV

RESULTS AND DISCUSSION

A thorough discussion concerning the successful iterative syntheses steps and their purposeful effect on varying morphology, surface defects, incorporation of carbon-based composites will be presented in this chapter. **Figure 11** summarizes particular modifications undertaken on pristine TiO_2 nanoparticles. The chemical reduction of samples was performed using $NaBH_4$ under the same scheme as will be discussed later. Growing the photoactive catalyst atop the paramagnetic core was performed via a slightly different route to that depicted in **Figure 11**. The overarching aim is to incorporate and investigate the below alterations, in order to achieve a model photoactive catalyst functional and retrievable under visible-light irradiation.

Understanding the effects each synthesis step has on the physical parameters of the TiO_2-based photocatalyst and relating those to the sample's photoactivity, a clearer picture can be put together on how to effectively optimize the material. Some physical parameters that have been investigated include, but are not limited to, crystalline phase, crystallite size, morphology, surface defects, band-gap, etc. Those parameters were controlled in subsequent syntheses steps in order to yield a better synergy between optimum physical properties (i.e. large crystallite size, predominant anatase phase, etc.) and further modification embarked upon.

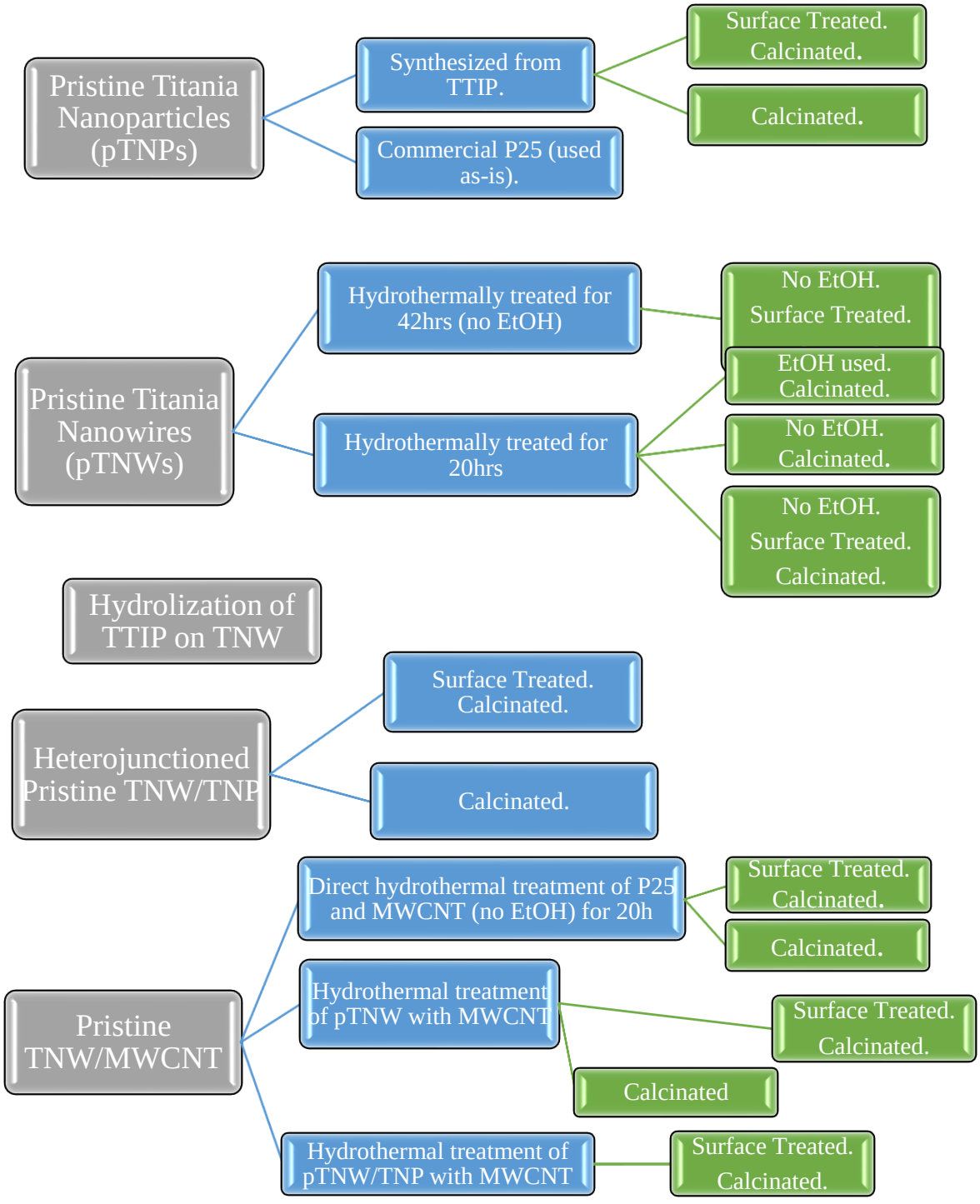

Figure 11 – General synthesis scheme of morphological, crystalline phase, heterojunctions, and carbon-based composite incorporation modifications undertaken on TiO_2

Kinetic studies were performed on samples to evaluate the rate of MO degradation and the kinetic parameters were used to compare the performance of materials fabricated in this work with other TiO_2-based photocatalysts.

Pristine Titania Nanoparticles (pTNPs)

Briefly, P25 has been widely used in commercial and laboratory syntheses for titania based material development due to its relatively basic nano-spherical zero-dimensional morphology which serves as a good starting point for higher dimensional growth. Moreover, P25 was reported to have high photoactivity, whereby rapid kinetics are observed in degrading organic contaminant azo dyes in contaminated waters. Unless otherwise specified, all synthesis for higher dimensional titania-based morphologies in this work, P25 was used as the titania precursor.

In order to evaluate effects of the different physical and photochemical parameters that are necessary for yielding a material with high photoactivity, lab synthesized pTNPs were achieved. Although their morphologies were similar to that of P25 – with a slight difference in nanoparticle average diameter – their respective photoactivities were notably different. TTIP was used as the titania precursor for the solvothermal fabrication of the pTNPs and calcination in air (600 ºC, 2 h) was carried out in a muffle furnace. Furthermore, surface treatment was performed prior to calcination on an amount of pTNPs.

The effect of calcination and surface treatment procedures were performed on all synthesis steps in this work to probe the effect they have on crystallinity, surface

structure, photoactivity, etc. As can be seen from **Figure 12** below, solar light induced photodegradation experiment on 10ppm Methylene Orange, P25 and the as prepared pTNPs from TTIP precursor shows similar and relatively high photoactivity – 62.9% and 58.7% degradation 120 minutes. The pTNPs prepared without the surface treatment procedure show a significant reduction in degradation efficiency – namely 31% degradation in 120 minutes. In order to reaffirm the understanding in the structural and crystalline effects of a material on its photoactivity, characterization techniques were performed on the photocatalysts.

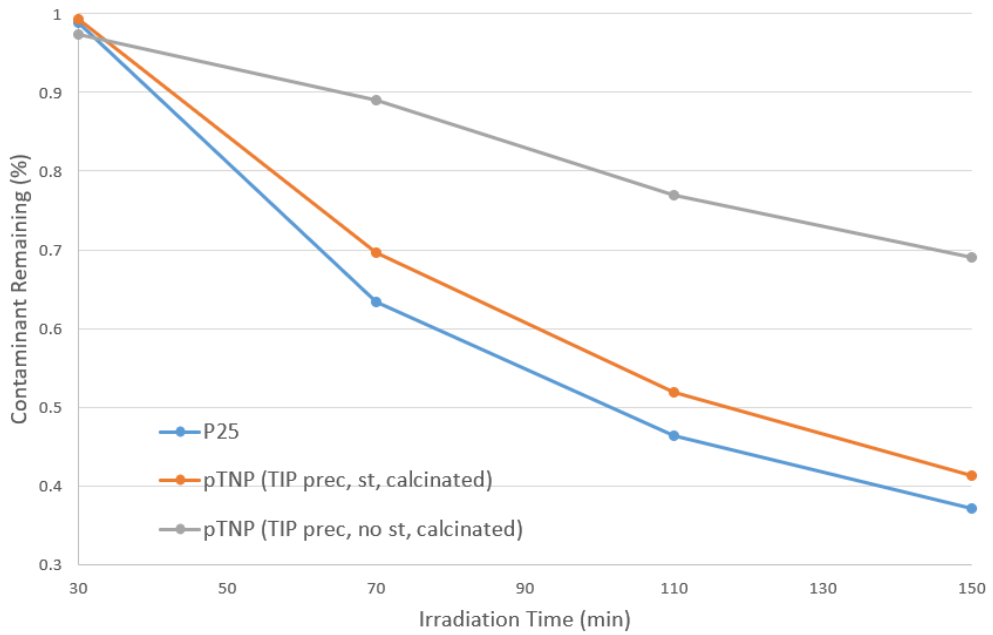

Figure 12 – Photodegradation of MO (10ppm) using commercial (i.e. P25) and synthesized pTNPs under solar irradiation

Although it is not common knowledge what titanium precursor is used and whether surface treatment is performed on commercial P25, it has been previously reported that the effect of titanium precursor affects the final photoactivity of the

material. As discussed previously, anatase is the predominantly photoactive titania phase. XRD analyses has been performed on the synthesized photocatalysts and the data are displayed in **Figure 13a**. It can be seen that the surface treatment procedure performed on the TTIP precursor pTNPs, prior to calcination, leads to a full anatase phase sample – even higher than the predominant but not full anatase P25. Pristine TNPs diffractogram - prepared with surface treatment – shows purely anatase diffraction peaks at 2θ values of 25.3º, 37.8º, 48.2º and 55.3º, which are assigned to the crystallography planes of {101}, {004}, {200}, and {211} - JCPDS card No. 21–1272. Interestingly, the pTNPs calcinated without surface treatment show a near complete rutile phase (98% rutile) owing to distinctive diffraction peaks namely at 2θ values of 27.4º, 36.1º, and 41.3º - JCPDS card No. 21–1276. Nonetheless, P25 witnesses slightly higher photoactivity although the crystalline phases were found to be 90.8% anatase and 9.2% rutile. This is a clear first indication that although a predominantly rutile phase is unfavorable for high photoactivity, a full anatase phase is not necessarily the sole factor in governing the degree of photoactivity of a material. **Figure 13b** summarizes the average crystallite size (D) findings approximated using Scherrer equation ($D = (0.9)\lambda/W \cos(\theta)$(B. Ingham, 2014) λ is the X-ray wavelength used during XRD analysis (Cu-Kα = 0.15405 nm), W is the full-width at half angle intensity of the peak (Rad) calculated using Origin software, and θ is the Bragg's angle. Scherrer formula is utilized to approximate the average size in the vertical direction of crystals.

Generally, it is more favorable for a photocatalyst to have larger crystallite sizes. The larger crystallites allow in reducing the disadvantageous electron-hole

recombination rate upon photoexcitation, which is an innate property of pristine unmodified titania. Larger crystallites simply increase the migration distance of a photoexcited electron to reach the surface of its parent titania crystal. This in turn increases the probability that the photogenerated electron can partake in a useful redox reaction on the titania surface – effectively enhancing the observed photoactivity of the material in degrading organic contaminants. However, given that P25 exhibits higher photoactivity yet a smaller average crystallite size, it can be deduced that perhaps when the difference in crystallite size is not very significant, its effect on photoactivity is minimized. Moreover, there are truly multiple factors that may affect the photoactivity of a material like titania. Parameters such as predominant crystalline phase and crystallite size have perhaps a varying degree of importance on the photoactivity. It is the agglomeration of these parameters that truly define the photoactivity of a material. Given a sample with high photoactivity, its characterized parameters will inevitably shed light on the varying degree of importance they have on photoactivity. It is the anticipation of this work that once a bigger collection of synthesized materials with different synthesis and surface treatment conditions are characterized and their photodegradation performance evaluated, a pattern will emerge that will explain the relationship between the materials' physical characteristics and their performance.

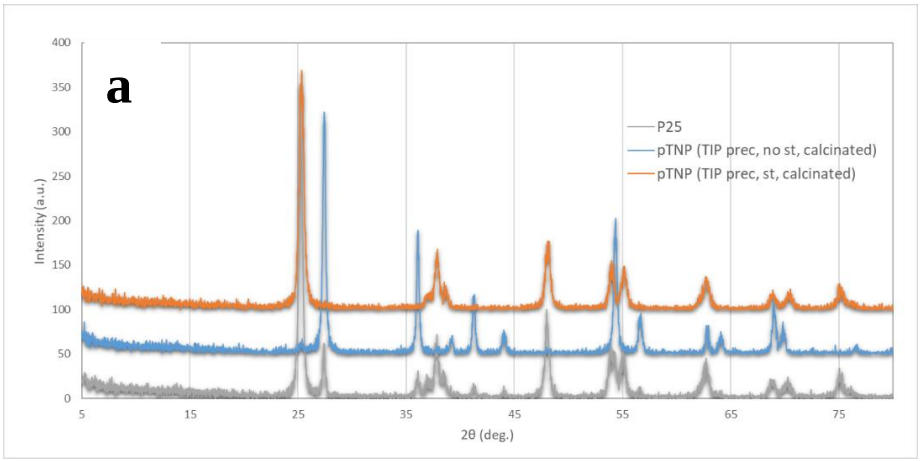

b

Sample	Phase (%)		Avg. Crystallite Size (D) (nm) - Sherrer Equation
	Anatase	Rutile	
P25	90.8	9.2	17.19
pTNP (TIP, no st, 600C calc)	2	98	24.9
pTNP (TIP, st and 600C calc)	100	---	20.6

Figure 13 – a) XRD patterns of commercial P25 and synthesized pTNPs and b) Average Crystallite Size of P25 and pTNPs approximated using Scherrer equation

Another significant parameter in the photoactivity of photocatalytic nano-spherical particles is their surface area. Smaller diameters translate to a favorable larger surface area. As can be seen from TEM images of P25 and pTNP (TTIP prec, st, calcinated) in **Figure 14** below, P25 generally has slightly smaller nanoparticles. This may reduce aggregation in aqueous media, effectively maintaining a higher available surface area. Nanoparticles will spontaneously aggregate to reduce their surface tension and the degree of aggregation can be verified using Zeta potentials. A positive, or negative, Zeta potential with absolute values greater than 30 mV indicates stable colloids due to electrostatic repulsion between nanoparticles.

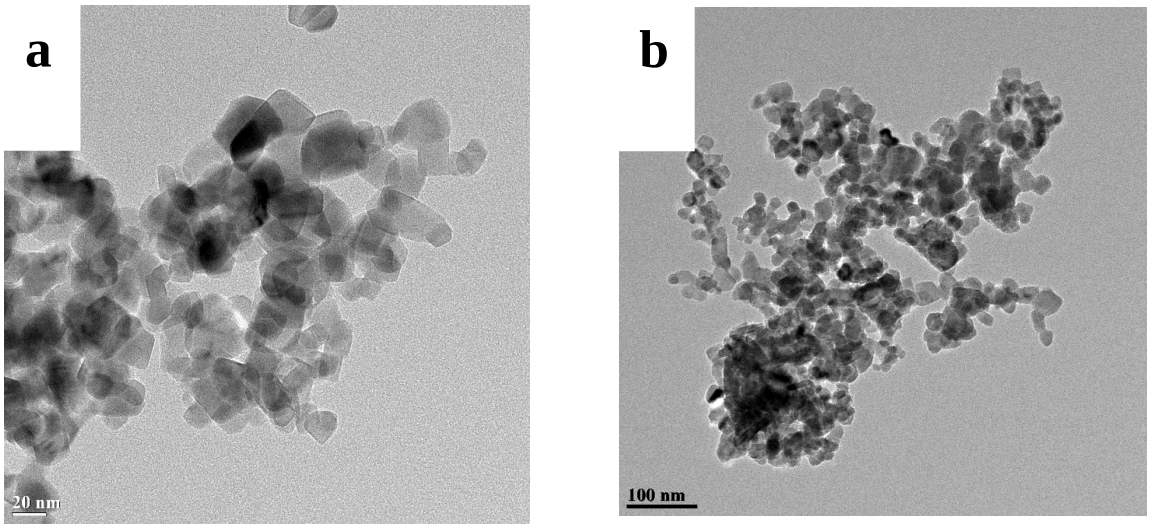

Figure 14 – TEM images of a) P25 and b) pTNP (TTIP prec, st, calcinated)

It is also worth noting that the titanium precursor used in the synthesis of both P25 and pTNPs (using TTIP as precursor) are perhaps different. The use of different titanium precursor in the synthesis of titania has been studied previously and it was found that given the same synthesis procedure using different initial titanium precursors, the final product can vary slightly in crystallinity, size and crystal phase yielding a slightly different photoactivity.

Pristine Titania Nanowires (pTNWs)

Shifting from a 0-D to a 1-D nanostructure acts to a significant degree for enhancing the photoactivity of a material. Generally, a unidimensional, crystalline, anatase titania nanowire can further reduce the effect of the ever-imposing predicament of high electron-hole recombination rate present in titania. Upon photoexcitation, the electron will have a directional path of migration along the directional axis of the nanowire. To

this extent, an alkaline hydrothermal method was utilized to synthesize the pTNWs whilst employing P25 as the titania precursor for the nanowire growth. The effect of ethanol as part of the hydrothermal growth medium was examined, along with the effects of surface treatment prior to calcination, and the samples' physical characteristics and corresponding photoactivity in degrading Methylene Orange as a model organic contaminant were investigated. Moreover, the hydrothermal treatment time was varied from 20 to 42 hours, whereby the latter should theoretically yield longer nanowires. In short, the nanowire growth mechanism is facilitated under the high temperature and pressure during the hydrothermal synthesis. Titania nanoparticles effectively grow from the top down and organize in such a mechanism where a final 1-D morphology is produced. The diameter and length have been proposed to be largely governed by the hydrothermal synthesis' temperature. Generally, temperatures above 160 ◦C yield nanowires, whilst temperatures below that reduce the growth kinetics – given the same time of synthesis – and only form thicker nanorods.

Ethanol (EtOH) serves as a templating agent during the nanowire hydrothermal process. However, as can be seen in **Figure 15** below, the effect of ethanol is quite significant on reducing the photoactivity on the final pTNW samples fabricated using an EtOH assisted scheme. Moreover, it can be clearly seen that samples that were not surface treated and particularly calcinated have had a notable cutback in their photodegradation efficiency. Although samples fabricated under longer nanowire growth times yielded slightly more favorable photodegradation of the MO, the effect of growth time is significantly reduced when surface treatment and calcination are introduced as

part of the synthesis procedure. Therefore, for later syntheses in this work, ethanol was not used as a templating agent during nanowire growth, the nanowire growth time has been maintained at 20 hours, and surface treatment and calcination were performed in all later samples discussed in later subsections.

A significant morpholofical difference is noticed when ethanol has been used as a templating agent during the alkaline hydrothermal nanowire growth procedure to yield pTNWs. As can be observed from **Figure 16** below, the use of ethanol allows for longer and more wire-like woven nano-structures that appear more amorphous than crystalline (**Figure 13 a**). Although the SEM image in **Figure 16 b** is for pTNW (20hrs, no EtOH, st, calcinated) and **Figure 16 a** is for pTNW (20hrs, with EtOH, no st, no calcination), the morphology of the two samples cannot be goverened by surface treatment or calcination since both are post-morphological change procedures and have very little to no effect on morphology. They do however have effects on crystallinity was later discussed.

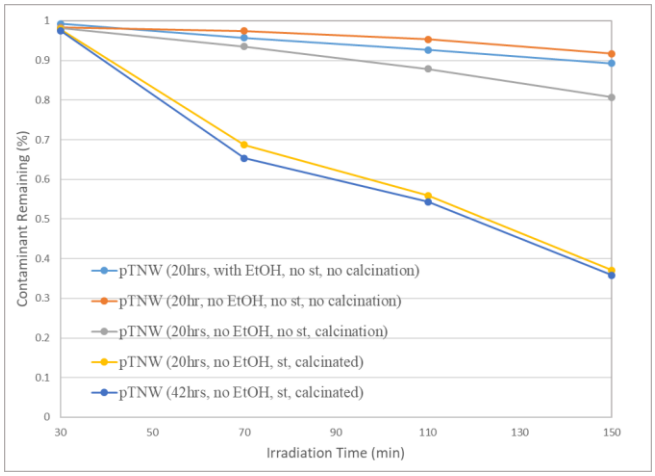

Figure 15 – Photodegradation of MO (10ppm) under solar irradiation using different pTNWs fabricated under different conditions

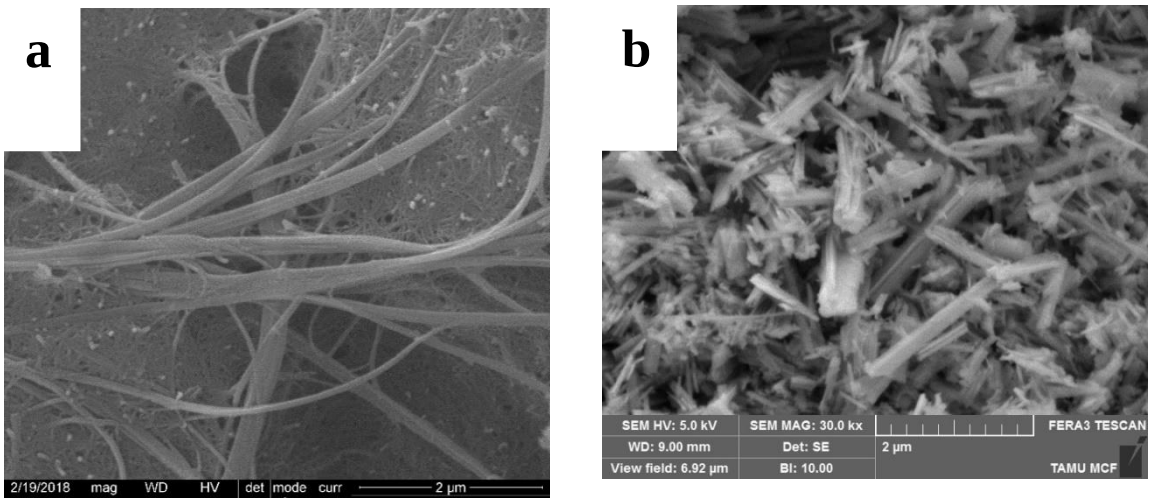

Figure 16 – SEM images of a) pTNW (20hrs, with EtOH, no st, no calcination) and b) pTNW (20hrs, no EtOH, st, calcination)

The significant degradation enhancement of the sample in **Figure 16 b** (64.2% degradation of MO in 2hrs under solar irradiation) compared to the pTNW sample fabricated with EtOH assistance (10.7% degradation under the same conditions), cannot simply be attributed to the morphology effect, albite an important effect. **Figure 15** shows that generally samples synthesized via an ethanol-assisted procedure show a significant reduction in photodegradation efficiency compared to samples synthesized without ethanol during the nanowire growth procedure. To better understand the degree of importance ethanol has on photoactivity compared to surface treatment and calcination, XRD analysis was performed on samples to probe their crystallinity, or lack thereof. **Figure 17 a** shows that the sample synthesized with ethanol as a templating agent during nanowire growth showed no presence of anatase titania, which is the most photoactive titania phase. Moreover, Scherrer approximations in **Figure 17 b** of the

same material showed the smallest crystallite size of 9.34 nm among all pTNW samples prepared. The small crystallite size coupled with the nonexistent anatase phase act as guiding points in explaining why this material had a very low observed photodegradation efficiency in degrading MO. On the contrary, the pTNW samples grown without facilitating EtOH in the hydrothermal medium showed a larger crystallite size, approximately 18.5 nm, and a more predominant anatase phase.

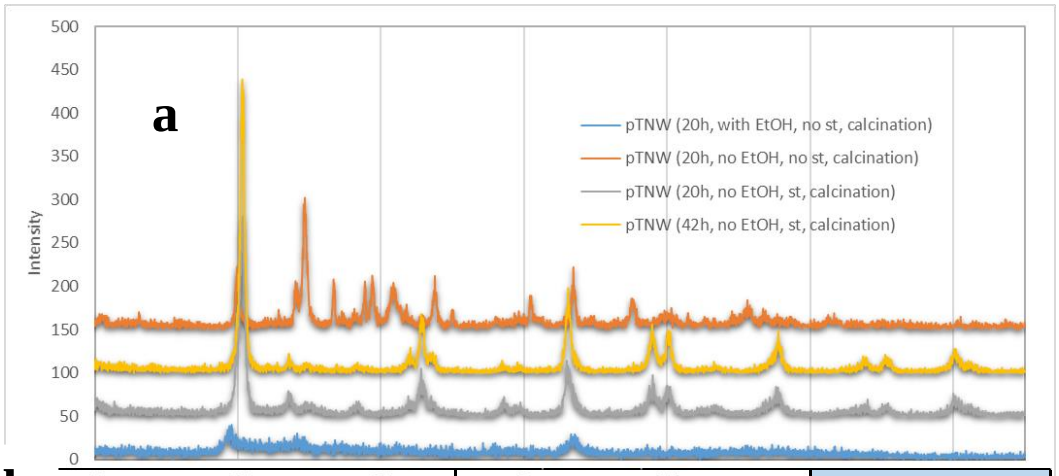

b

Sample	Phase (%)			Avg. Crystallite Size (D) (nm) - Sherrer Equation
	Anatase	Rutile	Titanium Dioxide	
pTNW (20h, with EtOH, no st, calcination)	---	2.5	97.5	9.34
pTNW (20h, no EtOH, no st, calcination)	49.1	---	50.9	18.32
pTNW (20h, no EtOH, st, calcination)	87.1	12.9	---	18.57
pTNW (42h, no EtOH, st, calcination)	100	---	---	19.68

Figure 17- a) XRD patterns of pTNWs synthesized with varying use of EtOH, surface treatment, and calcination, and b) Crystallite Sizes of pTNWs approximated using Scherrer equation

It is apparent that the surface treatment procedure alone served to enhance the phase shift to a more favorable anatase phase, subsequently improving photoactivity. A remarkable 38% phase increase from rutile to anatase is observed between the two pTNW samples synthesized and calcinated under the same procedure, with the only

difference lying in the surface treatment step. This consequently led to a photodegradation increase from 19.2% to 62.9% - the latter corresponding to the surface treated sample. TEM images in **Figure 18 a-b** below shows that the lattice fringe spacing found on the pTNW surface treated samples does in fact correspond to anatase titania – owing to a notable lattice spacing of 0.347 nm. Lattice fringe spacing in **Figure 18 c** corresponds to an amorphous titania phase, having an apparent spacing of 0.248 nm. Thus, it was found that the same surface treatment procedure, irrespective of morphology, has almost the same remarkable effect at dramatically increasing the anatase phase composition of the photoactive sample. However, to confirm this finding, in later subsections where MWCNTs are introduced to the nanomaterial, surface treatment studies were also performed to aid in better understanding their effect on crystallinity, and subsequently on the photoactivity of the sample. Surface treatment was not performed on samples with ethanol being an integral part of the hydrothermal synthesis seeing as that ethanol-assisted samples have no anatase phase whatsoever to be improved by the surface treatment procedure.

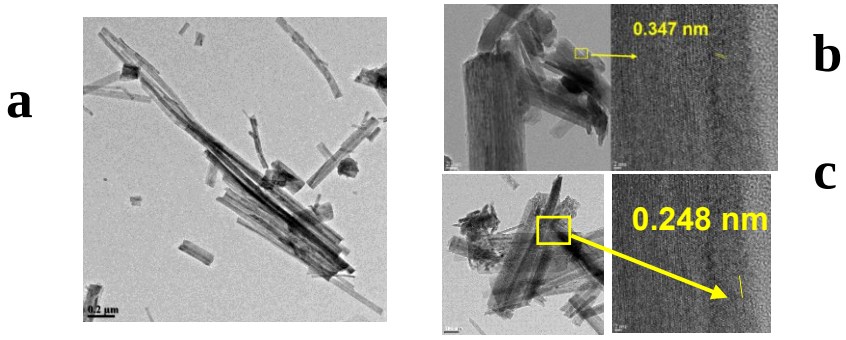

Figure 18- a) TEM image of pTNW (20h, no EtOH, st, calcination) and HRTEM and lattice fringe spacing of b) pTNW (20h, no EtOH, st, calcination) and c) pTNW (20h, no EtOH, no st, calcination)

All the slightly altered properties resulting upon nanowire formation from nanoparticles hydrothermally facilitated growth have shown to inevitably yield slightly higher photoactivity of pTNW compared to pTNP. In order to effectively determine whether the increased photoactivity is solely attributed to the hypothesized reduction of electron-hole recombination rate due to the pTNW's intrinsic 1-D morphology compared to pTNPs' 0-D morphology, diffuse reflectance spectroscopy (DRS) using a solid-state UV-Vis-NIR spectrophotometer was employed to examine whether a change was exhibited in band-gap energy between both morphologies.

In brief, the band-gap energy is a set energy level intrinsic to a photocatalyst whereby it is the required minimum energy, measured in eV, needed to photoexcite an electron from its ground state valence band (VB) to a conduction band (CB). The excited electron can travel along the crystal to the crystal's surface upon successfully being photoexcited from the VB to the CB. Photoactivity is largely determined by whether intermediate energy levels exist in the band-gap. In the case that some may do in fact exist, the apparent band-gap energy will be reduced, and a higher frequency of solar spectra photons will have sufficient energy to photoexcite available valence band electrons. Customarily, a minute fraction of electrons and holes that are photogenerated will partake in a successful photodegradation reaction, while the rest will result in an unfavorable quick recombination scheme – the electron travels back and fills the hole it generated during photoexcitation.

Factoring for the direct transition type semiconductor nature (optical property of titania), optical bandgap energies were approximated using Tauc's equation below (A.S. Hassaniena, 2016):

$$(\alpha h\nu)^{\frac{1}{2}} = A(h\nu - E_g)$$

where α is the absorption coefficient, h is Planck's constant, E_g is the optical bandgap of the semiconductor, ν is the frequency of incident photons. α is essentially 2.303/Ad, where A is the absorbance of the sample and d is the cell path length used. Solid-state UV-Vis-NIR and the corresponding bandgap approximation plot using Tauc's equation are seen in **Figure 19**. The comparison between the synthesized pTNP and pTNW samples show that nanowire morphologies have a substantial reduced bandgap energy. This is particularly interesting when considering that the pTNWs were fabricated using P25 as precursor instead of the TTIP used in fabricating the pTNPs. P25 has a bandgap energy of about 3.2 eV, compared with pTNWs having bandgaps of 2.95 eV and 2.9 eV for surface un-treated and surface treated samples, respectively. pTNPs fabricated have an estimated bandgap of 3.0 eV.

The reduced bandgap of pTNWs could be attributed to the roughening of surface edges as can be seen in **Figure 19 a**, or more likely due to the formation of some surface oxygen vacancies during calcination. Furthermore, since bandgap is apparently reduced by surface treatment prior to calcination, the increase of oxygen vacancies could in part be attributed to residual sulfate and chloride ions attached to the surface prior to calcination. The presence of oxygen vacancies was examined using X-ray Photoemission Spectroscopy (XPS) in **Figure 20** below.

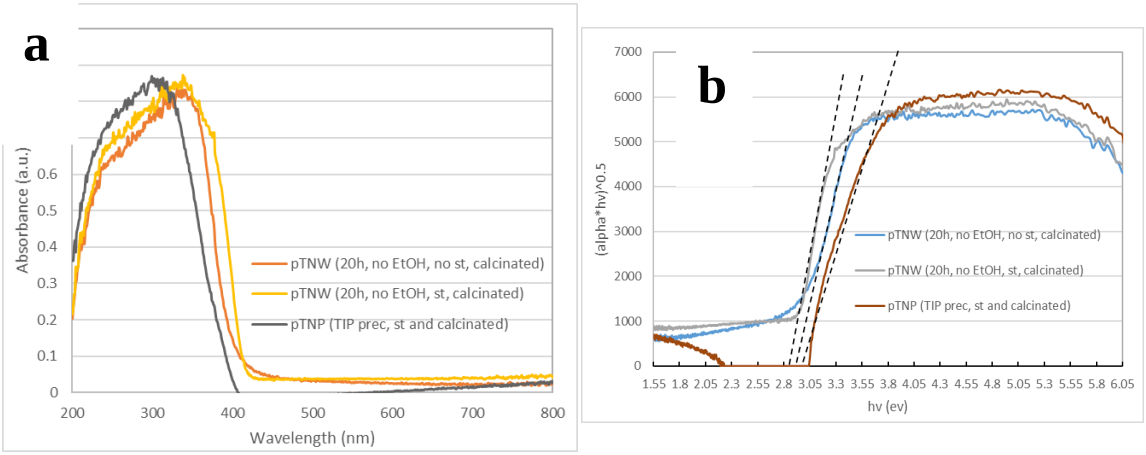

Figure 19 – a) Solid-state UV-Vis-NIR spectra and b) Tauc plots for bandgap energy approximations of pTNPs and pTNWs

The oxidation state and surface composition of the prepared pTNPs and pTNWs – both surface treated and calcinated – has been investigated using XPS in **Figure 20** below. The full spectra range XPS survey in **Figure 20 a** indicate the presence of titanium and oxygen as sole elements as expected. Briefly, the full survey was carried out under 80 eV passing energy and the element specific survey was carried out at high resolution (20 eV passing energy). The notable down-shift of the pTNW sample is interesting given that no measure was taken to purposefully affect the surface chemistry, however as mentioned the reduction in bandgap energy of pTNWs is most probably attributed to the introduction of oxygen vacancies during synthesis. **Figure 20 b** represents three distinct Ti2p peaks at 459.6 eV, 465.2 eV, and 473.1 eV corresponding to Ti $2p_{3/2}$, Ti $2p_{1/2}$, and Ti $2p_{3/2}$ – belonging to the pTNP sample. The same figure shows a clear shift in peak locations for the pTNW sample, namely at 456.1 eV, 461.7 eV, and 469.4 eV corresponding to Ti $2p_{3/2}$, Ti $2p_{1/2}$, and Ti $2p_{3/2}$. The peak shift is perhaps due to the introduction of oxygen vacancies during the synthesis procedure of the nanowires.

The highly alkaline hydrothermal medium, followed by the relatively acidic surface treatment procedure prior to calcination can result in the formation of oxygen vacancies in the titania surface without a purposeful reduction scheme. Moreover, the reduction in peak intensity of the pTNW sample could be attributed to the formation of Ti^{3+} which cause a slight reduction in intensity of Ti^{4+} recorded in the XPS survey of Ti2p. The observed reduction in bandgap energy mentioned previously can be attributed to the apparent presence and formation of oxygen vacancies in the pTNWs structure. Although there was no apparent change in color between pTNPs and pTNWs, this is easily explained by the lack of a disordered surface in both samples. It is the presence of a disordered surface that allows for a color change to be observed – normally a darker color. As will be discussed and observed with reduced (black) photocatalytic materials prepared later, the disordered structure usually tends to form upon intentional reduction of the sample.

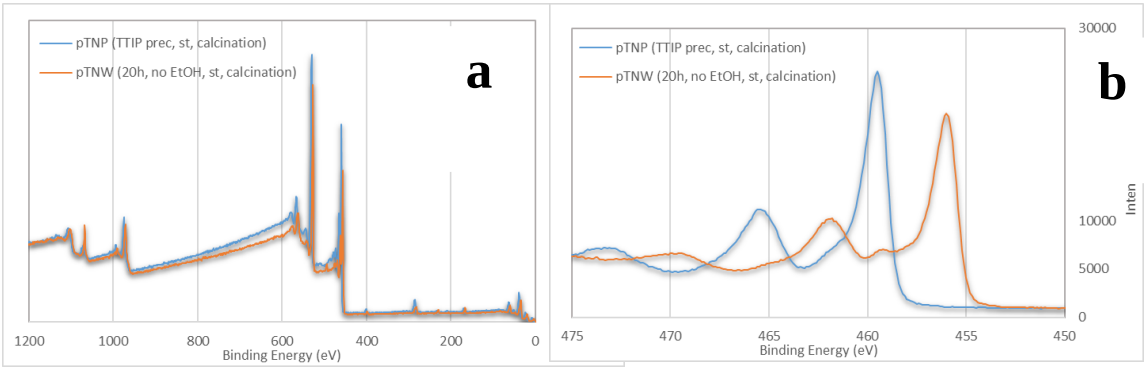

Figure 20 – a) Full-scale XPS survey and b) Ti2p survey of pTNP (TTIP prec, st, calcination) and pTNW (20h, no EtOH, st, calcination)

Heterojunction Pristine Titania Nanowires (pTNWs)/ Pristine Titania Nanoparticles (pTNPs)

As was previously discussed, in order to effectively enhance the quantum efficiency or the photodegradation efficiency of a titania nanostructure, several factors need to be considered simultaneously. There's an apparent dependence of the innately high electron-hole recombination rate of titania on nano-morphology (i.e. 0-D nanospheres and 1-D nanowires), crystallite size, oxidation state (i.e. Ti^{4+} and Ti^{3+}), crystal phase (i.e. anatase), and specific exposed facets (i.e. {101}, {100}, etc.). Generally, there's a tradeoff between having a predominant 0-Dimentional structure compared to a 1-Dimentional structure. Briefly, a 0-D structure such as nanospheres have an advantageously high energy density, higher surface area, and less structural hinderances to agglomerate assuming an absolute Zeta potential above 30 eV. A 1-D structure such as nanowires are utilized for having a higher surface area for target contaminant adsorption (an elementary step in any photocatalytic reaction), reduced electron-hole recombination rate due to axial travel of photogenerated electron along the surface structure of the NW, and higher accessibility to intertwine with dopants if design deems fit.

Anatase titania has a higher surface activity compared to rutile because it has more defect states in its structure – necessary to produce more oxygen vacancies along its lattice structure. Moreover, having a predominant {101} exposed anatase facet would be beneficial because this particular facet yields the lowest surface energy (0.44 J/cm^2). A heterojunction nanostructure of nanoparticles garnishing nanowires which is

predominantly anatase and has {101} exposed facets was fabricated in order to compare its photoactivity to pTNPs and pTNWs. The nano-heterojunction structure would perhaps yield higher photoactivity when later combined with MWCNTs and then reduced.

In summary, as prepared pTNWs that were not surface treated but were calcinated were added to an amount of IPA and dissolved EDTA. An equimolar amount of TTIP to pTNWs was added to the solution under vigorous stirring for 15 minutes. The aqueous medium was then transferred to a Teflon-line stainless steel autoclave and maintained at 150 ºC for 24 hours. This ensured the hydrolyzation of the TTIP to pTNPs atop the pTNWs structure – whilst the pTNWs structure remained morphologically unchanged. The resultant pulp was washed several times, vacuum dried, fully surface treated and finally calcinated in air. The final product was an equimolar amount of pTNPs/pTNWs heterojunction.

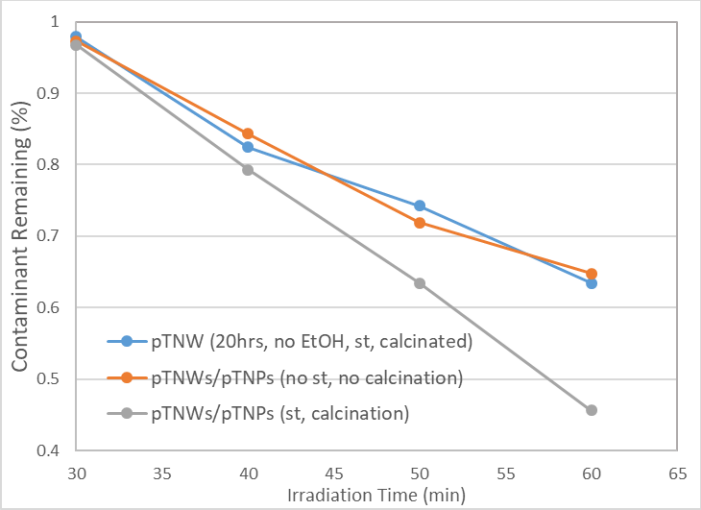

Figure 21 – Comparative photodegradation of MO (10ppm) under solar irradiation using pTNWs and pTNWs/pTNPs heterojunctions

As can be observed from **Figure 21** above, the surface treated and calcinated pTNWs/pTNPs is superior to pTNWs. The photodegradation experiments displayed on the figure were performed for irradiation time of 30 minutes, whereby 30 minutes of dark adsorption conditions were allowed prior to solar irradiation. pTNWs achieved 36.7% degradation, whilst surface treated and calcinated pTNWs/pTNPs showed enhanced degradation, 54.4%, in only 30 minutes of solar irradiation. This increase in performance of the heterojunction structure can be explained by the enhanced crystallinities, morphologies and crystallite sized of the synthesized pTNWs/pTNPs samples. It is also worth noting that the heterojunction structure that wasn't surface treated exhibited a 22% decrease in photodegradation performance compared to the surface treated sample.

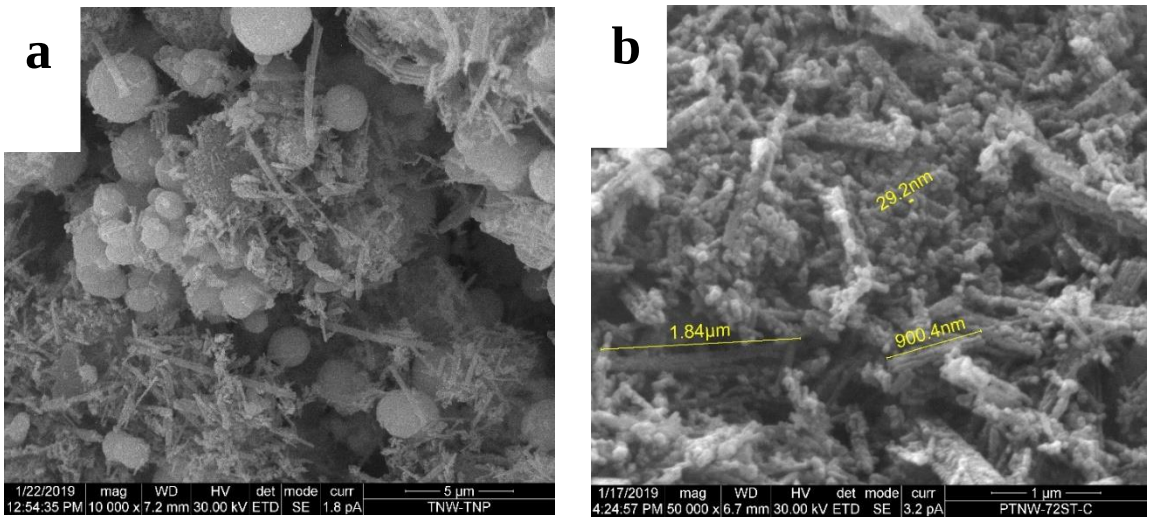

Figure 22 – SEM images of a) pTNW/pTNP (no st, calcination) and b) pTNW/pTNP (st, calcination)

a

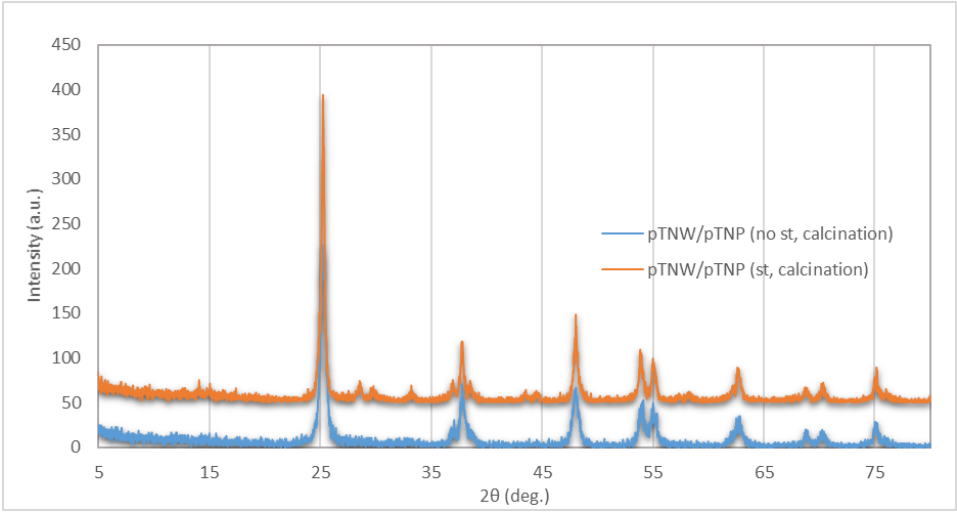

b

Sample	Phase (%)		Avg. Crystallite Size (D) (nm) - Sherrer Equation
	Anatase	Rutile	
pTNW/pTNP (no st, calcination)	100	--	15.58
pTNW/pTNP (st, calcination)	100	--	21.57

Figure 23- a) XRD patterns of pTNW/pTNPs synthesized with and without surface treatment, and b) Crystallite Sizes of pTNW/pTNPs approximated using Scherrer equation

As can be seen from Figure 23, the untreated sample's morphology exhibits both morphologies, however on different scales – namely nano and micro scale. It is worth noting that although some nanowires have been decorated with nanoparticles, a great fraction of nano/microparticles are seemingly stand-alone structures without a heterojunction. It is therefore safe to deduce that the acidic surface treatment process prior to calcination leads to effective encapsulation of heterojunctions between the nanoparticles and nanowires in a very thorough fashion, as can be seen in **Figure 22 b**. In order to probe the effect on crystallinity of both procedures, XRD characterization was performed and the data are presented in **Figure 23 a**.

Remarkably, both treated and untreated samples possess a full anatase structure as can be observed from **Figure 23 a**. However, it is seen that anatase peaks at 2θ values

of 25.3º and 48.2º, which are assigned to the crystallography planes of {101} and {200} respectively - JCPDS card No. 21–1272 – show a clear reduced peak intensity for the untreated sample. This can explain why photoactivity of the treated sample is about 20% higher than that of the untreated one. A higher ratio of exposed {101} facet in the surface treated sample which has the lowest surface energy of any anatase facet translates to lower photon energy required for photoexcitation, effectively increasing the probability of a successful photoreaction. Perhaps more interestingly, however, is the clear increase in average crystallite size – approximated using Scherrer equation in **Figure 23 b,** which contributes to the effective increase in photoactivity of the surface treated sample. An evident 38.4% increase in average crystallite size is witnessed for the treated sample compared to that of the untreated sample. Again, this indicates that the surface treatment procedure does in fact have an effect on morphology and crystallite structure since it is performed prior to calcination, whereby the sample yields its final structure. A larger crystallite size translates to lengthier path of migration by a photogenerated electron to the surface during the initiation of a photoreaction. This in effect reduces the probability, and subsequently the rate, of electron-hole recombination, and thus enhances the chances of a successful photodegradation reaction to occur.

Comparing solid-state absorption spectra for pTNWs and the heterojunction pTNWs/pTNPs, it can be observed that the surface treated heterojunctioned structure has a bandgap edge that is slightly lower that of the pTNWs as shown in **Figure 24 a**. Bandgap approximations using Tauc equation in **Figure 24 b** shows that in fact the surface treated heterojunction pTNWs/pTNPs have a smaller bandgap energy of 2.62

eV, approximately 0.2 eV less than that of the untreated sample, and about 0.28 eV lower than that of the base pTNWs. Interestingly, given that stand-alone surface treated NPs and NWs have bandgap energies of 3 eV and 2.9 eV, the reduction found in pTNWs/pTNPs bandgap can be attributed to both oxygen vacancies from the nanowires and the heterojunction structure itself.

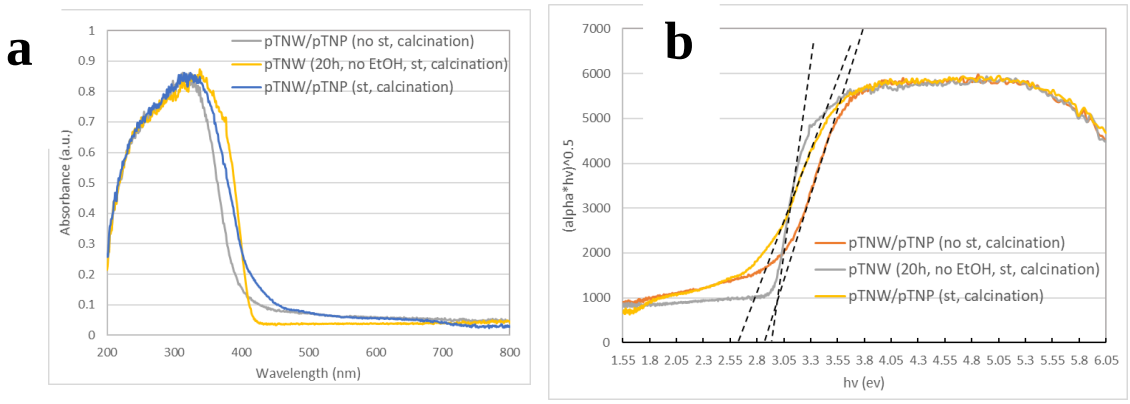

Figure 24 – a) Solid-state UV-Vis-NIR spectra and b) Tauc plots for bandgap energy approximations of pTNWs/pTNPs

Given that from both pTNPs and pTNWs it was found that {101} exposed anatase facets exist, it could be surmised that both nanostructures' lattices can mix at their respective interfaces, thus resulting in significant interactions and allowing surface heterojunctions to form. The smaller sized nanoparticles can in turn promote delocalization of molecular orbitals around the CB edge of the nanostructure creating bandgap traps between the VB and CB and in effect reducing the effective bandgap energy of the heterostructure.

In summary, it can be seen that the photodegradation efficiency of the pristine titania samples discussed thus far show that the pTNWs/pTNPs heterostructure is superior, followed by pTNWs and pTNPs respectively. The differences in photoactivity have been dominantly attributed to the ratio of anatase phase, exposed anatase {101} facets, structural effects on reducing the electron-hole recombination rate, and the presence of synthesis induced oxygen vacancies such as in pTNWs.

Pristine Titania Nanowires - Multiwalled Carbon Nanotubes Composites (pTNWs/MWCNTs)

The effect of carbon-based materials (i.e. graphene, CNTs, activated carbon, etc.) heterojunction with titania, predominantly focusing on 0-Dimensional pTNPs, was investigated. The main focus of previous studies has been on finding different synthesis schemes for the effective surface binding of the carbon species to the photoactive titania. Owing to the rapid electron-hole recombination rate, low adsorptive capacity, small surface area, wide bandgap energy, and subsequent poor visible-light energy utilization, various methods have been proposed to curb the disadvantageous effects of the aforementioned. Carbon-based materials and in particular CNTs (Multiwalled CNTs used for this work), have remarkable properties that make them a great candidate to incorporate with titania nanocomposite.

MWCNTs have a high thermal and chemical stability, which are of paramount importance during nanocomposite synthesis when the MWCNTs are to be subjected to high chemical and thermal oxidative processes (i.e. hydrothermal, calcination, etc.). Due

to their high surface area, a well-integrated mesh of MWCNTs with pTNWs can yield an improved adsorptive capacity and effectively more sites for adsorbing contaminants onto the 3-Dimensional pTNWs/MWCNTs nanocomposite. Importantly, a surface heterojunction of CNTs with a pTNWs can effectively increase defect surface sites on the photoactive titania due to the creation of Ti-C and Ti-O-C surface bonds. This in effect means that an improvement in visible-light utilization is achieved. One major predicament facing previous works performed with pTNPs and CNTs (or other carbon allotropes) is the nanoparticles' tendency to severely agglomerate during the fabrication process. This problem is curbed by employing 1-Dimensional pTNWs which have a lower tendency to agglomerate under the binding procedure of titania and CNTs.

In order to test synthesis effects on the resultant pTNWs/MWCNTs, several alternatives have been evaluated. Firstly, a sample dubbed pTNWs/MWCNTs (1) was synthesized using a typical alkaline hydrothermal process. P25 was used as the titania nanowire precursor and an amount of 5 w% MWCNTs was well mixed in the alkaline medium prior to hydrothermal treatment. The resultant pulp for this sample was not surface treated prior to calcination. Moreover, due to a high air calcination temperature resulting in the combustion of the MWCNTs to carbon dioxide, a calcination temperature of 450 ºC for 4 hours was utilized for all MWCNTs intertwined samples. A sample undergoing the same procedure, however with the extra step of full surface treatment prior to calcination was fabricated and dubbed pTNWs/MWCNTs (2). Moreover, surface untreated and treated samples were also synthesized under the same conditions, however with utilizing as-prepared pTNWs (not surface treated but

calcinated) as the titania nanowire precursor – resulting in pTNWs/MWCNTs (3) and pTNWs/MWCNTs (4), respectively. Heterojunction of pTNWs/pTNPs/MWCNTs were also fabricated and dubbed pTNW/pTNP/MWCNTs (5). Lastly, in order to test the resulting photodegradation change if a different carbon allotrope was used, the same weight amount of grinded activated carbon (AC) was mixed with commercial P25 prior to hydrothermal treatment to form the nanocomposite. This sample was fully surface treated and calcinated, dubbed pTNWs/AC.

Due to the apparent rapid kinetics of most of the prepared pTNWs/MWCNTs nanocomposites, the photodegradation experiments were allowed to stir for 30 minutes dark adsorption conditions prior to 30 minutes solar illumination. The results are presented in **Figure 25** below.

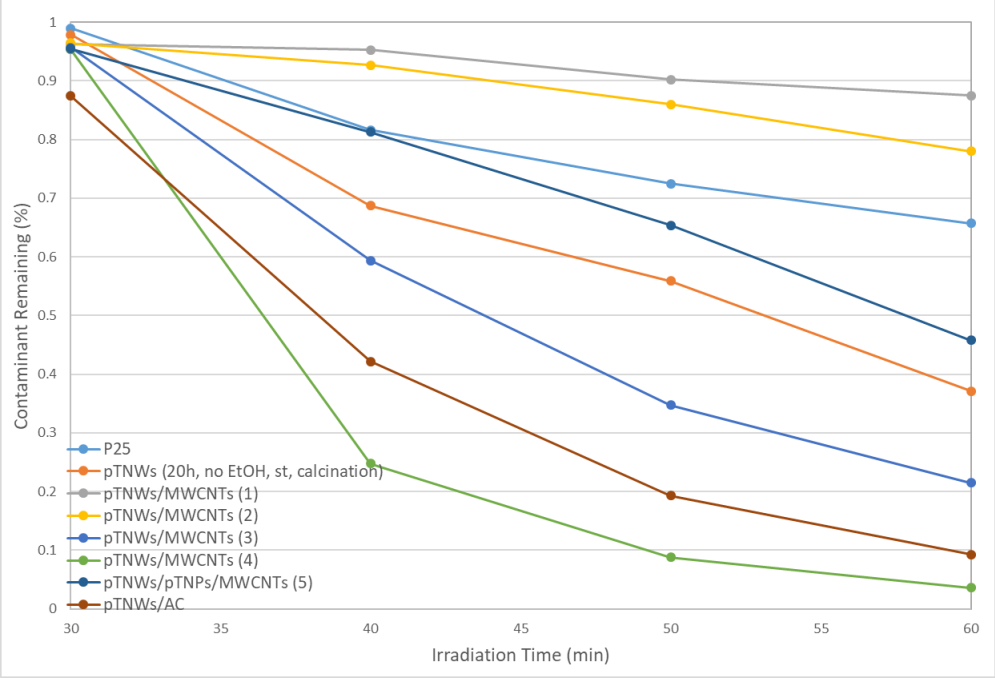

Figure 25 – Comparative photodegradation of MO (10ppm) under solar irradiation using heterojunctioned pTNWs/MWCNTs nanocomposites

Interestingly, it seems that the photodegradation performance of pTNWs/MWCNTs (1) and (2) was substantially lower than that of both its titania precursor, P25, and pTNW structures. The first two synthesis iterations yield a photodegradation efficiency of 12.5% and 22.3% after 30 minutes of solar irradiation. Moreover, pTNWs/pTNPs/MWCNTs (5) showed an unexpected lower photodegradation rate than that of the pure single titania morphology structure of pTNWs/MWCNTs (3) and (4). It does, however, have an apparent higher degradation performance (45.8%) on MO than P25 (34.27%). Surprisingly, a dramatic improvement in photoactivity is witnessed for nanocomposite samples (3), (4), and the AC heterojunctioned sample. pTNWs/MWCNTs (3) yielded a degradation efficiency of 78.5%, pTNWs/MWCNTs (4) yielded a remarkable 96.4%, and lastly pTNWs/AC resulted in a 90.7% degradation efficiency.

Some patterns do emerge from the above results shown in **Figure 25**, indicating that the surface treatment procedure is fundamental for improving the photodegradation efficiency of samples prepared under the same synthesis route. Moreover, nanocomposites prepared using P25 as a precursor showed a dramatic decrease in photoactivity, even lower than the parent P25 used. Moreover, all samples having MWCNTs showed an improved initial adsorptive capacity, whilst the pTNWs/AC sample showed the greatest initial adsorption. This is most likely due to AC's very high internal surface area (~ 1500 m^2/g). Moreover, what is hypothesized from the above findings is that properly heterojunctioned pTNWs/MWCNTs have a higher adsorption kinetics – an elementary step in any photochemical reaction. Although AC has higher

surface area than MWCNTs, the higher photoactivity witnessed for pTNWs/MWCNTs (4) compared with its AC counterpart is most likely due to better intertwinement and surface coverage of the titania nanowires along the 1-Dimensional ribbon-like structure of the MWCNTs.

Figure 26 shows representative SEM images of pTNWs/MWCNTs (2) and pTNWs/AC. As can be seen, since both of these samples had the same titania precursor, namely P25, prior to NW growth and the same surface treatment and calcination procedures, a comparison of both was insightful. The morphological comparison examines how both samples underwent the same synthesis, with the sole difference in carbon allotrope additive used, whilst yielding varying photodegradations; 22.3% for pTNWs/MWCNTs (2) and 90.7% for pTNWs/AC.

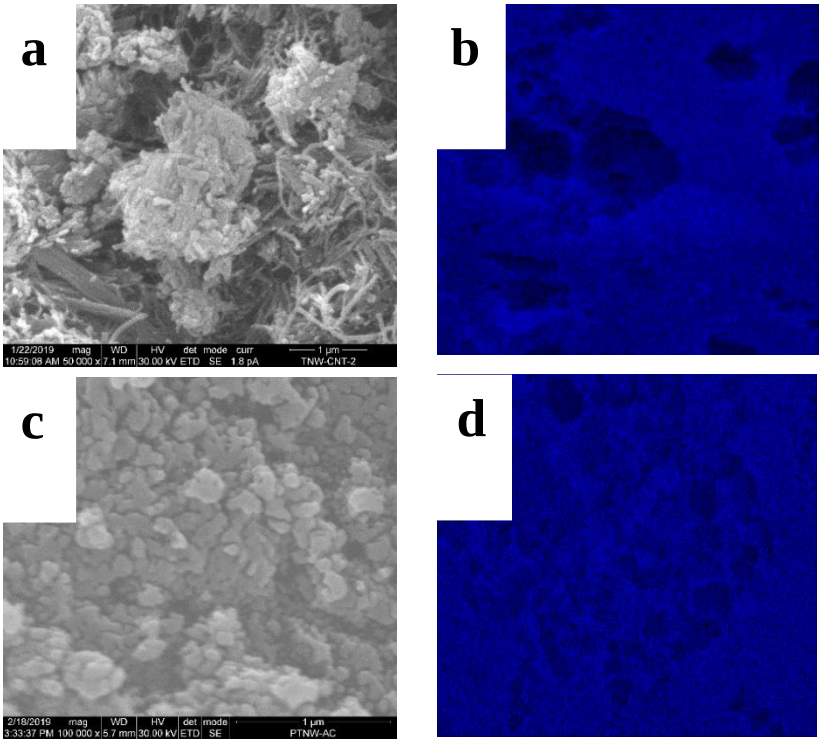

Figure 26 – SEM images of a) pTNWs/MWCNTs (2) and c) pTNWs/AC, and Titanium elemental mapping in b) pTNWs/MWCNTs (2) and d) pTNWs/AC

It is believed that the major difference in photoactivity between both samples emerges from the morphological nature of the different carbon allotropes used. The fine diameters of the MWCNTs allows for easier passing of P25 nanoparticles in the somewhat agglomerated MWCNTs. Upon hydrothermal treatment, a large amount of the titania NPs are forced to seemingly get stuck inside the CNTs, essentially decreasing surface coverage and increasing agglomeration of the photocatalytic titania. However, in the pTNWs/AC sample, **Figure 26 d** shows slightly better surface coverage of elemental titanium, compared to large vacancy spots in **Figure 26 b**, corresponding to pTNWs/MWCNTs (2). The morphology of grinded granular AC allows for the majority of the heterojunction to form on the surface, whereby a large internal pore structure of the AC remains free of titania. This perhaps has a symbiotic effect, whereby high adsorption of AC micropores is maintained, whilst the photoactive titania has an increased surface coverage density.

The surface morphology of untreated and treated pTNWs/MWCNTs, prepared with untreated pTNWs, was examined using TEM in order to better understand the effect of surface treatment on the photoactivity of titania. The results in **Figure 27** show a clear surface distinction, whereby the treated nanowires exhibit roughened surface edges with fewer nano-shred morphologies of titania populating the surface nanowire. It is unclear how this may yield beneficial in a photodegradation scheme, but perhaps roughened surface and edges allow for less agglomeration amongst the pTNWs along the MWCNTs length – this can also be seen when comparing **Figures 27 a and b**. This

finding, if true, sheds light on the benefit of surface treatment in higher dimensional (over 1-D) titania morphologies and probes on to the effect of photocatalyst agglomeration in a nanocomposite. Very distinctive surface heterojunction can be seen between the titania nanowires and the MWCNTs in both samples.

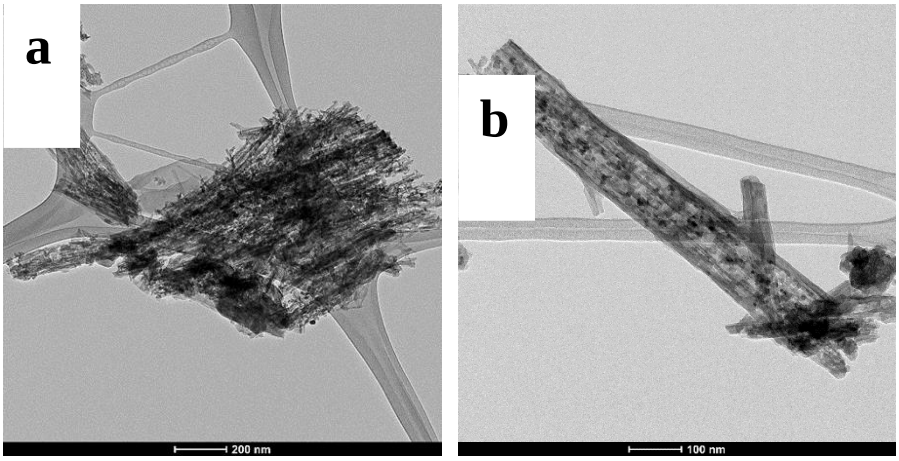

Figure 27 – TEM images of a) untreated pTNWs/MWCNTs (3), and b) surface treated pTNWs/MWCNTs (4)

To better understand the reasoning behind the unexpectedly hindered performance of MWCNT-incorporated titania-NWs with samples prepared using P25 as the preliminary titania precursor for the hydrothermal heterojunctioned and nanowire growth procedure, characterization of the materials' crystalline phases and crystallite sizes were performed and the results were shown in **Figure 29 a**. In order to yield an appropriate and relatable comparison when performing the powder XRD analysis, pTNWs/MWCNTs (2) data was compared with pTNWs/MWCNTs (4) and pTNWs/AC – whereby all samples were surface treated and calcinated under the same synthesis procedure.

It can be seen from **Figure 28 a** that obvious differences arise among the MWCNTs composited samples. Solely owing their differences in titania precursor used, the P25 precursory pTNW/MWCNT (2) sample shows an expectedly high anatase composition of about 82% compared to that of 91% present in the pTNW precursory pTNW/MWCNT (4) sample. It can also be seen from the XRD findings is the conspicuous broad peak at 2θ value of 10º present in pTNWs/MWCNTs (2). It was determined that this peak belongs to graphene oxide (GO) corresponding to an exposed facet of {101}. Although no graphene oxide was purposefully synthesized and added to the hydrothermal medium prior to NW growth, it seems that using P25 as the titania precursor in the presence of CNTs allowed for some formations of GO. The synthesis mechanism of this GO perhaps was facilitated through agglomerated P25/MWCNTs bulks – seen in **Figure 26 a** – whereby carbons in MWCNTs rearranged in GO formations. The presence of byproduct GO is not, however, found in pTNWs/MWCNTs (4) sample, which did not have a great deal of agglomeration as discussed in **Figure 27**. This strengthens the hypothesis that agglomeration of CNTs – facilitated by the incorporated hydrolyzed titania – under alkaline hydrothermal synthesis conditions allow for an allotrope to change from CNTs to GOs.

a

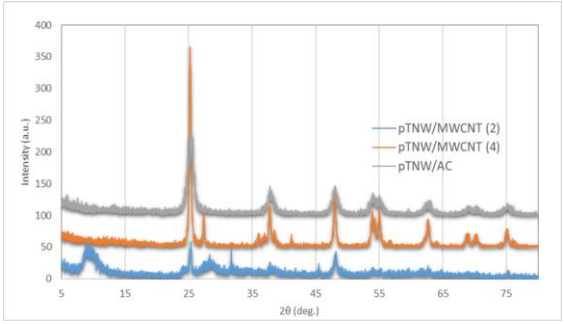

Figure 28- a) XRD patterns of surface treated pTNW/MWCNT and pTNW/AC and b) Crystallite Sizes approximated using Scherrer equation

Figure 28 Continued

b

Sample	Phase (%)			Avg. Crystallite Size (D) (nm) - Sherrer Equation
	Anatase	Rutile	Brookite	
pTNW/MWCNT (1) (no st, 400 calc)	81.7	4.6	13.7	3.49
pTNW/MWCNT (4) (st and 400C calc)	91.3	8.7	---	19.78
pTNW/AC (st and 400C calc)	28.6	---	71.4	7.91

Moreover, it can be seen from **Figure 28 a** that the highly photoactive samples of pTNW/MWCNT (4) and pTNW/AC both show a more crystalline structure with that of pTNW/MWCNT (2). A significantly higher anatase phase is present in pTNW/MWCNT (4) compared with all other carbon composited pTNW samples. Considering this finding as well as the superior photoactivity of pTNW/MWCNT (4) compared to other samples, it can be deduced that the effect of crystallinity on photoactivity in titania nanocomposites is still significant.

Furthermore, in an effort to further explain the photodegradation findings aforementioned, samples' crystallite sizes were approximated using Scherrer equation in **Figure 19 b**. The findings show that firstly, crystallite size of the pTNW/MWCNT (2) is an astoundingly low 3.5 nm, as was discussed earlier. The remarkable thing is that it was earlier discussed that P25 – the titania precursor used – has an average crystallite size of about 18 nm. The reduction in crystallite size can be explained via the conventional nanowire growth scheme, whereby titania molecules are grown through a top-bottom mechanism. In doing so and factoring in the large degree of agglomeration present in the nanocomposite even prior to heterojunctioning between the titania and CNTs, the titania nanoparticles seemingly did not have enough time to grow into nanowires. Moreover,

the same effect perhaps led to the relatively low crystallite size (7.9 nm) present in the pTNW/AC sample – which also had P25 as the pTNW precursor. The pTNWs/MWCNTs (4) sample shows a large average crystallite size of 19.8 nm. This shows that during the hydrothermal treatment process to form heterojunctions between the CNTs and as prepared pTNWs, further elongation of the pTNWs occured.

It is this finding of major difference in crystallite size between pTNWs/MWCNTs (4) and pTNW/AC that led to the slight decrease in photoactivity of pTNWs/AC than what could have potentially resulted in a more photoactive sample if as prepared pTNWs were used as the titania precursor in fabricating a pTNWs/AC sample.

Additionally, in order to quantify the bandgap energy of the pristine titania composites, the utilization of Tauc equation was employed and presented in – **Figure 29 b**. Due to the addition of black carbon allotropes – either MWCNTs or AC – to the white titania samples prior to the surface binding hydrothermal process, the final product has a grayish color. This means that if effective heterojunctioned are formed between the carbon and titania, then the apparent absorption spectra and bandgap approximations are accurate. In order to further evaluate this argument, FTIR spectra were collected for a nanocomposite sample – pTNWs/MWCNTs (4) – in order to investigate the presence of bonds between titanium and carbon.

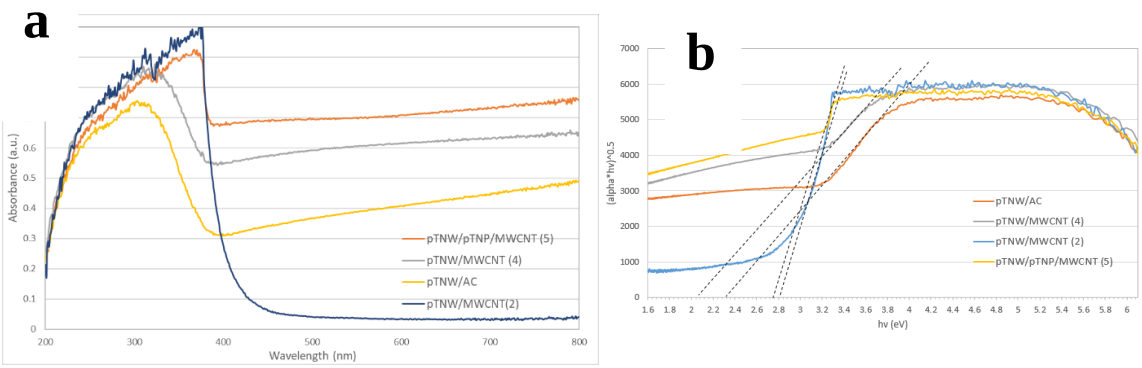

Figure 29 – a) Solid-state UV-Vis-NIR spectra and b) Tauc plots for bandgap energy approximations of pTNW/MWCNTs and pTNW/AC

The solid-state UV-Vis-NIR shows clear visible light absorption for both the AC composited sample and the MWCNT composited sample (4). Due to the full visible spectra absorbance of both MWCNTs and AC, their presence in the sample in small amounts should come to no surprise in increasing the absorption of the composited sample. Correspondingly, the bandgap energies approximated for the samples are 2.80 eV for pTNW/MWCNT (2), 2.75 eV for pTNW/pTNP/MWCNT, 2.35 eV for pTNW/AC, and 2.08 eV for pTNW/MWCNT (4). Since the amount of carbon allotrope to titania was maintained in all samples, the differences in absorption spectra and bandgap approximations show that there's a varying degree of intertwinement and effective heterojunctions created between the carbon allotropes and titania nanostructures. However, in order to accurately determine whether the bandgap energy approximations are representative of the materials, the identification of bonds between carbon and titania need to be first identified.

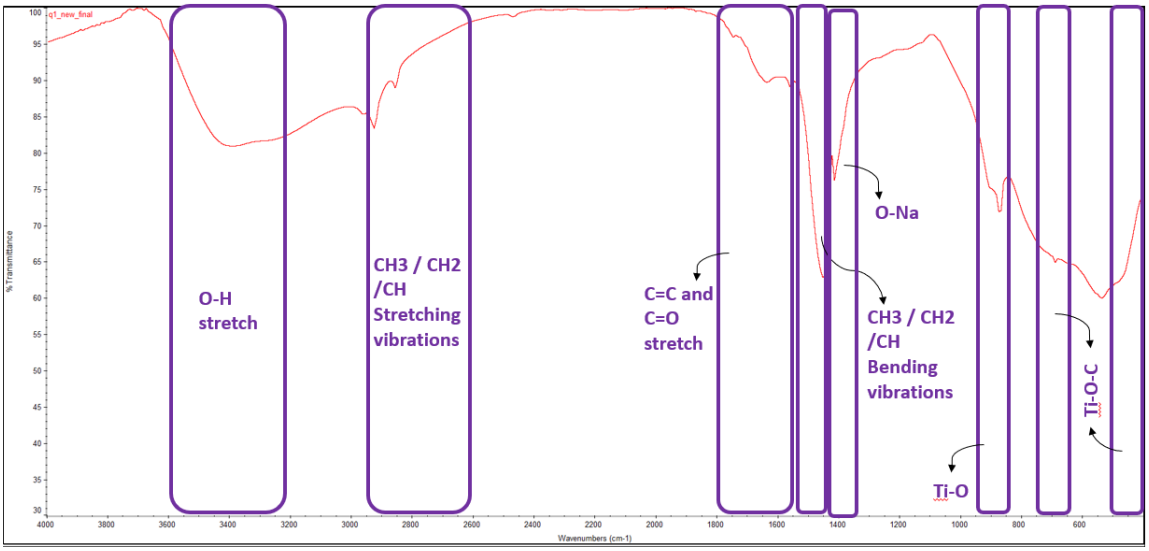

Figure 30 – FT-IR spectra of pTNW/MWCNT (4)

Figure 31 above depicts the FTIR spectrum of pTNW/MWCNT (4) nanocomposite, in the range of 400-4000 cm^{-1}. Clearly, the obtained spectrum revels the presence of the distinctive broad peak at 3440 cm^{-1} – corresponding to O-H bonds which is indicative to the presence of surface adsorbed H_2O molecules and hydroxyl groups. Moreover, a slight distinctive peak corresponding to an O-Na stretching vibration is recorded at 1350 cm^{-1}. This is most likely surface adsorbed to titania from the heterojunctioning procedure that used alkaline NaOH [10M]. The presence of the Ti-O bond for titania is presented through a strong peak at about 930 cm^{-1}. The presence of the composited MWCNTs can be seen extensively witnessed through multiple aliphatic asymmetric and symmetric stretches, namely CH3/CH2/CH stretching vibrations at 2978 cm^{-1} and 2878 cm^{-1}. Bending aliphatic vibrations can be seen through the sharp peak at 1450 cm^{-1}. The ever-distinctive functional groups for CNTs, namely C=C (1570 cm^{-1})

and C=O (1670 cm^{-1}) are also present. However, what ensures the effective chemical heterojunctioning between the titania and carbon allotrope are the two peaks at 480 cm^{-1} and 710 cm^{-1} corresponding to different vibrational/bending stretches of the heterojunctioned Ti-O-C bond.

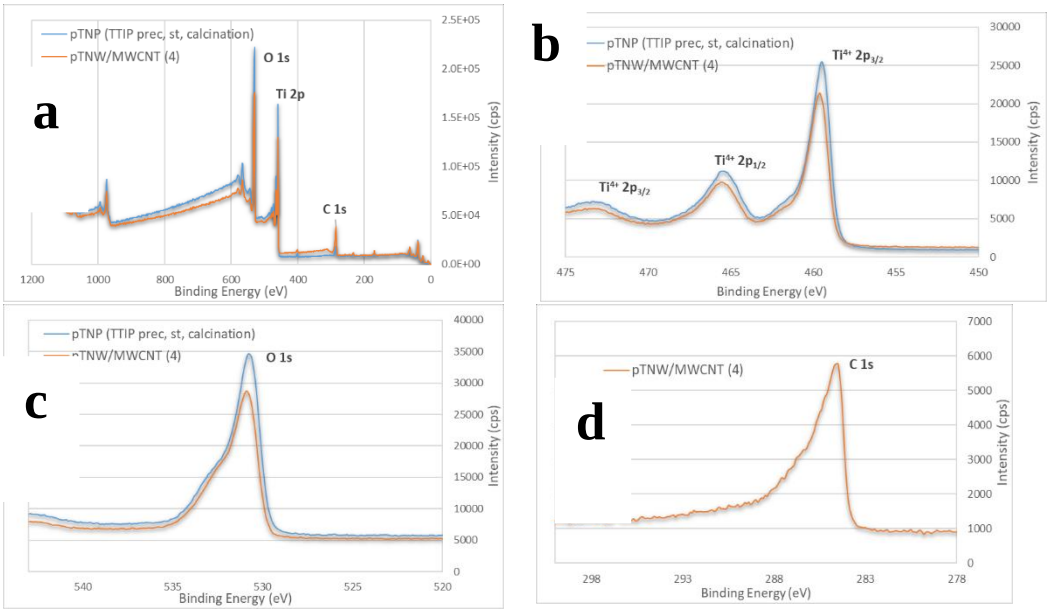

Figure 31 – a) Full-scale XPS survey and b) Ti2p survey c) O1s survey and d) C1s of pTNP (TTIP prec, st, calcination) and pTNW/MWCNT (4)

As can be seen from **Figure 31**, a thorough full survey XPS comparative analysis was conducted between the surface treated and calcinated pTNPs and pTNWs/MWCNTs (4). The nanoparticles were chosen for comparison in order to check for the presence, or lack thereof, of any oxygen vacancies, oxidation states of titanium, and heterojunctions between carbon and surface titania. Briefly, **Figure 31 b** shows maintained peak values for surface titanium, with no notable shifts in binding energies. Ti^{4+} 2p3/2 and Ti^{4+} 2p1/2 are both present with no apparent presence of reduction in forming the Ti^{3+} oxidation

state. It is worth noting that the slight reduction in peak area for both **Figure 31 b and c** in the pTNW/MWCNT (4) sample is due to the presence of elemental carbon in this sample – effectively reducing the elemental area of titanium and oxygen (titania). Main peak area of pTNW/MWCNT (4) in **Figure 31 c** is actually composed of two peaks –, the main peak at 530.7 eV and a broader peak at 532.1 eV. The main peak, present in both samples, corresponds to lattice oxygen (O_2^{2-}) in titania. The broader peak, however, can be ascribed to C=O or Ti-O-C heterojunctions between titania and the carbon allotrope – confirming FTIR results regarding the successful heterojunctioning. **Figure 31 d** represents the spectrum of C 1s, whose area is comprised of 3 main peaks – namely at 283.7 eV, 284.3 eV, and 286.8 eV. The first two peaks at 283.7 eV and 284.3 eV correspond to sp^2 and sp^3 carbons, respectively. Both carbon orbitals are representative of MWCNT 1s carbons. Interestingly, however, the last sub-peak at 286.8 eV corresponds to O-C=O which effectively can form anchoring functionalities for titania in forming heterojunctioning bonds.

Reduced (Black) Titania-Based Nanostructures and Nanocomposites – bTNPs, bTNWs, and bTNW/MWCNT

Given that in previous sections a clearer understanding of the effect of crystalline phase, crystallite size, morphology, heterojunctions and other photocatalyst design parameters have been studied and optimized to curb the rapid electron-hole recombination rate and improve photoactivity, this section will focus on enhancing the utilization of a greater fraction of the solar spectrum. As was mentioned before, pristine titania only utilizes the

UV area of the solar spectrum. Black titania offers the opportunity to expand the light absorption spectrum to a wider range.

Numerous works have been done on reducing pristine titania nanostructures, predominantly nanoparticles, to black titania nanostructures. These works showed improvement in visible light absorption. However, the procedures followed were associated with several downfalls including dangerous and expensive synthesis conditions (i.e. high-pressure hydrogenation), long reduction times, and a shift in certain intended design parameters from the pristine nanostructure. In this work, a simple, yet effective, reduction procedure has been utilized, which is physiochemical reduction using sodium borohydride ($NaBH_4$).

A certain molar ratio of the reducing agent is physically mixed with the solid pristine nanostructure, then the mixture is transferred to an aluminosilicate crucible in a tubular reactor. The reduction only progresses when the borohydride disassociates into boron and hydrogen, whereby the hydrogen introduces surface defects and oxygen vacancies. It is the surface defects that contribute to the color change of the naturally pasty-white titania nanostructures.

In order to reduce pristine samples effectively, different reduction temperatures and molar ratios of borohydride to titania were utilized. It was confirmed from previous studies that when employing sodium borohydride, the time of reaction becomes independent of surface defects after 1 hour of reaction/reduction time. Thus, 1 hour of reaction time was used for all reduction schemes, with a 30 minutes heating-up time and natural cooling-down time. All reductions were carried out in a pure argon atmosphere

since the presence of oxygen can ignite upon hydrogen disassociation from the borohydride. P25 was used as the model titania sample to optimize the reduction scheme. As can be seen from **Figure 33** below, it was found that a reduction temperature of 380 ºC and a molar ratio of 1.25:1 ($NaBH_4$: TiO_2) is optimum for generating the most photoactive titania sample. The most photoactive samples from preceding syntheses in ameliorating pristine titania nanowires and nanocomposites with MWCNTs, were used to generate their progressive reduced (black) counterparts.

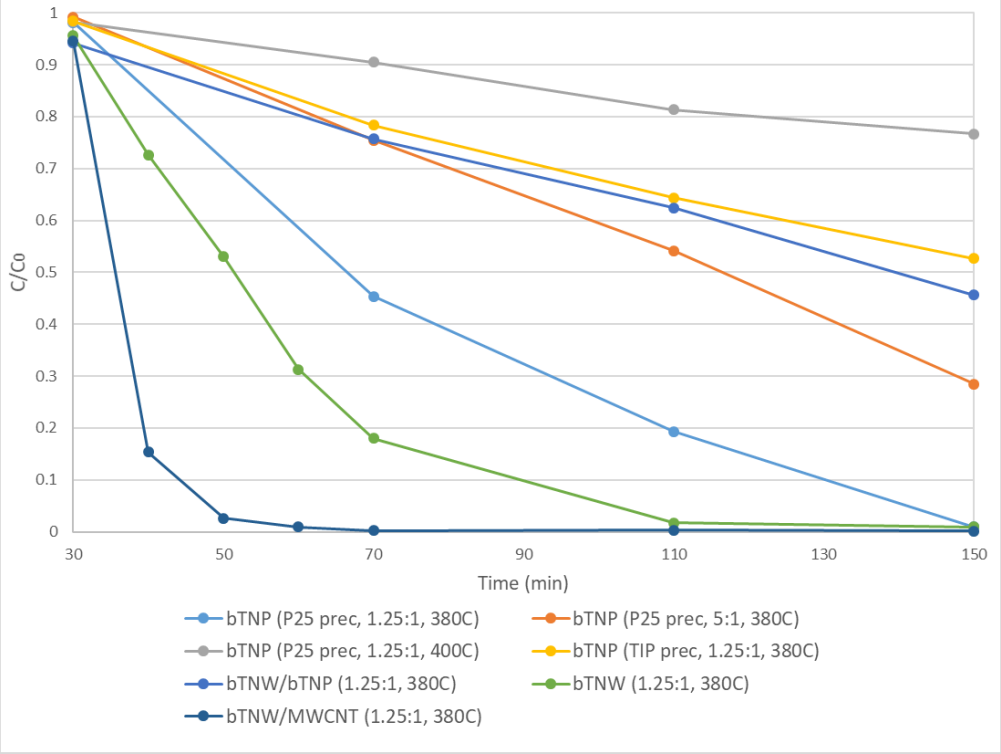

Figure 32 – Comparative photodegradation of MO (10ppm) under solar irradiation using physiochemically reduced (black) titania nanostructures and nanocomposites

The black samples clearly outperform their pristine counterparts in photodegradation of MO. The enhanced obsorption of visible light essentially allows for

more photoexcitation phenomena in the titania, in turn increasing the probability of successful photochemical reactions with time. 99.3% of MO was degraded in 2 hours under solar irradiation using the relatively simple structured black titania nanoparticles that have been optimally reduced from commercial P25. Surprisingly, increasing the molar ratio of borohydride to titania from 1.25:1 to 5:1, using the same reduction temperature and time, reduced photodegradation efficiency to 71.5% after the same reaction time of two hours. The reduction in photoactivity with increasing borohydride concentration can be attributed to the effect posed on crystallinity. Reductive hydrogen at high temperatures can significantly change the crystalline structure, size of crystallites, and increase aggregation of the final product. However, what is perhaps more elusive is the significant reduction in photodegradation to 23.3% in 2 hours irradiation when the temperature of reduction was increased by a mere 20 ºC. The reason for this is perhaps more challenging to explain, however previous work with hydrogenating titania concluded that reduction temperature has a significant impact on the ratio of bulk/surface defect states in the titania nanostructure. It is thus clear that utilizing the 1.25:1 molar ratio along with a reduction temperature of 380 ºC maintains the optimized design parameters of the pristine titania nanostructures and nanocomposites, whilst allowing for an optimum surface/bulk defect states ratio to be generated.

Adopting the optimized reduction scheme, pTNWs that were surface treated and calcinated used for generating the bTNWs resulted in a photocatalyst that yields a 98.2% photodegradation in 90 minutes of solar irradiation. Moreover, the black nanocomposite

of pTNWs/MWCNTs (4) had a remarkable 97.4% photodegradation of 10ppm MO in 20 minutes under solar irradiation. In order to better understand these results, characterization techniques were utilized to study the different effects that reduction had on the different design parameters of the photocatalysts that were synthesized.

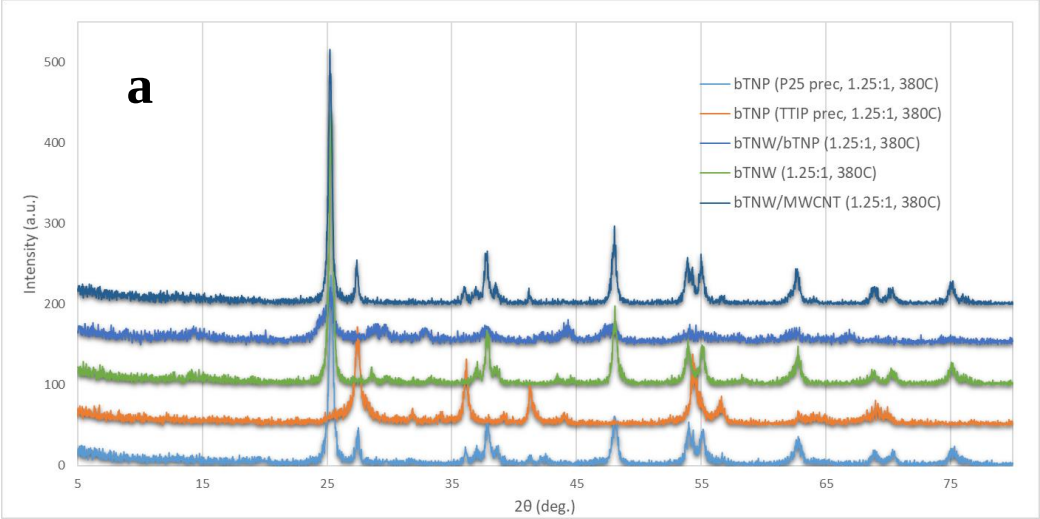

b

Sample	Phase (%)		Avg. Crystallite Size (D) (nm) - Sherrer Equation
	Anatase	Rutile	
bTNP (P25, 1.25:1, 380C)	91.1	8.9	17.92
bTNP (TTIP, 1.25:1, 380C)	---	100	15.18
bTNW/bTNP (1.25:1, 380C)	76	24	15.22
bTNW (1.25:1, 380C)	98	2	18.32
bTNW/MWCNT (1.25:1, 380C)	90.4	9.6	19.42

Figure 33- a) XRD patterns of and b) Crystallite Sizes approximated using Scherrer equation of reduced titania-based nanostructures and nanocomposites

First, in order to investigate how reduction with hydrogen from borohydride affects the crystallinity and crystallite sizes of the emerging reduced titania-based photocatalyst, XRD analysis has been performed and the data are presented in **Figure 34 a**. When comparing these results with the unreduced pristine samples counterparts, a pattern can be extracted. Essentially, utilizing this reduction scheme, a pristine sample

that was predominantly anatase would remain predominantly anatase upon reduction. This patterning in how crystal phase changings occur upon reduction has also been identified for other samples that have been reduced from their pristine supplements. However, one sample seems to severely violate this scheme, which is the bTNPs (TTIP precursor) from pTNPs (TTIP prec, st, calcinated). The pristine form of this particular sample was 100% anatase and upon reduction a complete phase shift to 100% rutile is witnessed. However, whenever P25 was used, or predominantly used, as the titania precursor in some nano-morphological change via synthesis, the pristine phase is maintained to a large degree. This is observed for bTNWs, bTNWs/MWCNTs, bTNPs (P25 precursor), and bTNWs/bTNPs. Thus, it can be deduced that for this reduction scheme, maintaining the crystalline phase of the pristine sample is highly dependent on the nature of titanium precursor used in synthesis.

Using Scherrer equation to approximate crystallite sizes and comparing the findings presented in **Figure 34 b** with those of their pristine correspondents, it can be deduced that, on average, the crystallite size does not significantly change during the reduction scheme. However, in some cases it does seem to be slightly disadvantageously reduced. This is quite a logical finding since this particular reduction procedure does not play a role on the bulk morphology of the nanostructures. Although, as was seen from the SEM images of reduced samples, bTNWs generated from reduction schemes involving higher reduction temperatures or higher reductant concentration, the morphology does in fact change from a seemingly ordered nanowire structure to a significantly fractured structure that is not very crystalline. Although not displayed, but

the XRD analysis for those samples were very noisy due to the highly amorphous distribution of fractured ‘nano-stubs’.

To ensure that no morphological change occurs during the reduction scheme utilized, **Figure 34** below depicts some TEM images taken for selected representative samples. As can be seen, there is in fact no evident change in morphology during reduction. However, there is slight agglomeration substantiated for bTNPs compared to the pTNPs. This agglomeration tendency is however seemingly nonapparent for nanowires and nanocomposites with MWCNTs, which is advantageous. Generally, agglomeration in nanomaterials utilized for aqueous media reduces the effective exposed surface area necessary for a reaction to take place on.

The black nanocomposite sample – bTNW/MWCNT – was also analyzed using TEM elemental analysis in order to ensure that no resultant impurities are present upon final preparation of the reduced photocatalyst. The slightest impurities (i.e. boron) can severely cripple photoactivity if unchecked. The elemental analysis is depicted in **Figure 35** whereby no impurities have been found a uniform coverage of the MWCNTs is maintained upon reduction.

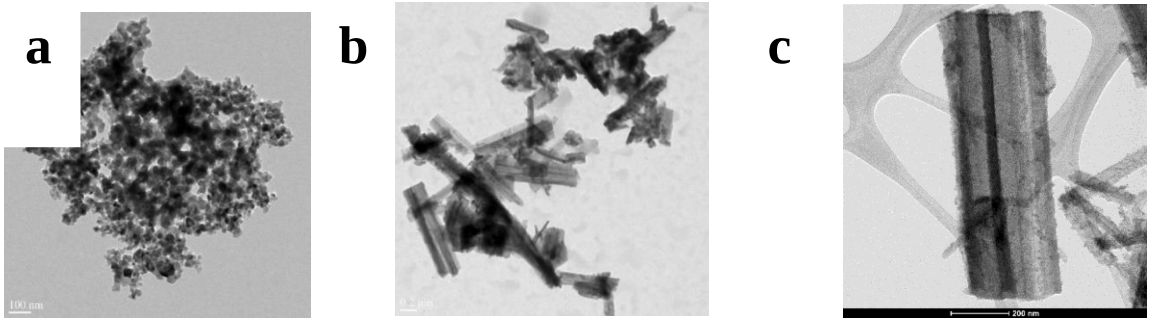

Figure 34 – TEM images of a) bTNP (P25, 1.25:1, 380C) b) bTNW (1.25:1, 380C), and c) bTNW/MWCNT (1.25:1, 380C)

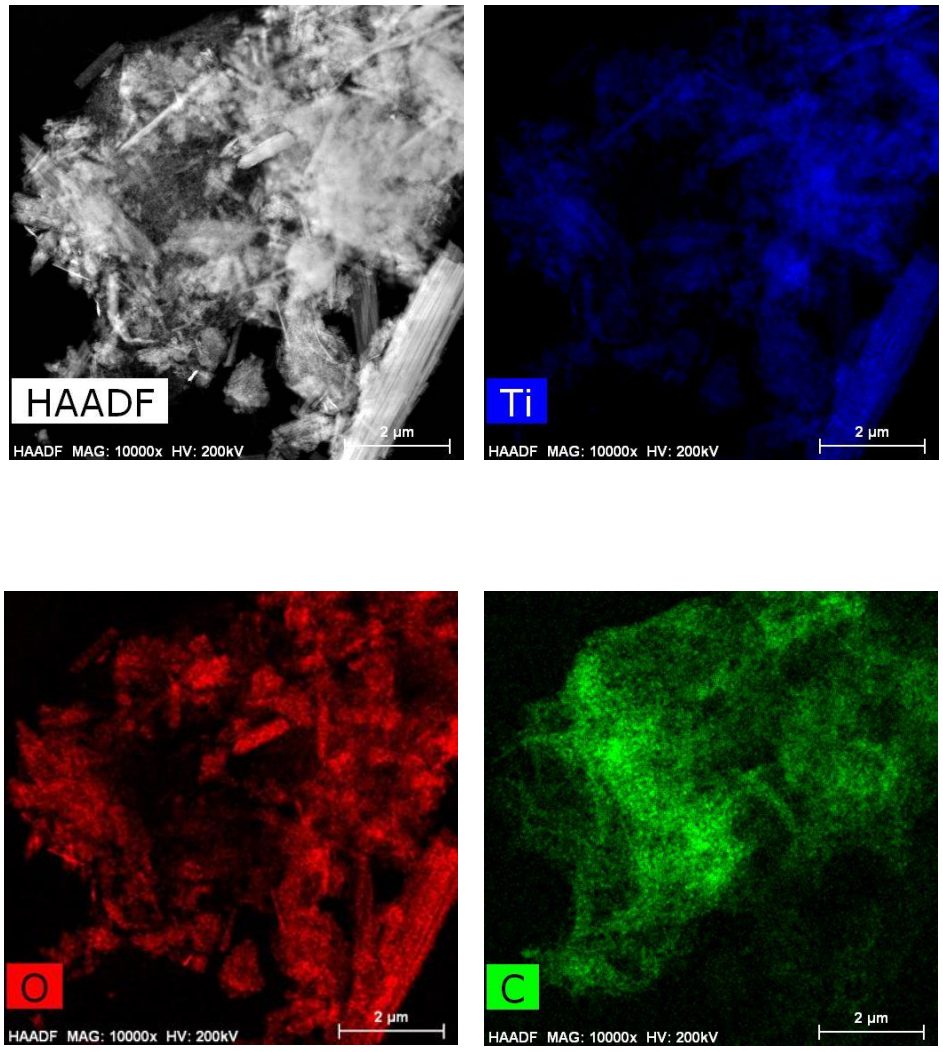

Figure 35 – TEM elemental analysis on bTNW/MWCNT (1.25:1, 380C)

During the reduction procedure the reducing hydrogen, generated from the high temperature induced dissociation of borohydride, effectively removes oxygen atoms from the ordered titania lattice. This introduces oxygen vacancies in the structure of the lattice and reduces surface titanium ions from the 4+ oxidation state to the 3+ oxidation state. The reduction of Ti lattice positions is predominantly due to the migration of excess electrons remaining after the generation of the oxygen vacancies. These excess

electrons can also maintain their position at oxygen vacancy sites, whereby constituting electron-rich oxygen vacancies. Such effects are generally allocated to the discussion of structural defects of a material. It is these structural defects that result in the coloring of pasty white titania to darker colors (i.e. black). Black titania is renowned for its enhanced property of utilizing the solar energy, which occurs via the narrowing of bandgap energy during reduction. **Figure 36** below shows solid-state UV-Vis-NIR analyses and the corresponding Tauc plots used to approximate the bandgap energies of the black titania nanostructures and nanocomposites. It is clear from the results that all reduces samples have had their bandgaps successfully narrowed from their pristine counterparts, and as can be seen from **Figure 36 a**, they all have a significantly improved absorbance into the visible light segment of the solar spectrum.

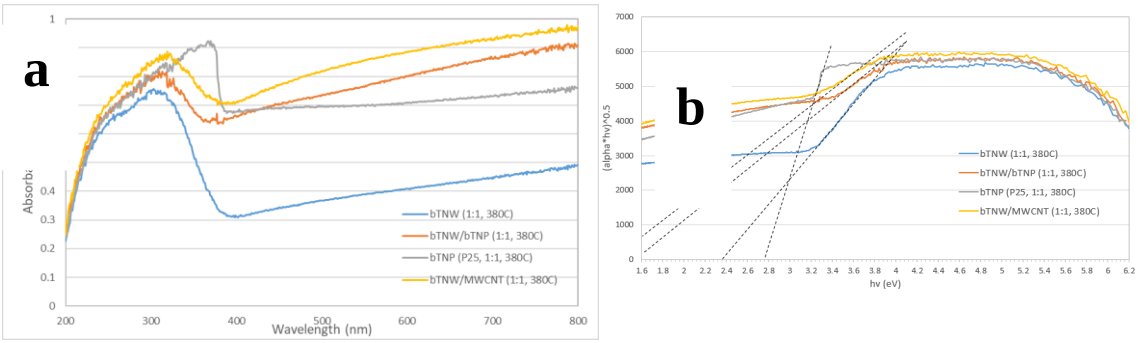

Figure 36 – a) Solid-state UV-Vis-NIR spectra and b) Tauc plots for bandgap energy approximations of reduced titania nanostructures and nanocomposites

Reduction using sodium borohydride has been favored recently, and utilized in this work, due to the propagation of high concentrations of oxygen vacancies via relatively medium reduction temperatures, and at atmospheric pressures. The narrowing of the bandgap energy in reduced (black) titania samples can be attributed to the generation of donor energy states which reside below the CB – much like the narrowing of bandgap upon carbon allotrope heterojunctioning with titania.

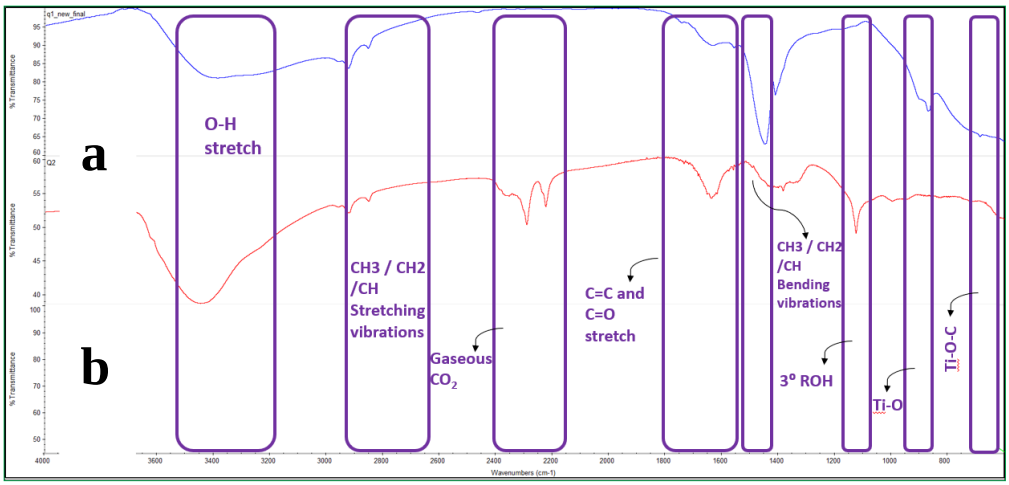

Figure 37 – FT-IR spectra of a) pTNW/MWCNT (4) and b) bTNW/MWCNT (1:1, 380C)

In comparing the FTIR specra of both the unreduced (pristine) and reduced TNW/MWCNTs, several significant differences can be immediately noticed. Firstly, the intensity in the O-H stretches for the reduced sample (**Figure 37 b**) is notably increased, which is directly associated with surface defects and oxygen vacanies introduced during reduction. The higher the intensity of O-H stretches, the higher the corresponding surface defects are likely to be. Although from peak characteristics, aliphatic stretching vibrations remain seemingly unchanged, the corresponding bending vibrations are

significantly decreased upon reduction. The introduction of surface defects to certain species (titania) of a nanocomposite can inadvertently introduce some structural hinderences for the carbon allotrope, reducing bending vibrational modes. This however, should have little to no effect on the apparent photoactivity of the reduced nanocomposite. Two characteristic peaks can be identified in the 2250-2350 cm^{-1} range, which correspond to gaseous carbon dioxide adsorbed through the defected surface structure of the reduced sample. The hydroxylation of the surface upon hydrogenation also resulted in a notable peak at 1150 cm^{-1} corresponding to a C-O-H stretch of a tertiary alcohol. Interestingly, there is a substantial reduction in peak intensity in the 600-950 cm^{-1} range. Two main functional groups reside in this region, namely the Ti-O and Ti-O-C bond stretches. The reduction in peak intensiry in this area is highly indicative, and further confirmates, the introduction of oxygen vacancy sites. By definition, no Ti-O or Ti-O-C bonds can form in the presence of an oxygen vacancy since oxygen is required in forming these bonds.

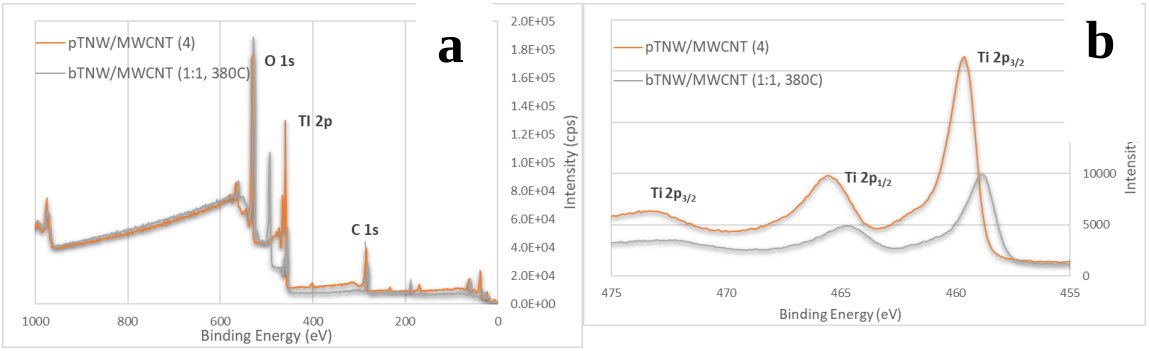

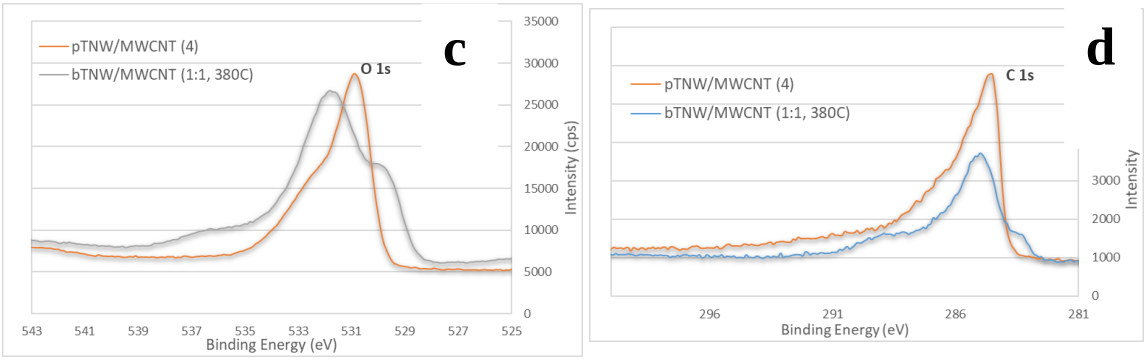

Figure 38 – a) Full-scale XPS survey and b) Ti2p survey c) O1s survey and d) C1s of pTNW/MWCNT (4) and bTNW/MWCNT (1:1, 380C)

A full-scale XPS survey was carried out on bTNW/MWCNT (1:1, 380C) and the results were compared with previously obtained XPS results of pTNW/MWCNT (4) – the reduced nanocomposite's precursor. The results, seen in **Figure 38**, shows some notable differences in the elemental surveys. The Ti 2p peaks were preliminarily analyzed to determine the presence and degree of reduced titanium in the Ti^{3+} oxidation state. The Ti^{4+} oxidation state has two dominant peaks at 459.6 eV and 465.4 eV corresponding to $Ti2p_{3/2}$ and $Ti2p_{1/2}$ respectively. A lower binding energy shift of about 0.8 eV correspond to the same $Ti2p_{3/2}$ and $Ti2p_{1/2}$ peaks with the Ti^{3+} oxidation state. What can be seen from **Figure 38 b** is the positioning of the pristine nanocomposite's peaks at the locations of unreduced titanium's oxidation state of 4+. The notable shift in the binding energies of the $Ti2p_{3/2}$ and $Ti2p_{1/2}$ peaks for the bTNW/MWCNT (1:1, 380C) sample are due to the reduction of Ti^{4+} to the reduced Ti^{3+} state. For titania-based nanostructures, oxygen's 1s orbital peak is composed of two peaks, namely the predominant Ti-O peak of titania positioned at 529.9 eV and the O-H hydroxyl peak at 531.4 eV. Although both peaks are present in both samples, a significant increase in the

area of the O-H peak is observed for the reduced nanocomposite, which is indicative of oxygen vacancies and surface defects – substantiating FTIR findings discussed above. Although not performed in this work, Electron Paramagnetic Resonance (EPR) can indirectly show the concentration of surface to bulk Ti^{3+} which is detrimental in enhancing photoactivity under visible light irradiation. Peaks at 286 eV and 288.2 eV corresponding to heterojunctioning between the carbon and titania are in fact maintained in the reduced sample, which as discussed previously is extremely beneficial for maintaining a high photoactivity by ensuring the optimum utilization of the conductive carbon allotrope and in effect reducing the electron-hole recombination rate upon photoexcitation.

Reduced (black) Paramagnetic Titania-Nanocomposite – bTNW/MWCNT@SiO_2@Fe_3O_4

Although a highly photoactive photocatalyst offers a clean and effective method in effectively removing organics from contaminated water sources, the hindrance that is prolonging its commercial applications can be truncated to two main factors. Firstly, most photocatalysts are not visible light driven and as such would only utilize a fraction of the available solar energy. However, as has been discussed, a myriad of different reduced (black) titania-based photocatalysts have been developed to effectively utilize a greater section of the previously wasted solar energy – including the final photocatalyst developed in this work bTNW/MWCNTs. The second, and perhaps more challenging

predicament, is the design and recyclability of the photocatalytic nanoparticles employed during treatment.

The second conundrum has been approached via a few ways, most prevalent of which is either by having a photocatalytic membrane or, the method employed in this work, introducing an effective method to collect the catalyst once homogenously dispersed in the reactor volume. The problem that has historically been crippling the former method has been in the ineffective design of a photocatalytic membrane reactor system and in the employment of photocatalytic membranes that require a prolonged residence time to effectively degrade the contaminants.

Thus, the employment of a paramagnetically photoactive photocatalyst that can both efficiently utilize the solar spectrum's energy availability to a high degree and can be methodically collected via the presence of a small magnetic field would make photocatalytic water treatment more feasible for commercial application.

Paramagnetic iron oxide micro/nanospheres that can effectively act as templates for the chemical deposition of the developed bTNW/MWCNT (1:1, 380C) photocatalyst atop the core was developed. However, in order to prevent a disadvantageous heterojunction between the Fe_3O_4 core and the photoactive titania, a silica coating was applied atop the paramagnetic core prior to deposition of the photocatalyst.

Initially, it was thought that a direct homogenous mixture of both the bTNW/MWCNT (1:1, 380C) and the $Fe_3O_4@SiO_2$ cores in an aqueous solution prior to filtration and calcination would lead to the final paramagnetic photocatalyst. However,

the surface chemistry of the amorphous silica coating and the bTNW/MWCNTs would not allow for any kind of chemical bridging, only physical amalgams that quickly separated the paramagnetic cores during a magnetic field and left the active photocatalyst dispersed in solution.

Therefore, the prepared bTNW/MWCNT (1:1, 380C) photocatalyst was grown atop the paramagnetic spheres in order to effectively fabricate the bTNWMWCNT@SiO_2@Fe_3O_4 paramagnetic composite. Briefly, the iron oxide cores were synthesized via an established hydrothermal procedure discussed in Chapter III. The silica coatings were applied using TEOS as the silica precursor in a wet chemistry-based synthesis procedure. TTIP was added to an amount of Fe_3O_4@SiO_2 cores in solution prior to their hydrothermal-assisted hydrolysis to titania nanoparticles. Growing the nanowires was rather tricky, since direct alkaline-based hydrothermal growth of the prepared pTNP@ Fe_3O_4@SiO_2 would result in pTNW@ Fe_3O_4@SiO_2 with very low surface coverage of titania. Therefore, P25 was first added to the hydrothermal medium prior to nanowire growth, followed by the MWCNTs hydrothermal addition procedure. Finally, in order to obtain the reduced paramagnetic sample, the same reduction scheme used on pTNW/MWCNT (4) to generate bTNW/MWCNT (1:1, 380C) was utilized.

Due to the magnetic properties of the synthesized final composite, photodegradation experiments could not be performed using magnetic stirring for mixing but rather they were carried out on a mechanical shaker under vertical illumination of light employing the same solar simulator used for testing the photodegradation performance of non-magnetic samples. The results are summarized in **Figure 39** below.

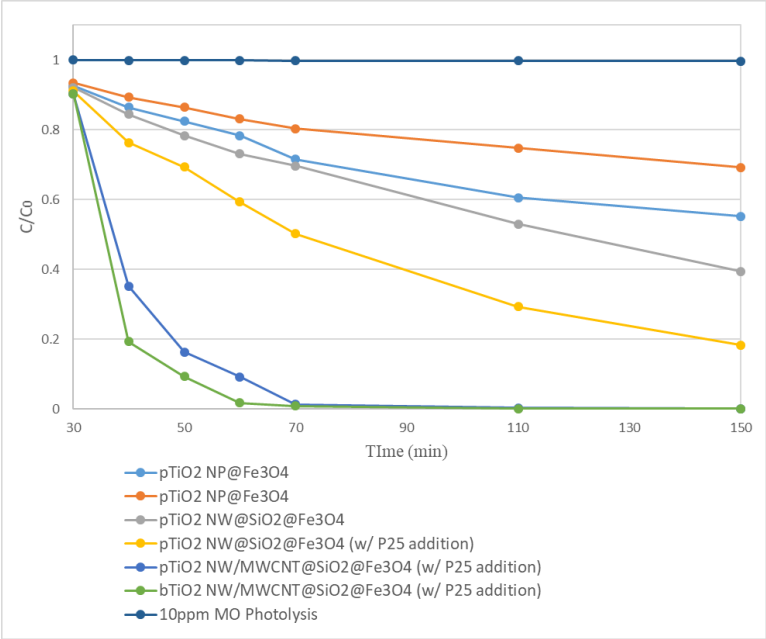

Figure 39 – Photolysis and comparative photodegradation of MO (10ppm) under solar irradiation using paramagnetic reduced and pristine nano-titania composites, where C/C0 is the contaminant remaining and time is the actual irradiation time

As can be seen from **Figure 39** above, the incorporation of photoactive titania nanocomposites yielded an enhanced photodegradation efficiency in the iterative steps undertaken to reach the final paramagnetic bTNW/MWCNT@ Fe_3O_4@SiO_2 which reached a photodegradation efficiency of 98.2% after 40 minutes of solar irradiation. There is a slight, albite a negligible, decrease in photodegradation efficiency when comparing the paramagnetic composites to their stand-alone photocatalysts discussed

earlier in the chapter. This, however, can be attributed to several factors including the employment of a catalyst loading rate of 1 g/L for the stand-alone composites, and 2 g/L for the paramagnetic composites. The increase in catalyst load for the latter is due to the presence of heavy iron oxide and silica portions of the composite. However, even in doing so, the net presence of photoactive titania in the paramagnetic samples is slightly less than that when the stand-alone titania nanocomposites were used to photodegrade the contaminant. Moreover, aggregation effects for magnetic particles tends to be higher, which in turn reduces the exposed effective surface area of the composite leading to a slight decrease in photodegradation efficiency.

XRD analysis has been performed on selected paramagnetic samples in order to verify the crystallinity of the different materials incorporated in the composite. **Figure 40** below verifies the successful synthesis of all iterative samples fabricated. The pronounced peaks of Fe_3O_4 can be seen in all paramagnetic samples through 2θ values of 30.3º, 35.6º, 35.6º, 43.1º, 57.1º, and 62.6º, which correspond to the characteristic cubic spinal structure of Fe_3O_4 (JCPDS 75-1609). Upon applying the silica coating on the iron oxide cores, the subtly weak broad peak around 25.3º corresponding to the amorphous silica shell later atop the core is found. The amorphous silica peak is distorted in the

presence of titania atop the coating, since the notable anatase peaks of titania are found at 2θ values of 25.2º and 48.3º.

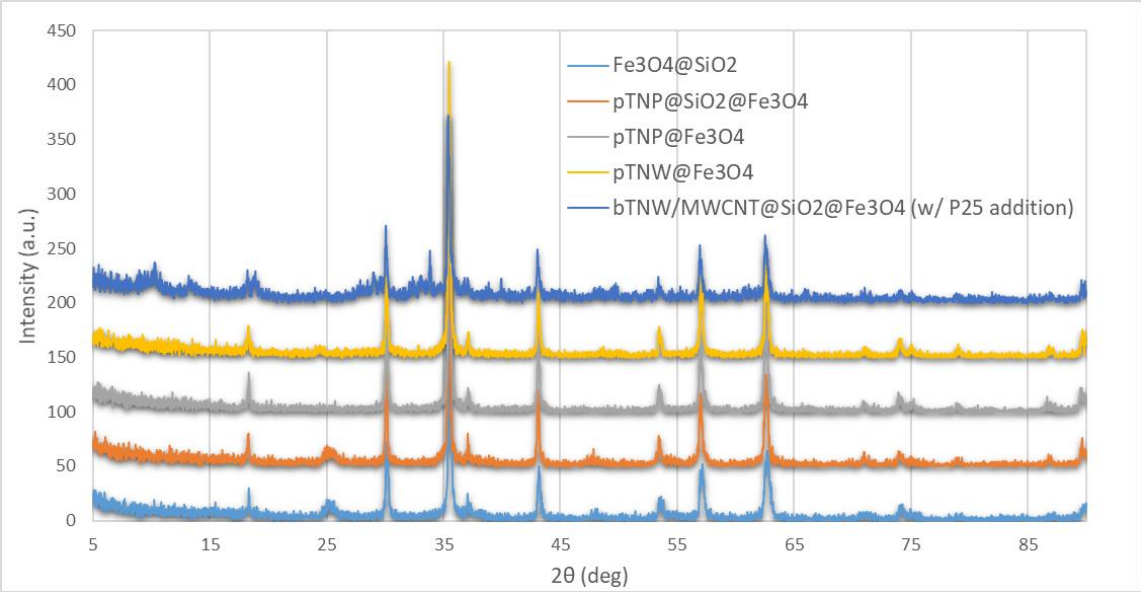

Figure 40- XRD patterns of paramagnetic titania-based photocatalytic samples

In order to ensure the morphological soundness of the as synthesized paramagnetic nanospheres and to ensure well surface coverage of titania atop the magnetic cores, as well as effective formation of nanowires. SEM imaging of a selected representative array of samples have been depicted in **Figure 42** below.

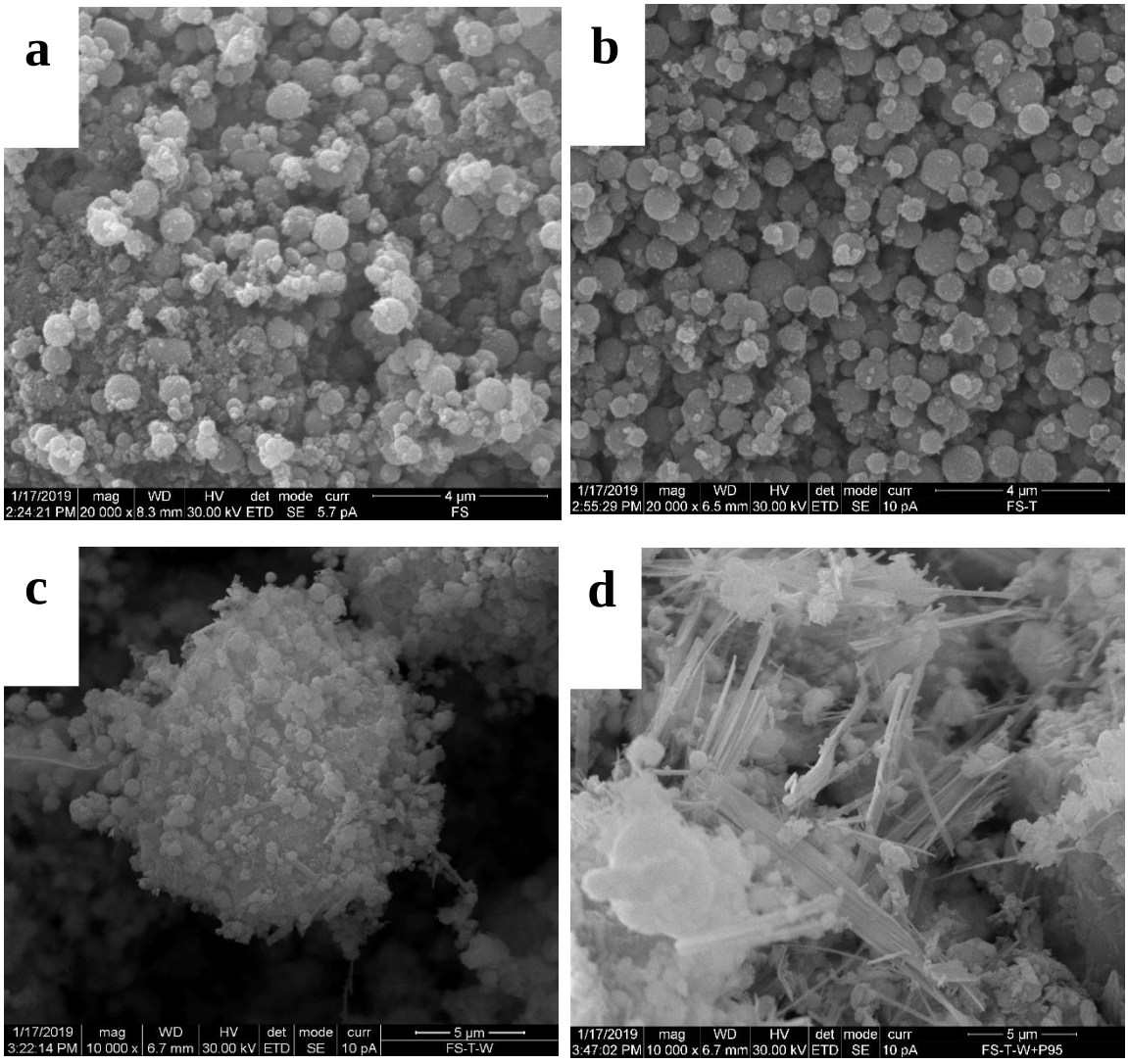

Figure 41- SEM images of paramagnetic a) Fe_3O_4@SiO_2, b) pTNP@SiO_2@Fe_3O_4, c) pTNW@SiO_2@Fe_3O_4, and d) pTNW@SiO_2@Fe_3O_4 (with P25 addition)

Significant morphological changes are among different samples and can be observed. The deposition and hydrolysis of titania nanoparticles atop the paramagnetic silica-coated iron oxide seems to result in a more ordered general morphology of spherical nanocomposites, which could highly be attributed to the resuming of

hydrothermal treatment of the paramagnetic composites. Relatively poor surface coverage of titania nanowires can be seen in **Figure 41 c** and a high degree of aggregation is also witnessed. However, a substantial increase in surface coverage atop the paramagnetic cores, lengthier and more exposed nanowires are observed in **Figure 41 d**, which included the addition of P25 prior to nanowire alkaline hydrothermal growth.

Interestingly, the pTNW@SiO2@Fe3O4 (w/ P25 addition) sample maintains its ease of magnetic retrievability even though the expected micro/nano-spherical deposition of the photoactive titania nanotubes seems to be loosely attached to the surface of the cores. This accentuates the presence of strong heterojunctions between the titania and silica layers, that do not affect the photoactivity of titania negatively. This can be examined using FTIR to potentially observe Si-O-Ti bridging bonds, but can also be seen in **Figure 42 d**.

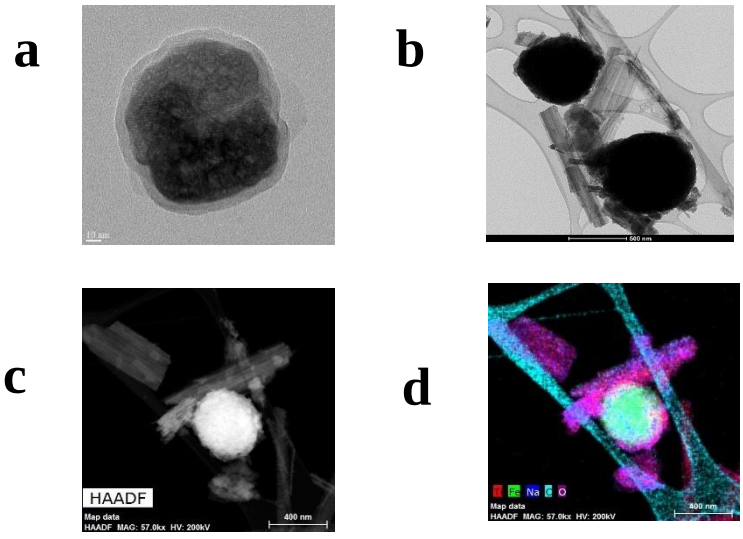

Figure 42- TEM images of paramagnetic a) Fe_3O_4@SiO_2, b) pTNW@SiO_2@Fe_3O_4 and c), d) TEM elemental analysis of pTNW@SiO_2@Fe_3O_4 (with P25 addition)

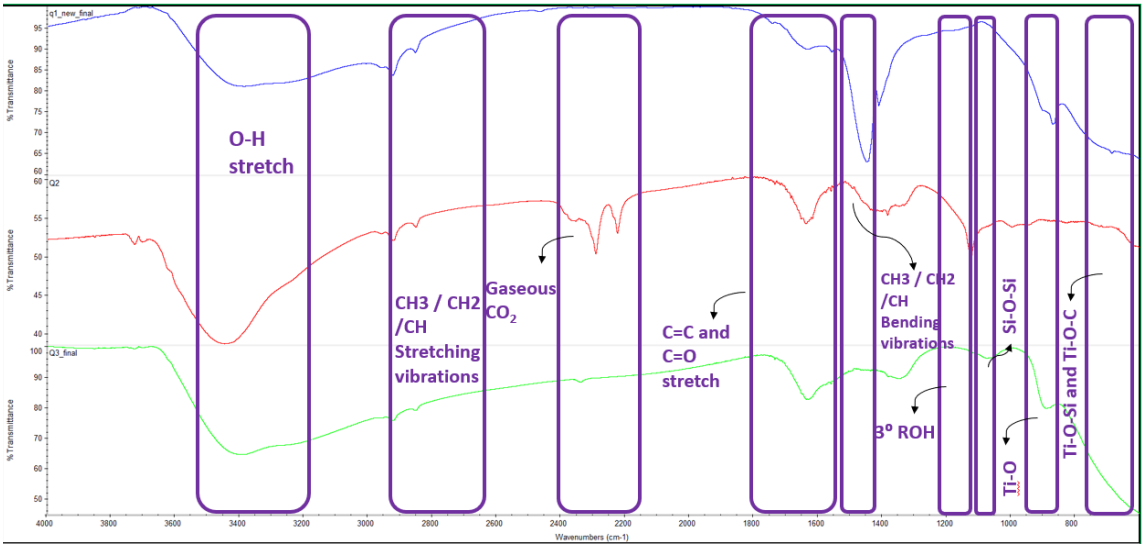

Figure 43 – FT-IR spectra of a) pTNW/MWCNT (4), b) bTNW/MWCNT (1:1, 380C), and c) pTNW@SiO_2@Fe_3O_4 (with P25 addition)

FTIR analysis was systematically performed and is demonstrated in **Figure 43** above in order to prove the heterojunctioning of titania with the amorphous silica layer atop the paramagnetic core and in order to chemically prove the presence of characteristic silica coatings in the final paramagnetic nanocomposite structure. The peak at 1095 cm^{-1} depicts the presence of Si-O-Si bonds which preliminarily proves the successful silica coating even after the hydrothermal nanowire growth procedure atop it. The degree in which the peak is present is representative of the degree of silica exposed. Since the sample analyzed has a high surface coverage of titania nanowires as seen from morphological imaging in **Figure 42 d** and **Figure 42 b-d**, the degree of exposed silica is minimized. What is quite reassuring in terms of effective synthesis is the silica-titania bridging bond that verifies the formation of heterojunctioning between the core surface

and photoactive nanostructure. This can be seen in the overlapping peak area, with the Ti-O-C heterojunctioning peak, at approximately 910 cm^{-1}.

Thus, as was seen from the aforementioned characterizations of the final paramagnetic photocatalyst, their is good agreement in terms of the morphological, crystalline, and photoactive degradation efficiencies exhibited from the developed bTNW/MWCNT (1:1, 380C) visible-light driven photocatalyst. The paramagnetic property of the composite ensures the effective collection of the material from the treated water in a few seconds upon applying a small magnetic field.

Kinetics Study of Fabricated Photocatalytic Material Groups

Degradation reactions of organics in aqueous media via catalysts are intermittently studied using first and second order kinetic models. As briefly discussed in the end of Chapter 3, the apparent first and second order rate constants, k_1 and k_2 respectively, can be obtained by investigating the linear relationship in both kinetic models (**Eqs. 2** and **3**) below:

$$C_t = C_0 e^{-k_1 t} \qquad \textbf{(Eq. 2)}$$

$$\frac{1}{C_t} = \frac{1}{C_0} + k_2 t \qquad \textbf{(Eq. 3)}$$

It was already demonstrated that the photodegradation performance was systematically enhanced from the initial synthesis and use of pTNPs all the way to developing the final reduced bTNW/MWCNT (1:1, 380C) nanocomposite, and

efficiency was successfully maintained after the incorporation of paramagnetic heterojunctioned cores. In this section, kinetic studies of the most photoactive samples fabricated from each synthesis group will be performed in order to test the kinetic model that best fits the different set of experimental results. Moreover, insight on photodegradation kinetics from the kinetic models employed that shows the best fitting correlation will also shed light on the degradation mechanism at play.

Figure 44 below summarized all first and second order reaction kinetics obtained for the different sample groups. It can be seen that a consistent enhancement in the rate constant is witnessed between each successive sample group developed. All analysis has been performed on solar irradiation intensity of 700 W/m^2, with an initial MO concentration of 10 ppm, and a catalyst loading of 1 g/L – with the exception of 2 g/L for paramagnetic bTNWs/MWCNTs@SiO_2@Fe_3O_4.

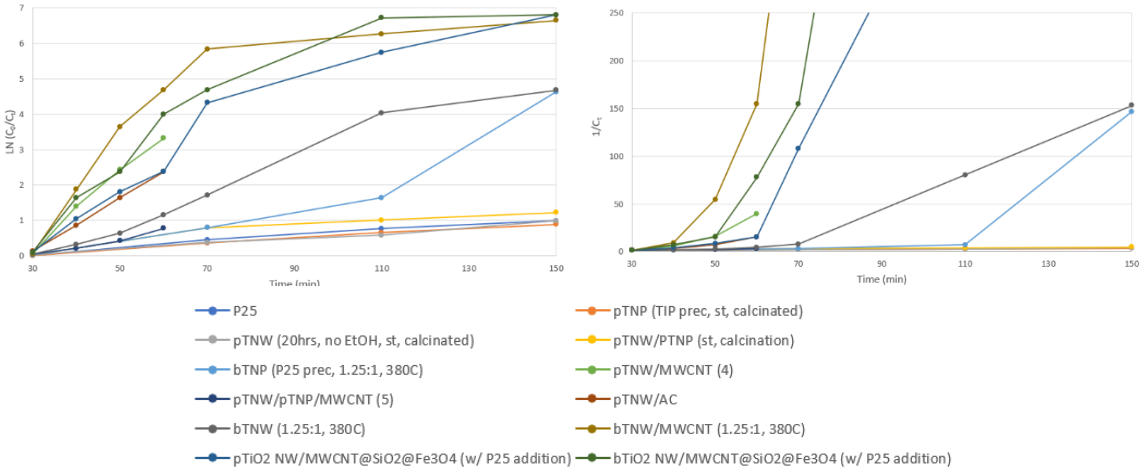

Figure 44– a) First and b) Second order kinetic plotting of photocatalytic samples of successive synthesis steps

Running the comparative analysis on both kinetic models and acquiring the coefficient of determination (R^2) for each respective model for selected samples, it can be determined from **Table 3** below that a first order kinetics model is more appropriate for this scheme of photodegradation using the developed titania-based nanocomposites.

Sample Name	First Order Rate Constant (k_1)	First Order Coefficient of Determination (R^2)	Second Order Rate Constant (k_2)	Second Order Coefficient of Determination (R^2)
Commercial P25	0.0081	0.9771	0.0172	0.9662
bTNW (1.25:1, 380C)	0.0418	0.9758	0.1541	0.8705
pTNW/MWCNT (4)	0.1087	0.9912	1.2471	0.8923
bTNW/MWCNT (1.25:1, 380C)	0.1439	0.9838	11.253	0.7575
pTiO2 NW/MWCNT@SiO2@Fe3O4 (w/ P25 addition)	0.0979	0.9495	2.2413	0.6132
bTiO2 NW/MWCNT@SiO2@Fe3O4 (w/ P25 addition)	0.1153	0.9831	3.771	0.83

Table 3– a) First and b) Second order kinetic plotting of photocatalytic samples of successive synthesis steps

It can be seen that the first order rate constant significantly increases from iteratively synthesized samples, which is indicative of the several suggested criteria discussed earlier during photocatalysts development. For instance, the morphological change and introduction of defect structures from P25 to bTNW (1.25:1, 380C) resulted in a the first order rate constant increasing by a factor of ten, which is attributed to the coupling of the enhanced surface area available upon morphological change and the ability to utilize a greater portion of the solar spectrum after reduction. The obtained pseudo-first order rate constant (k_1) is in fact the apparent kinetics constant, which is comprised of the product between the true reaction rate and the adsorption rate constants, k_r and k_{ads} respectively. This can be explained through the infamous Langmuir-Hinshelwood model. **Figure 45** below shows a schematic depiction of the

proposed mechanism of action during an effective solar-driven photodegradation phenomena induced by bTNW/MWCNTs.

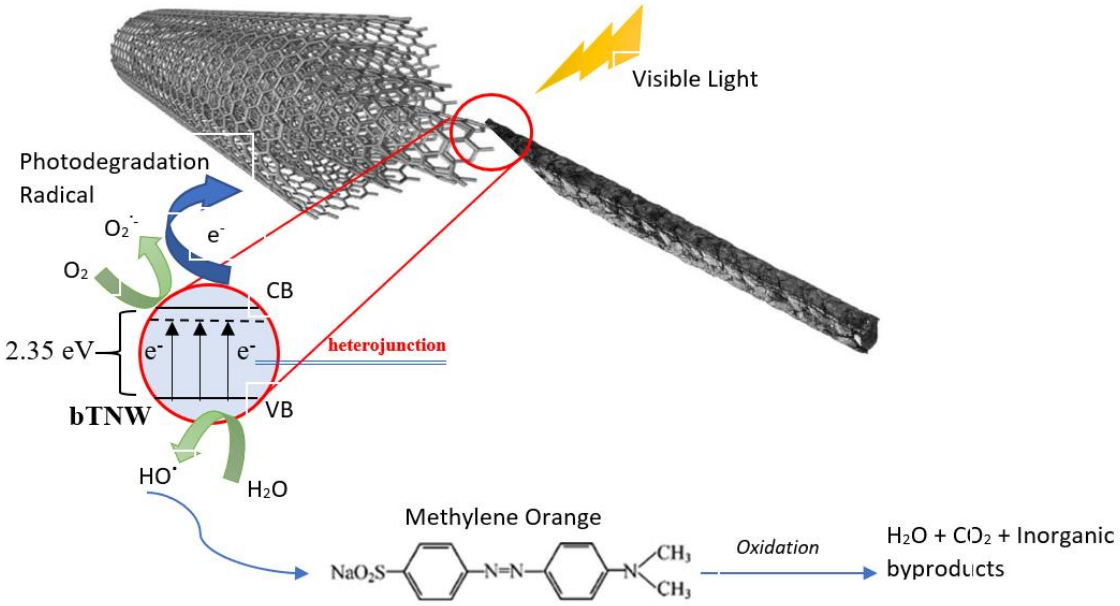

Figure 45– Proposed mechanism of bTNW/MWCNTs photodegradation of MO under solar light irradiation

Parametric Study on bTNW/MWCNTs

In order to obtain the optimum operating conditions for photodegradation of organics (i.e. MO) using the developed bNTWs/MWCNTs (1.25:1, 380C) photocatalyst, different conditions including pH, catalyst loading, and the effect of MO initial concentration were studied. For photodegradation experiments, illumination intensity was maintained at 700 W/m2, initial MO concentration was set for 10 ppm, catalyst load was 1 g/L, and pH was maintained at 7. However, in **Figure 46** below, one of the aforementioned

parameters was varied in order to investigate the varying effects these parameters have on the photodegradation efficiency.

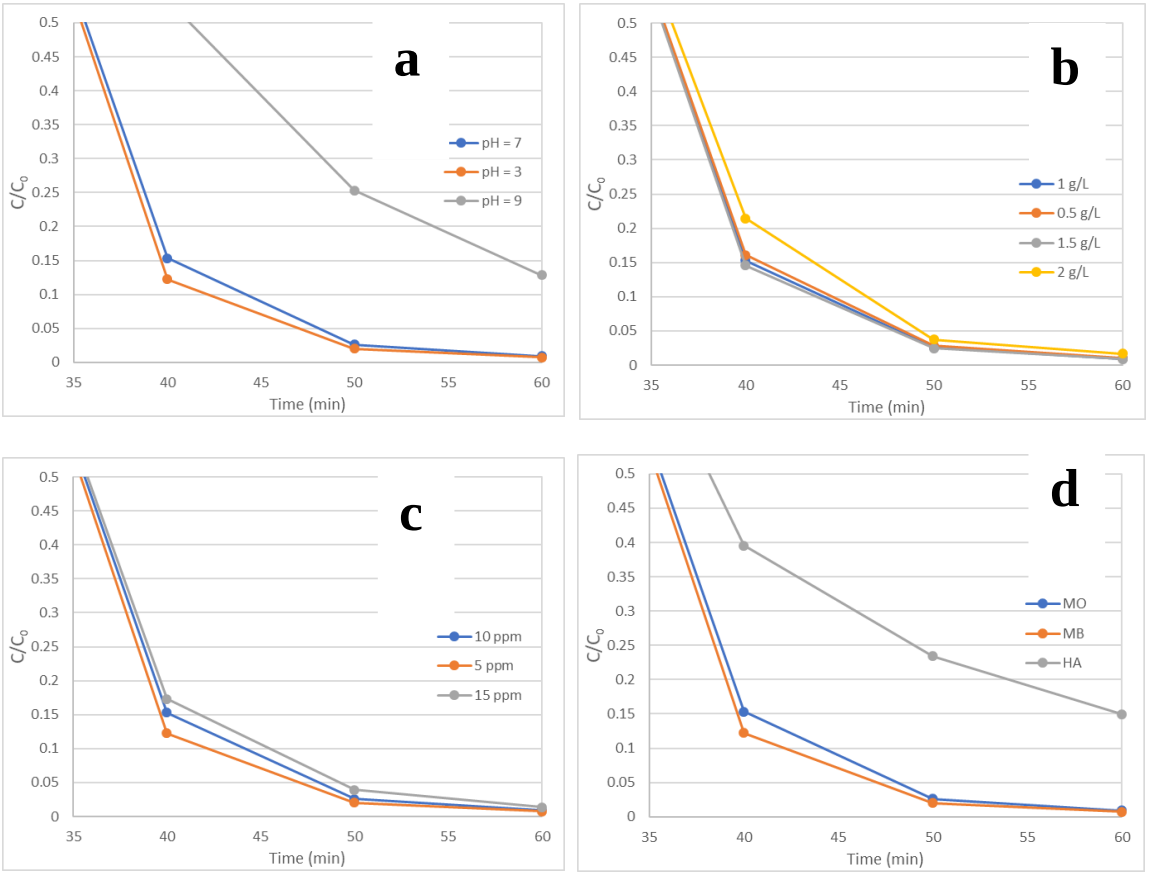

Figure 46– Photodegradation experiments performed using bTNW/MWCNT (1.25:1, 380C) whilst varying a) pH, b) catalyst load, c) initial MO concentration, and d) organic contaminant in solution

As can be seen from the above figure, the change of pH perhaps has the most substantial effect. Optimum degradation rates were found to be at acidic and neutral pH values, whilst by far a significant reduction in photodegradation can be seen by simply making the reaction solution more alkaline, **Figure 46 a**. It is worth noting that MO is an anionic dye, which means that in solution it will have a net negative charge. Thus, it

makes sense that in an acidic medium, adsorption would be enhanced atop the photocatalyst's surface, whereby facilitating a slight increase in photoreaction kinetics. However, in an alkaline medium, surface crevices atop the photocatalyst's defect surface structure, introduced during reduction, will contain hydroxyl ions which would repel the MO, in effect decreasing its adsorption likelihood. Since adsorption is decreased and the organic contaminant has a hinderance reaching the surface of the titania, the degradation would simply not occur, or in this case be partially hindered.

Increasing catalyst dose in the range of 0.5-2.0 g/L was found to have negligible effect of photodegradation efficiency (Figure 48 b). The same was observed for the effect of initial MO concentration (**Figure 46 c)**.

Interestingly, as can be seen from **Figure 46 d**, the developed photocatalyst effectively and unselectively is capable of degrading methylene orange and methylene blue as organic contaminants. This means that it is unselective in photodegrading cationic (MB) and anionic (MO) contaminants. There is however a significant decrease in its apparent photodegradation efficiency of humic acid (HA). This, however, is not very indicative that it does not effectively degrade organic humic compounds. The reason for this lies in the composition of the humic acid salt that was used as the source of humic acid. The humic salt used is less than 50% pure and other complex intermediates can negatively hinder the photodegradation of HA, or simply form colored complexes that are detected with the UV-Vis-NIR under the same absorption band as remaining HA concentration in solution with respect to time. Although, this could have been avoided by purifying the humic acid salt prior to use, in this case this was not done.

In all cases, the representative degradation of MO, MB and to a high degree, impure HA, is a very good indication that the developed photocatalyst is not selective in terms of organic contaminants that it can degrade. This leads to the inclination and promotion of the developed photocatalyst to be effectively utilized for water treatment/pre-treatment processes in waters that include natural organic compounds.

Lastly, in order to ensure the proper recyclability of the developed photocatalysts and bring it a step closer to commercial utilization through ensuring a higher degree of feasibility, recyclability photodegradation experiments were carried and are presented in **Figure 47** below. It can be seen that even after 3 cyclic runs of using the same photocatalytic material, the photodegradation efficiency is remarkably well maintained.

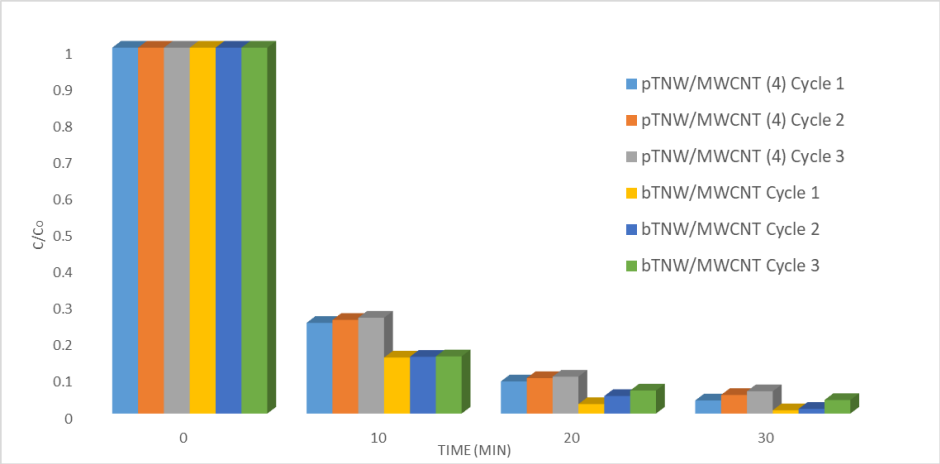

Figure 47– Photodegradation cyclability tests of 10ppm MO using pTNW/MWCNT (4) and bTNW/MWCNT (1.25:1, 380C) under solar irradiation

CHAPTER V

CONCLUSION AND RECOMMENDATIONS

Bound by its innate disadvantageous properties, including a fast electron-hole recombination rate and poor utilization of the available solar energy bombarding the Earth's surface, unmodified titania has had limiting options in truly capitalizing on its commercial use. In this work, however, the successful design, fabrication and characterization of modified titania-based photocatalyst was achieved. The careful design modifications introduced to the pristine titania nanospheres, used as the titania precursor, coerced the realization of a reduced black titania nanowire structure that is thoroughly heterojunctioned with MWCNTs. The surface defects atop the titania nanostructure allowed for the utilization of both UV and visible light regions. Moreover, the establishment of a high ratio of oxygen vacancies on the titania structure, along with MWCNTs heterojunctions, led to a notable reduction in the high bandgap energy of pristine titania (3.2 eV), and resulted in a final bandgap energy of 1.45 eV of the final photocatalyst. The promising photocatalyst developed, bTNWs/MWCNTs (1.25:1, 380C) yielded very high photodegradation efficiency (97.4%) of methylene orange (MO) – as a representative organic contaminant in a mere 20 minutes of artificial solar irradiation of 700 W/m^2 light intensity

Moreover, in order to bring this photocatalyst one step closer to commercial utilization, a very specific predicament facing the application of photocatalysts for large-

scale water pretreatment processes was addressed, strictly speaking the ease of recollection of the solid photocatalyst from treated waters. In tackling this particular conundrum, the implementation of a paramagnetic silica-coated iron oxide core to be used as carrier elements of the photoactive bTNWs/MWCNTs (1.25:1, 380C) was successfully designed, implemented and tested. The careful design resulted in a very slight decrease in photodegradation efficiency, compared to the stand-alone bTNWs/MWCNTs and yielded 90.9% photodegradation in 20 minutes of artificial solar irradiation.

In order to ensure the optimum design conditions are met through careful syntheses routes, several factors were iteratively checked whilst fabricating each successive modification to the titania (i.e. nanowires, implementation of MWCNTs, reduction, etc.). Moreover, due to the array of experimental conditions that may affect the apparent photodegradation efficiency, pH, catalyst load, initial MO concentration, and the degradation of other organic mimicking agents (i.e. MB, HA) photodegradation performance tests were carried out. The experimental results led to very interesting findings, and the confirmation that the developed photocatalyst is not specific in degrading anionic or cationic contaminants but will in fact effectively degrade both with a matching performance.

Characterization techniques performed on the developed photocatalysts, including but not limited to XRD, SEM, TEM, elemental imaging, XPS, solid-state UV-Vis-NIR, FTIR, etc. led a more translucent understanding of the design factors that influence and are detrimental in yielding a highly photoactive material. A predominant

anatase phase with {101} exposed lattice facets was found to be of paramount importance. Approximations through Scherrer equation, clearly showed that above a certain crystallite size (i.e. 15nm), there is a decreasing dependence on crystallite size for enhancing electron surface distance migration, and in effect decreasing the electron-hole recombination rate. Surface treatment procedures were found to have notable impacts on morphological roughening of surface and edge structures of 1-Dimensional titania nanostructures (i.e. nanowires), which in turn have had a phenomenal enhancement of photoactivity. The presence of oxygen vacancies and Ti^{3+} were found to further enhance photoactivity via the reduction in bandgap energy of titania. Surface defects introduced through reduction schemes were found to enhance adsorption and photoactivity of organic contaminants. Incorporating MWCNTs whilst ensuring for a successful heterojunction with the surface of the titania and low aggregation of the nanocomposite was found to be highly dependent on the morphology of titania precursor used. In the case where pristine surface treated titania nanowires were used for MWCNTs incorporation via alkaline hydrothermal treatment, the resulting pTNWs/MWCNTs (4) sample yielded the highest photodegradation of MO amongst all other MWCNTs incorporated samples. Generally, in order to achieve the highest photoactivity potential in the final material prepared, the highest photoactive sample from each synthesis group was utilized in further advancing the design modifications until the final photocatalyst was achieved.

In summary, this investigative study formally prepared a novel titania-based photocatalytic material that was remarkably photoactive and elegantly utilized both UV

and visible light of the solar spectrum. The resultant photodegradation experiments show this material to be one of the best in the field for photodegrading organic contaminants under solar light irradiation.

Future work can focus on developing a more robust photochemical reactor that can serve to be the standard for photodegradation performance experimental quantifications. This would allow better comparison of findings amongst researchers globally. Moreover, the photodegradation of actual (not synthetic) contaminated water sources should be more representative, since the smallest concentrations of substances found in real waters can have propagating hindering effects on photocatalysts via deactivation schemes, etc. Furthermore, the development of other novel photocatalysts that are not necessarily titania-based will further increase our understanding of heterogenous photocatalysis generally and may serendipitously lead to the discovery of a remarkably photoactive novel photocatalytic material.

REFERENCES

A.E. Giannakas, E. S., Y. Deligiannakis, I. Konstantinou. (2012). *Appl. Catal., B. Environ.*(132-133), 460-468.

A.S. Hassaniena, A. A. A. (2016). Effect of Se addition on optical and electrical properties of chalcogenide CdSSe thin films. *Superlattices and Microstructures, 89*, 153-169.

Anas, M., Han, D. S., Mahmoud, K., Park, H., & Abdel-Wahab, A. . (2016). Photocatalytic degradation of organic dye using titanium dioxide modified with metal and non-metal deposition. *Materials Science in Semiconductor Processing, 41*, 209-218.

Ariyanti, D., Mills, L., Dong, J., Yao, Y., & Gao, W. (2017). NaBH4 modified TiO2: Defect site enhancement related to its photocatalytic activity. *Materials Chemistry and Physics, 199*, 571-576.

Aryal, S., Kim, C. K., Kim, K. W., Khil, M. S., & Kim, H. Y. . (2008). Multi-walled carbon nanotubes/TiO2 composite nanofiber by electrospinning. *Materials Science and Engineering: C, 28*(1), 75-79.

Asahi, R. Y. O. J. I., Morikawa, T. A. K. E. S. H. I., Ohwaki, T., Aoki, K., & Taga, Y. (2001). Visible-light photocatalysis in nitrogen-doped titanium oxides. *science, 293*(5528), 269-271.

B. Ingham, M. F. T. (2014). X-ray diffraction for characterizing metallic films. *Optical and Magnetic Applications*.

Bagga, A., Chellam, S., & Clifford, D. A. (2008). Evaluation of iron chemical coagulation and electrocoagulation pretreatment for surface water microfiltration. *Journal of Membrane Science, 309*(1-2), 82-93.

Batzill, M. (2011). Fundamental aspects of surface engineering of transition metal oxide photocatalysts. *Energy & Environmental Science, 4*(9), 3275-3286.

Bond, T., Goslan, E. H., Parsons, S. A., & Jefferson, B. (2010). Disinfection by-product formation of natural organic matter surrogates and treatment by coagulation, MIEX and nanofiltration. *Water Res, 44*(5), 1645-1653. doi:10.1016/j.watres.2009.11.018

Burri, D. R., Choi, K. M., Han, S. C., Burri, A., & Park, S. E. . (2007). Selective conversion of ethylbenzene into styrene over K2O/TiO2-ZrO2 catalysts: Unified effects of K2O and CO2. *Journal of Molecular Catalysis A: Chemical, 269*(1-2), 58-63.

Cargnello, M., Gordon, T. R., & Murray, C. B. (2014). Solution-phase synthesis of titanium dioxide nanoparticles and nanocrystals. *Chemical reviews, 114*(19), 9319-9345.

Chalasani, R., & Vasudevan, S. (Cyclodextrin-functionalized Fe3O4@ TiO2: reusable, magnetic nanoparticles for photocatalytic degradation of endocrine-disrupting chemicals in water supplies). 2013. *ACS nano, 7*(5), 4093-4104.

Chen, G., Ji, S., Li, H., Kang, X., Chang, S., Wang, Y.,Liu, H. (2015). High-energy faceted SnO2-coated TiO2 nanobelt heterostructure for near-ambient temperature-responsive ethanol sensor. *ACS applied materials & interfaces, 7*(44), 24950-24956.

Chen, J. S., Tan, Y. L., Li, C. M., Cheah, Y. L., Luan, D., Madhavi, S., ... & Lou, X. W. (2010). Constructing hierarchical spheres from large ultrathin anatase TiO2 nanosheets with nearly 100% exposed (001) facets for fast reversible lithium storage. *Journal of the American Chemical Society, 132*(17), 6124-6130.

Chen, L. C., Ho, Y. C., Guo, W. S., Huang, C. M., & Pan, T. C. (2009). Enhanced visible light-induced photoelectrocatalytic degradation of phenol by carbon nanotube-doped TiO2 electrodes. *Electrochimica Acta, 54*(15), 3884-3891.

Chen, X., Liu, L., Liu, Z., Marcus, M. A., Wang, W. C., Oyler, N. A., ... & Guo, J. . (2013). Properties of disorder-engineered black titanium dioxide nanoparticles through hydrogenation. *Scientific reports, 3*, 1510.

Chen, X., Liu, L., Peter, Y. Y., & Mao, S. S. . (2011). Increasing solar absorption for photocatalysis with black hydrogenated titanium dioxide nanocrystals. *science, 331*(6018), 746-750.

Chen, X., & Mao, S. S. (2007). Titanium dioxide nanomaterials: synthesis, properties, modifications, and applications. *Chemical reviews, 107*(7), 2891-2959.

Chow, C. W., van Leeuwen, J. A., Fabris, R., & Drikas, M. (2009). Optimised coagulation using aluminium sulfate for the removal of dissolved organic carbon. *Desalination, 245*(1-3), 120-134.

Dai, G., Yu, J., & Liu, G. (2012). A new approach for photocorrosion inhibition of Ag2CO3 photocatalyst with highly visible-light-responsive reactivity. *The Journal of Physical Chemistry C, 116*(29), 15519-15524.

DESA, U. (2017, 21 June 2017). World population projected to reach 9.8 billion in 2050, and 11.2 billion in 2100. Retrieved from https://www.un.org/development/desa/en/news/population/world-population-prospects-2017.html

Devi, L. G., & Kavitha, R. (2013). A review on non metal ion doped titania for the photocatalytic degradation of organic pollutants under UV/solar light: Role of photogenerated charge carrier dynamics in enhancing the activity. *Applied Catalysis B: Environmental, 140*, 559-587.

EPA, U. (2018). National Pollutant Discharge Elimination System (NPDES). Retrieved from https://www.epa.gov/npdes/about-npdes

Fabris, R., Chow, C. W., Drikas, M., & Eikebrokk, B. (2008). Comparison of NOM character in selected Australian and Norwegian drinking waters. *Water Res, 42*(15), 4188-4196. doi:10.1016/j.watres.2008.06.023

Fox, M. A., & Dulay, M. T. (1993). Heterogeneous photocatalysis. *Chemical reviews, 93*(1), 341-357.

Fu, H., Yang, L., Hu, D., Yu, C., Ling, Y., Xie, Y., Zhao, J. . (2018). Titanium dioxide nano-heterostructure with nanoparticles decorating nanowires for high-performance photocatalysis. *International Journal of Hydrogen Energy, 43*(22), 10359-10367.

Fujihira, M., Satoh, Y., & Osa, T. (1981). Heterogeneous photocatalytic oxidation of aromatic compounds on TiO2. *Nature, 293*(5829), 206.

Ge, M., Cao, C., Huang, J., Li, S., Chen, Z., Zhang, K. Q., ... & Lai, Y. (2016). A review of one-dimensional TiO 2 nanostructured materials for environmental and energy applications. *Journal of Materials Chemistry A, 4*(18), 6772-6801.

Górska, P., Zaleska, A., Kowalska, E., Klimczuk, T., Sobczak, J. W., Skwarek, E., ... & Hupka, J. . (2008). TiO2 photoactivity in Vis and UV light: the influence of calcination temperature and surface properties. *Applied Catalysis B: Environmental, 84*(3-4), 440-447.

H. XingGang, H. M., W. XiaoLing, L. Dong. (2009). First-principles calculations on implanted TiO2 by 3d transition metal ions. *Science in China Series, 52*, 838-842.

H.T. Gao, Y. Y. L., C.H. Ding, D.M. Dai, G.J. Liu. (2011). *Int. J. Min. Met. Mate., 8*, 606-614.

Heshan, C. A. I., Guoguang, L. I. U., Lü, W., Xiaoxia, L. I., Lin, Y. U., & Daguang, L. I. (2008). Effect of Ho-doping on photocatalytic activity of nanosized TiO2 catalyst. *Journal of Rare Earths, 26*(1), 71-75.

Hossain, F. M., Evteev, A. V., Belova, I. V., Nowotny, J., & Murch, G. E. (2010). Electronic and optical properties of anatase TiO2 nanotubes. *Computational Materials Science, 48*(4), 854-858.

Hu, C., Zhang, R., Xiang, J., Liu, T., Li, W., Li, M., ... & Wei, F. . (2011). Synthesis of carbon nanotube/anatase titania composites by a combination of sol–gel and self-assembly at low temperature. *Journal of Solid State Chemistry, 184*(5), 1286-1292.

J. Tian, X. H., H. Yang, Y. Zhou, H. Cui, H. Lui. (2016). *Applied Surface Science*, 738-743.

Jacangelo JG, D. J., Owen DM, Randtke SJ. (1995). Selected processes for removing NOM: an overview. *American Water Works Association (AWWA)*, 64-87.

Jarvis, P., Jefferson, B., & Parsons, S. (2004). Characterising natural organic matter flocs. *Water Science and Technology: Water Supply, 4*(4), 79-87.

Kang, Q., Cao, J., Zhang, Y., Liu, L., Xu, H., & Ye, J. (2013). Reduced TiO 2 nanotube arrays for photoelectrochemical water splitting. *Journal of Materials Chemistry A, 1*(18), 5766-5774.

Konstantinou, I. K., & Albanis, T. A. (2004). TiO2-assisted photocatalytic degradation of azo dyes in aqueous solution: kinetic and mechanistic investigations: a review. *Applied Catalysis B: Environmental, 49*(1), 1-14.

Kuo, C. Y. (2009). Prevenient dye-degradation mechanisms using UV/TiO2/carbon nanotubes process. *Journal of hazardous materials, 163*(1), 239-244.

Lacombe, S., Fresno, F., & Štangar, U. L. (2014). Photocatalysis: new highlights from JEP 2013.

Lee, H. U., Lee, S. C., Choi, S. H., Son, B., Lee, S. J., Kim, H. J., & Lee, J. . (2013). Highly visible-light active nanoporous TiO2 photocatalysts for efficient solar photocatalytic applications. *Applied Catalysis B: Environmental, 129*, 106-113.

Lee, S. Y., & Park, S. J. . (2013). TiO2 photocatalyst for water treatment applications. *Journal of Industrial and Engineering Chemistry, 19*(6), 1761-1769.

Li, Z., Gao, B., Chen, G. Z., Mokaya, R., Sotiropoulos, S., & Puma, G. L. (2011). Carbon nanotube/titanium dioxide (CNT/TiO2) core–shell nanocomposites with tailored shell thickness, CNT content and photocatalytic/photoelectrocatalytic properties. *Applied Catalysis B: Environmental, 110*, 50-57.

Liu, C., Tang, X., Mo, C., & Qiang, Z. (2008). Characterization and activity of visible-light-driven TiO2 photocatalyst codoped with nitrogen and cerium. *Journal of Solid State Chemistry, 181*(4), 913-919.

Liu, H., Jia, Z., Ji, S., Zheng, Y., Li, M., & Yang, H. . (2011). Synthesis of TiO2/SiO2@ Fe3O4 magnetic microspheres and their properties of photocatalytic degradation dyestuff. *Catalysis Today, 175*(1), 293-298.

Liu, X., Gao, S., Xu, H., Lou, Z., Wang, W., Huang, B., & Dai, Y. . (2013). Green synthetic approach for Ti 3+ self-doped TiO 2− x nanoparticles with efficient visible light photocatalytic activity. *Nanoscale, 5*(5), 1870-1875.

Lu, J., Han, Q., & Wang, Z. . (2012). Synthesis of TiO2/Bi2S3 heterojunction with a nuclear-shell structure and its high photocatalytic activity. *Materials Research Bulletin, 47*(7), 1621-1624.

Luttrell, T., Halpegamage, S., Tao, J., Kramer, A., Sutter, E., & Batzill, M. (2014). Why is anatase a better photocatalyst than rutile?-Model studies on epitaxial TiO 2 films. *Scientific reports, 4*, 4043.

Lv, C., Zhou, Y., Li, H., Dang, M., Guo, C., Ou, Y., & Xiao, B. . (2011). Synthesis and characterisation of Gd3+-doped mesoporous TiO2 materials. *Applied Surface Science, 257*(11), 5104-5108.

Matsukawa, S., Itoho, S., Habutnu, S., Aizawa, T. (2006). *Water Sci. Technol., 6*(67).

Mollah, M. Y., Morkovsky, P., Gomes, J. A., Kesmez, M., Parga, J., & Cocke, D. L. (2004). Fundamentals, present and future perspectives of electrocoagulation. *Journal of hazardous materials, 114*(1-3), 199-210.

Morran, J. Y., Drikas, M., Cook, D., & Bursill, D. B. . (2004). Comparison of MIEX® treatment and coagulation on NOM character. *Water Science and Technology: Water Supply, 4*(4), 129-137.

Muduli, S., Lee, W., Dhas, V., Mujawar, S., Dubey, M., Vijayamohanan, K., ... & Ogale, S. (2009). Enhanced conversion efficiency in dye-sensitized solar cells based on

hydrothermally synthesized TiO2− MWCNT nanocomposites. *ACS applied materials & interfaces, 1*(9), 2030-2035.

Naldoni, A., Allieta, M., Santangelo, S., Marelli, M., Fabbri, F., Cappelli, S., ... & Dal Santo, V. (2012). Effect of nature and location of defects on bandgap narrowing in black TiO2 nanoparticles. *Journal of the American Chemical Society, 134*(18), 7600-7603.

Ohtani, B. (2010). Photocatalysis A to Z—What we know and what we do not know in a scientific sense. *Journal of Photochemistry and Photobiology C: Photochemistry Reviews, 11*(4), 157-178.

Pan, H., Zhang, Y. W., Shenoy, V. B., & Gao, H. (2011). Effects of H-, N-, and (H, N)-doping on the photocatalytic activity of TiO2. *The Journal of Physical Chemistry C, 115*(24), 12224-12231.

Pan, J., Liu, G., Lu, G. Q., & Cheng, H. M. (2011). On the true photoreactivity order of {001},{010}, and {101} facets of anatase TiO2 crystals. *Angewandte Chemie International Edition, 50*(9), 2133-2137.

Peng, F., Cai, L., Huang, L., Yu, H., & Wang, H. (2008). Preparation of nitrogen-doped titanium dioxide with visible-light photocatalytic activity using a facile hydrothermal method. *journal of Physics and Chemistry of Solids, 69*(7), 1657-1664.

Pozan, G. S., & Kambur, A. (2014). Significant enhancement of photocatalytic activity over bifunctional ZnO–TiO2 catalysts for 4-chlorophenol degradation. *Chemosphere, 105*, 152-159.

Rämö, J., & Sillanpää, M. (2001). Degradation of EDTA by hydrogen peroxide in alkaline conditions. *Journal of cleaner production, 9*(3), 191-195.

Rao, G., Brastad, K. S., Zhang, Q., Robinson, R., He, Z., & Li, Y. . (2016). Enhanced disinfection of Escherichia coli and bacteriophage MS2 in water using a copper and silver loaded titanium dioxide nanowire membrane. *Frontiers of Environmental Science and Engineering, 10*(4).

Rao, G., Zhang, Q., Zhao, H., Chen, J., & Li, Y. . (2016). Novel titanium dioxide/iron (III) oxide/graphene oxide photocatalytic membrane for enhanced humic acid removal from water. *Chemical Engineering Journal, 302*, 633-640.

Rao, G., Zhao, H., Chen, J., Deng, W., Jung, B., Abdel-Wahab, A., Li, Y. (2017). FeOOH and Fe2O3 co-grafted TiO2 photocatalysts for bisphenol A degradation in water. *Catalysis Communications, 97*, 125-129.

Reddy, K. M., Manorama, S. V., & Reddy, A. R. (2003). Bandgap studies on anatase titanium dioxide nanoparticles. *Materials Chemistry and Physics, 78*(1), 239-245.

Richard Helmer, I. H. (1997). *Water Pollution Control: A Guide to the Use of Water Quality Management Principles*: CRC Press.

Schneider, J., Matsuoka, M., Takeuchi, M., Zhang, J., Horiuchi, Y., Anpo, M., & Bahnemann, D. W. (2014). Understanding TiO2 photocatalysis: mechanisms and materials. *Chemical reviews, 114*(19), 9919-9986.

Semiat, R. (2000). Desalination: Present and Future. *Water International, 25*, 54-65. doi:10.1080/02508060008686797

Shi, J. W., Zheng, J. T., Hu, Y., & Zhao, Y. C. (2007). Influence of Fe3+ and Ho3+ co-doping on the photocatalytic activity of TiO2. *Materials Chemistry and Physics, 106*(2-3), 247-249.

Siéliéchi, J.-M., Lartiges, B. S., Kayem, G., Hupont, S., Frochot, C., Thieme, J., . . . Kamga, R. (2008). Changes in humic acid conformation during coagulation with ferric chloride: Implications for drinking water treatment. *Water Res, 42*(8-9), 2111-2123.

Song, X., & Gao, L. (2007). Fabrication of hollow hybrid microspheres coated with silica/titania via sol− gel process and enhanced photocatalytic activities. *The Journal of Physical Chemistry C, 111*(23), 8180-8187.

Sussman, M. J., Brodusch, N., Gauvin, R., & Demopoulos, G. P. (2013). Novel Mesoporous Nanotitania/Carbon Composite Electrodes for Electrochemical Energy Storage. *ECS Transactions, 50*(24), 37-48.

Swietlik, J., Dabrowska, A., Raczyk-Stanislawiak, U., & Nawrocki, J. (2004). Reactivity of natural organic matter fractions with chlorine dioxide and ozone. *Water Res, 38*(3), 547-558. doi:10.1016/j.watres.2003.10.034

Syzgantseva, O. A., Gonzalez-Navarrete, P., Calatayud, M., Bromley, S., & Minot, C. (2011). Theoretical Investigation of the Hydrogenation of (TiO2) n Clusters (n= 1–10). *The Journal of Physical Chemistry C, 115*(32), 15890-15899.

Tian, J., Hao, P., Wei, N., Cui, H., & Liu, H. (2015). 3D Bi2MoO6 nanosheet/TiO2 nanobelt heterostructure: enhanced photocatalytic activities and photoelectochemistry performance. *ACS catalysis, 5*(8), 4530-4536.

Tieng, S., Azouani, R., Chhor, K., & Kanaev, A. (2011). Nucleation− Growth of TiO2 Nanoparticles Doped with Iron Acetylacetonate. *The Journal of Physical Chemistry C, 115*(13), 5244-5250.

Tominaka, S., Tsujimoto, Y., Matsushita, Y., & Yamaura, K. . (2011). Synthesis of nanostructured reduced titanium oxide: crystal structure transformation maintaining nanomorphology. *Angewandte Chemie International Edition, 50*(32), 7418-7421.

UN. (2016). Transforming our world: the 2030 Agenda for Sustainable Development. Retrieved from https://sustainabledevelopment.un.org/post2015/transformingourworld

Uyak, V., Yavuz, S., Toroz, I., Ozaydin, S., & Genceli, E. A. (2007). Disinfection by-products precursors removal by enhanced coagulation and PAC adsorption. *Desalination, 216*(1-3), 334-344.

Uyak, V., Yavuz, S., Toroz, I., Ozaydin, S., & Genceli, E. A. (2007). Disinfection by-products precursors removal by enhanced coagulation and PAC adsorption. *Desalination, 216*(1-3), 334-344.

Vijayan, B. K., Dimitrijevic, N. M., Wu, J., & Gray, K. A. (2010). The effects of Pt doping on the structure and visible light photoactivity of titania nanotubes. *The Journal of Physical Chemistry C, 114*(49), 21262-21269.

Wang, G., Wang, H., Ling, Y., Tang, Y., Yang, X., Fitzmorris, R. C., ... & Li, Y. . (2011). Hydrogen-treated TiO2 nanowire arrays for photoelectrochemical water splitting. *Nano letters, 11*(7), 3026-3033.

Wang, Q., Xu, S., & Shen, F. (2011). Preparation and characterization of TiO2 photocatalysts co-doped with iron (III) and lanthanum for the degradation of organic pollutants. *Applied Surface Science, 257*(17), 7671-7677.

Wang, X., Li, Z., Shi, J., & Yu, Y. (2014). One-dimensional titanium dioxide nanomaterials: nanowires, nanorods, and nanobelts. *Chemical reviews, 114*(19), 9346-9384.

Wang, Z., Yang, C., Lin, T., Yin, H., Chen, P., Wan, D., ... & Jiang, M. . (2013). H-doped black titania with very high solar absorption and excellent photocatalysis enhanced by localized surface plasmon resonance. *Advanced Functional Materials, 23*(43), 5444-5450.

Wu, M. C., Chen, C. H., Huang, W. K., Hsiao, K. C., Lin, T. H., Chan, S. H., ... & Hsu, K. H. (2017). Improved solar-driven photocatalytic performance of highly

crystalline hydrogenated TiO 2 nanofibers with core-shell structure. *Scientific reports, 7*, 40896.

Xin, T., Ma, M., Zhang, H., Gu, J., Wang, S., Liu, M., & Zhang, Q. (2014). A facile approach for the synthesis of magnetic separable Fe3O4@ TiO2, core–shell nanocomposites as highly recyclable photocatalysts. *Applied Surface Science, 288*, 51-59.

Xu, C., Song, Y., Lu, L., Cheng, C., Liu, D., Fang, X., ... & Li, D. (2013). Electrochemically hydrogenated TiO 2 nanotubes with improved photoelectrochemical water splitting performance. *Nanoscale Research Letters, 8*(1).

Xu, M., Gao, Y., Moreno, E. M., Kunst, M., Muhler, M., Wang, Y., ... & Wöll, C. (2011). Photocatalytic activity of bulk TiO 2 anatase and rutile single crystals using infrared absorption spectroscopy. *Physical Review Letters, 106*(13).

Yoon, S. H., ElShorafa, R., Katbeh, M., Han, D. S., Jeong, H. W., Park, H., & Abdel-Wahab, A. (2017). Effect of shape-driven intrinsic surface defects on photocatalytic activities of titanium dioxide in environmental application. *Applied Surface Science, 423*, 71-77.

Yu, H., Quan, X., Chen, S., Zhao, H., & Zhang, Y. (2008). TiO2–carbon nanotube heterojunction arrays with a controllable thickness of TiO2 layer and their first application in photocatalysis. *Journal of Photochemistry and Photobiology A: Chemistry, 200*(2-3), 301-306.

Yu, J., & Yu, X. (2008). Hydrothermal synthesis and photocatalytic activity of zinc oxide hollow spheres. *Environmental science & technology, 42*(13), 4902-4907.

Yu, J., Wang, D., Yan, M., Ye, C., Yang, M., & Ge, X. (2007). Optimized coagulation of high alkalinity, low temperature and particle water: pH adjustment and polyelectrolytes as coagulant aids. *Environmental monitoring and assessment, 131*(1-3), 377-386.

Yu, J., Xiong, J., Cheng, B., Yu, Y., & Wang, J. (2005). Hydrothermal preparation and visible-light photocatalytic activity of Bi2WO6 powders. *Journal of Solid State Chemistry, 178*(6), 1968-1972.

Yu, J., Zhang, J., & Liu, S. (2010). Ion-exchange synthesis and enhanced visible-light photoactivity of CuS/ZnS nanocomposite hollow spheres. *The Journal of Physical Chemistry C, 114*(32), 13642-13649.

Yu, X., Liu, S., & Yu, J. . (2011). Superparamagnetic γ-Fe2O3@ SiO2@ TiO2 composite microspheres with superior photocatalytic properties. *Applied Catalysis B: Environmental, 104*(1-2), 12-20.

Yu, Y., Wu, H. H., Zhu, B. L., Wang, S. R., Huang, W. P., Wu, S. H., & Zhang, S. M. . (2008). Preparation, characterization and photocatalytic activities of F-doped TiO 2 nanotubes. *Catalysis Letters, 121*(1-2), 165-171.

Yuan, J., Wang, E., Chen, Y., Yang, W., Yao, J., & Cao, Y. (2011). Doping mode, band structure and photocatalytic mechanism of B–N-codoped TiO2. *Applied Surface Science, 257*(16), 7335-7342.

Zhang, C., Yu, H., Li, Y., Gao, Y., Zhao, Y., Song, W., ... & Yi, B. . (2013). Supported Noble Metals on Hydrogen-Treated TiO2 Nanotube Arrays as Highly Ordered Electrodes for Fuel Cells. *ChemSusChem, 6*(4), 659-666.

Zhang, Q., Rao, G., Rogers, J., Zhao, C., Liu, L., & Li, Y. (2015). Novel anti-fouling Fe2O3/TiO2 nanowire membranes for humic acid removal from water. *Chemical Engineering Journal, 271*, 180-187.

Zhang, X., Zhou, G., Zhang, H., Wu, C., & Song, H. (2011). Characterization and activity of visible light–driven TiO 2 photocatalysts co-doped with nitrogen and lanthanum. *Transition Metal Chemistry, 36*(2), 217-222.

Zhang, Y., Tang, Z. R., Fu, X., & Xu, Y. J. . (2010). TiO2− graphene nanocomposites for gas-phase photocatalytic degradation of volatile aromatic pollutant: is TiO2− graphene truly different from other TiO2− carbon composite materials? *ACS nano, 4*(12), 7303-7314.

Zhang, Y., Xing, Z., Yang, S., Zhou, W. . (2017). 3D urchin-like black TiO2-x/carbon nanotube heterostructures as efficient visible-light-driven photocatalysts. *RSC Advances, 7*, 453-460.

Zhao, H., Chen, J., Rao, G., Deng, W., & Li, Y. (2017). Enhancing photocatalytic CO2 reduction by coating an ultrathin Al2O3 layer on oxygen deficient TiO2 nanorods through atomic layer deposition. *Applied Surface Science, 404*, 49-56.

Zhou, P., Wang, Y., Xie, C., Chen, C., Liu, H., Chen, R., ... & Wang, S. . (2017). Acid-etched layered double hydroxides with rich defects for enhancing the oxygen evolution reaction. *Chemical Communications, 53*(86), 11778-11781.

Zhou, P., Yu, J., & Wang, Y. . (2013). The new understanding on photocatalytic mechanism of visible-light response NS codoped anatase TiO2 by first-principles. *Applied Catalysis B: Environmental, 142*, 45-53.

Zhu, W. D., Wang, C. W., Chen, J. B., Li, D. S., Zhou, F., & Zhang, H. L. (2012). Enhanced field emission from hydrogenated TiO2 nanotube arrays. *Nanotechnology, 23*(45).

Zollinger, H. (1991). *Color Chemistry: Synthesis, Properties and Applications of Organic Dyes and Pigments - 2nd edition*: VCH.

Zou, X., Liu, J., Su, J., Zuo, F., Chen, J., & Feng, P. . (2013). Facile Synthesis of Thermal-and Photostable Titania with Paramagnetic Oxygen Vacancies for Visible-Light Photocatalysis. *Chemistry–A European Journal, 19*(8), 2866-2873.